Development of Ultrasensitive Analytical Techniques to Detect Trace Elements

A Dissertation Presented for the

Doctor of Philosophy

Degree

The University of Tennessee, Knoxville

Elisa Romero Romero

December 2019

© by Elisa Romero Romero, 2019
All Rights Reserved.

To my family

Acknowledgments

I thank the Consejo Nacional de Ciencia y Tecnología (CONACYT) and the graduate research scholarship under the tutelage of Dr. Galindo Uribarri for the economic support received during the PhD program.

The PhD has been the most challenging stage of my life. I remember my advisor always told me the PhD is a training to be an independent researcher, for me that means have curiosity for everything surrounding us, have an analytical mind, discover and investigate new physics, challenge yourself, always learn and teach. Now after this long path, I see the world in a very different way, I can consider myself as a "very promising independent researcher" and I will be eternally thankful to my advisor for teaching me that, Dr. Galindo-Uribarri, his guidance and encouragement helped to make all this possible.

I thank all the technical and administrative support in both ORNL and UTK. I also thank all the researches and technicians from ANU and CIRCE for their support and for their very welcoming work environment.

I am very thankful to the PROSPECT collaboration, it was a pleasure to meet all of you.

I thank to all of my fellow student colleagues and summer students, I prefer not to give the list of their names as I don't want nobody to be left out.

Last but not least, I want to thank my family, my partner and friends to be there in this strenuous path, even though they did not understand what I was doing, the supported me and encouraged me to keep going. My family being at distance were always so close to me.

Abstract

In this thesis, two methods for ultra-trace analysis were investigated: the negative-ion based Accelerator Mass Spectrometry (AMS) and positive-ion based Resonant Ionization Mass Spectrometry (RIMS). The detection, monitoring and quantification of ultra-low levels of actinides is of considerable importance and represents a challenge in many fields of modern science: neutrino physics, dark matter searches, nuclear astrophysics, environmental science, etc. These fields demand more sensitive and more efficient techniques and are pushing the limits of conventional techniques for ultra-trace analysis.

Employing the 14 MV tandem accelerator of the Australian National University, we demonstrated an AMS method capable of detecting ultra-low traces of Th and U from ultrapure Cu made underground for the Majorana Demonstrator.

We made significant advancements on the actinide detection efficiency and sensitivity with the laser-based technique RIMS. We demonstrated that RIMS is a powerful analytical technique for actinides since it does not require large amount of material, has high selectivity, high efficiency and high sensitivity. Several three-step ionization schemes were studied and numerous high-lying and autoionizing levels were observed for Pu, Th, and U. We obtained efficiencies up to 51% for Pu, 32% for Th and 9% for U. These efficiencies represent the largest efficiencies reported for actinides and surpass significantly the efficiencies obtained in AMS for actinides which are between 0.1% to 1%.

We performed sensitivity studies with a setup consisting of a Resonant Ionization Laser Ion Source (RILIS), a mass spectrometer based on the Holifield Radioactive Ion Beam Facility radioactive injector IRIS2 and a single ion counter. We obtained a detection limit of 10^3 atoms for ^{240}Pu which is 1-2 orders of magnitude below previously reported.

Atomic spectroscopic studies for Pu were done revealing four Rydberg series in the energetically high-lying region in the atomic spectrum. The first ionization potential (IP) of Pu was precisely determined as 48605.748 $(95)_{stat}(49)_{sys}$ cm^{-1} using two methods. This value is a factor of three more precise than the one reported in the NIST database and constitutes a benchmark for modern relativistic atomic theories.

Table of Contents

1 Introduction **1**

2 The Need for Highly Efficient and Sensitive Techniques: Two Examples **4**

2.1 Introduction 4

2.2 Neutrino Physics 5

2.3 Neutrinoless Double Beta Decay 7

2.4 Actinides 9

2.5 Relativistic Effects and Determination of Ionization Potential of Heavy Elements 12

2.6 Plutonium: History and Properties 14

3 Ultra-trace Detection Techniques applied in Actinides **18**

4 Accelerator Mass Spectrometry **22**

4.1 Introduction 22

4.2 Principles of AMS 23

4.3 Ion Source 26

4.4 Injection System 26

4.5 Tandem Accelerator 26

4.6 High-energy Beam Selection 28

4.7 Ion Detection 28

5 U and Th detection using AMS **30**

5.1 Introduction 30

5.2 AMS at ANU 32

5.3 Experimental Procedure . . . 35
5.3.1 Sample Preparation . . . 35
5.4 Injection Beams . . . 36
5.5 U and Th in Cu Samples and Outlook . . . 39

6 Resonant Ionization Mass Spectrometry 41
6.1 Introduction . . . 41
6.2 Resonance Ionization Laser Ion Source . . . 42
6.3 Hot Cavity Surface Ionization source . . . 46
6.4 Laser System Description . . . 47
6.5 Experimental Setup at ORNL . . . 48

7 Plutonium Sample 52
7.1 Introduction . . . 52
7.2 ^{242}Pu Sample Dilution . . . 53
7.3 Sample Drying Process for RILIS . . . 57

8 Plutonium Level Schemes Search 61
8.1 Introduction . . . 61
8.2 Second Step Scan . . . 61
8.3 Third Step Scan . . . 62

9 Saturation and Power Broadening 69
9.1 Introduction . . . 69
9.2 Saturation Measurement . . . 70

10 Efficiency Measurements of Actinides 74
10.1 Introduction . . . 74
10.2 Experiment Description . . . 75
10.3 Results . . . 77

11 Sensitivity Measurements with Plutonium 80
11.1 Introduction . . . 80

11.2 Channeltron Detector . . . 81
11.2.1 Channeltron installation . . . 82
11.3 Channeltron Characterization . . . 83
11.4 Background Characterization . . . 86
11.5 Detection Limits . . . 86

12 Plutonium Rydberg States **90**
12.1 Rydberg Properties . . . 92
12.2 Quantum Defect . . . 93
12.3 ^{242}Pu Spectrum with Rydberg States . . . 94
12.4 Determination of the Ionization Potential . . . 94
12.4.1 Method 1 . . . 95
12.4.2 Method 2 . . . 96
12.5 Pu IP Error Analysis . . . 103
12.6 Discussion . . . 103

13 Conclusions **107**

Bibliography **109**

Appendices **131**

A Cluster Formations **132**
A Discussion . . . 134

B Search for Doubly Charged Negative Atomic Ions **136**

C PROSPECT **140**

D Level Schemes **142**

Vita **177**

List of Tables

5.1 Cu samples with different purity. 36

5.2 Input beam molecules and tuning beam molecules. 37

7.1 Weight of the bottle before and after dilution. 56

7.2 Different sample dilutions and sizes for different stages in the experiment. . . 59

8.1 Measured energies of the second excited states and the FWHM of the resonance transitions. The given uncertainties for λ_2 are the standard deviations of the scan-up and scan-down measurements, not including the systematic error. The uncertainties for E_2 includes error propagation from λ_1 and λ_2. The pink shaded rows are the peaks we chose for the third-step scan. Units are in cm^{-1}. 64

11.1 Channeltron and faraday cups intensities comparison between different cathode values. 84

11.2 Isotopic composition of the ^{242}Pu sample and the respective isotopic ratio. Experimental counts were obtained by fitting the experimental data of Figure 11.6. The experimental ratio for ^{240}Pu match the expected ratio of the sample. 89

12.1 Results of Rydberg-Ritz fit for schemes A and B. The given uncertainties are the standard deviation of the fit. Last column is the value of IP derived from the series limits. 96

12.2 Results with statistical and systematic errors for both methods in A and B schemes. MiSi means Method i, Series i with i 1 or 2. All units are in cm^{-1}. 105

12.3 Plutonium IP values obtained with Rydberg convergence and photoionization threshold techniques. The value reported for this work is the average of all the values obtained from Table 12.2 and the uncertainty is given by the error propagation of those values. 105

D.1 $E_2 = 35568.888\ cm^{-1}$ 142
D.2 $E_2 = 35790.806\ cm^{-1}$ 144
D.3 $E_2 = 35977.442\ cm^{-1}$ 150
D.4 $E_2 = 36313.781\ cm^{-1}$ 159
D.5 $E_2 = 36452.504\ cm^{-1}$ 165
D.6 $E_2 = 36689.646\ cm^{-1}$ 167

List of Figures

2.1 Schematic diagram for (a) $2\nu\beta\beta$ decay and (b) $0\nu\beta\beta$ decay. 8

2.2 A cross-section of the Majorana Demonstrator. The germanium detectors are contained within two ultrapure electroformed copper cryostats. Each cryostat contains seven closely packed stacks of detectors, called strings, with up to five detectors comprising each string. In order to reduce further the background the Majorana Demonstrator also has a series of passive and active shielding. 9

2.3 Nonrelativistic and relativistic s and d orbital energies for the mercury and the superheavy element 112 derived from HF and DHF calculation. Relativistic effects splits orbitals d [1]. 13

2.4 Comparison between experimental and theory IP values for Cu, Ag and Au. The non-relativistic theory could not explain the experimental IP value of these elements. The included theories are Coupled Cluster CCSD(T) relativistic and Coupled Cluster CCSD non-relativistic [2, 1]. 14

2.5 Wigner-Seitz atomic radii for the actinides, the rare earths (lanthanides), and the 3d and 5d transition metals [3]. Plutonium sets a point of transition in radius for the actinides between its low- and high-temperatures phases. . . . 15

2.6 Pressure–temperature–volume diagram of plutonium metal. The six solid allotropes at ambient pressure are the most of any element in the periodic table. 17

2.7 Pu composition can provide a "fingerprint" to identify its origin according to the $^{240}Pu/^{239}Pu$ atom ratios [4] 17

4.1 AMS facilities around the world and their terminal voltage. The 25 MV tandem accelerator from the HRIBF, ORNL is included as comparison. . . . 23
4.2 (a) MS diagram, molecules are one of the main limitations in MS, as they cannot be distinguished from the nuclide of interest when they have the same mass. (b) AMS diagram. AMS enables the analysis of isotopic ratios in some cases as low as 10^{-16}, six or seven orders of magnitude lower than most MS techniques [5]. 24
4.3 A schematic diagram of a typical Cs-sputtering ion source. A Cs reservoir is heated to produce a Cs vapor. Some of the Cs is ionized to Cs+ on a hot hemispherical tantalum surface. Cs+ ions are accelerated and focused on to the sample material. 28

5.1 The low energy section of the 25 MV Tandem at ORNL consists of a single cathode Cs ion source, a 90° injection magnet and a faraday cup. 31
5.2 Heavy Ion Accelerator Facility (HIAF) layout. The pelletron tandem accelerator services 7 beamlines in the 14UD target area. For this work we use line 5 marked in the figure. 33
5.3 Schematic diagram of the 14UD Accelerator facility at the ANU. The negative ions are pre-accelerated at about 100kV towards the injection magnet where the isotope of interest is mass selected and accelerated towards the high voltage terminal, here the ions are stripped and molecules are dissociated. The now positive ions are mass selected by the analyzer magnet and then velocity filtered before arriving to the detector. 34
5.4 Schematic diagram of the time-of-flight detector system. The ions passing the Wien filter pass the MCP, the start detector which is enlarged in this figure for a more detailed view. The stop detector is a silicon detector 2.3 m away from the MCP [6] 37
5.5 Sample size and shape to fit the target holder of the cathode wheel. 37

5.6 Aluminum cathode wheel in the MC-SNICS used for the Cu measurements. Commonly for AMS measurements a copper wheel is used, however for our measurements the Cu wheel was not chosen as it can potentially create strong backgrounds. 38
5.7 Beam intensity comparison for ultrapure Cu sample. The beam extracted from $^{238}U^{63}Cu$ was more stable than the beam extracted directly as U. . . . 40
5.8 Overlay of $^{238}U^{+5}$ and $^{232}Th^{+5}$ 2D histogram of energy vs time of flight showing the events detected in ultrapure Cu sample. 40

6.1 Excitation schemes for resonance ionization, two-step resonant excitation is taken as an example. The final ionization can be achieved by three different processes: non resonant, autoionizing and Rydberg states. 44
6.2 Cross sectional side view of the hot-cavity ion source assembly showing the main components of the source and the direction of the laser and ion beams. 44
6.3 Representation of the laser beam path from the laser room to the hot cavity ion source located in IRIS2. 45
6.4 The three Ti:Sa lasers at ORNL. The main components are labeled: ① Photonics Nd:YAG pump laser and pumping beam optics; ② Lens; ③ Ti:Sapphire crystal; ④ Pockel cells; ⑤ Grating; ⑥ Lens; ⑦ Second-harmonic generation (SHG) crystal; ⑧ Beam optics for SHG; ⑨ Laser beam exit; ⑩ Chiller tubes. 48
6.5 Typical tuning curve of the Ti:Sa lasers [7]. The peak on the curve is at 2.5 W peak near 810 nm. 49
6.6 RIMS setup at the Oak Ridge National Laboratory. Individual elements of the system are labeled by numbers: (1) Hot cavity ion source, (2) Electrostatic Steering (ES) 1, (3) Faraday cup (FC) 1, (4) Electrostatic quadrupole (EQ) 1, (5) Low resolution magnet, (6) ES 2, (7) EQ 2, (8) Slits, (9) FC 2, (10) High resolution magnet ($m/\Delta m = 1000$), (11) Slits, (12) FC 3, (13) ES 3, (14) EQ 3, (15) FC 4 (16) Laser beams entering the beamline through a vacuum window. 50

6.7 In order to perform fine tuning of the lasers I created this GUI interface to operate the New Focus 8752 picometer drivers remotely. Each picometer driver can control three motors for x, y and z movement. This interface allowed the movement in different step sizes and saved the current position for each motor for each driver. It also allowed us to go back to the saved position with the reset button. The output window showed the errors caused by the user. 51

7.1 Layers of packaging for the 1 mg of ^{242}Pu. The inspection was carried out by the Physics Division radiation control technician (a) 5 gallon drum shipping package, (b) Exterior packaging around the Teflon bottle (c) The 30 ml Teflon bottle, (d) 1 mg of ^{242}Pu 54

7.2 Hot laboratory at the physics division for the preparation of the Pu sample. PPE consisted on body and feet coverall, 2 pair of gloves and glasses. From left to right: Scotty Matthews (RCT), Dr. Galindo-Uribarri and Elisa Romero. 55

7.3 Summarized steps of drying the ^{242}Pu sample in Zr foil. (a) Placing Zr foil in hot plate and heating it up, (b) Depositing solution drops on the Zr foil using the micropipette, (c) Waiting for the solution to dry, (d) Folding the Zr foil with the dried sample on it. 60

8.1 Measured λ_2 scan spectra with 20 resonance peaks observed, λ_1= 420.76 nm, λ_3= 763.07 nm. Light ping vertical lines help to guide the eye in the locations of the peaks. About 20 peaks were identified, in total 6 peaks were chosen for a third step scan. 63

8.2 Third step ionization scans for (a) E_2= 35568.888 cm^{-1}, (b) E_2= 35790.806 cm^{-1}, (c) E_2= 35977.442 cm^{-1}, (d) E_2= 136313.781 cm^{-1}, (e) E_2= 36452.504 cm^{-1}, (f) E_2= 36689.646 cm^{-1}. 65

8.2 Figure 8.2 continued. 66

8.3 Comparison between three step scans with GS (ground state), λ_2= Peaks 1, 3, 6, 19 of Table 8.1. The current was measured under the same experimental condition in FC3. The current was normalized to λ_2=Peak #1, λ_3=750.24 scheme since it has been used previously in the literature [8]. We observed peaks 2-5 times larger than the one reported in literature. 67

8.4 The highest yield three-step, three-photon ionization scheme in our searches for ^{242}Pu. This level was used for for the ionization efficiency measurement and sensitivities tests. 68

9.1 Saturation curves of the (a) first laser step, (b) second laser step, and (c) third laser step excitations via $E_2 = 35977.442$ cm^{-1} level. Dots represent the measured data and lines are fits to equation 9.3. We include a residual plot for each fitting. 72

9.1 Figure 9.1 continued. 73

10.1 Development of a typical efficiency measurement on ^{242}Pu. Blue line shows the efficiency measurement on a sample of 9.97×10^{15} atoms of ^{242}Pu. The sample was gradually heated and the signal of laser ions as well as of non-resonant background was recorded as a function of time. The surface ionization (non-resonant background) was measured by blocking the lasers, shown in red points. Magenta line shows how the evolution of the efficiency value and the green line shows the range of heating, with a maximum of 400 A. 76

10.2 Zoom in the spectrum to show the effect in the ion current after unblocking the lasers. The current jumps above the value that had initially before blocking the lasers 77

10.3 Ionization level schemes chosen for the efficiency measurements for (a) ^{232}Th, (b) ^{238}U and (c) ^{242}Pu. 79

11.1 Cutaway view of an electron multiplier detector. Basic operation schematics. 81

11.2 IRIS2 beamline end showing the channeltron detector installed after FC4. . . 82

11.3 Electronics diagram of system detection using the electron multiplier. 83

11.4 (a) Comparison between the channeltron counts of lasers blocked and unblocked using ^{242}Pu beam . The signal of the lasers blocked is enlarge 10^4 times for a better appreciation; (b) Comparison between the FC4 ion current of lasers block and unblocked using ^{242}Pu beam. We could not record a value for 250 A as we could not distinguish between background and signal; (b) Comparison between the FC3 ion current of lasers blocked and unblocked using ^{242}Pu beam. 85
11.4 Figure 11.4 continued. 86
11.5 Characterization of the background, we detect up to 500 counts/s using a very high value of cathode 380 A. The magenta line is the reference line at 500 counts/s. Each value of the cathode is marked, the maximum value was 380 A, we let it exhaust for some period of time. 87
11.6 Intensities of ^{242}Pu and ^{240}Pu showing laser effect by blocking the lasers, confirming we observed Pu. The fitted lines are to obtain the average counts observed for each isotope. 88

12.1 Stark - Coulomb potential for a Rydberg atom in a static electric field of 5.14kV/cm in the z direction. 93
12.2 We identified in total 4 series converging to the IP. In the case of Scheme C we could not identify the rydbergs exactly as the were perturbations. 97
12.3 IP values as a function of Z and their precision. Figure taken from [9] . . . 98
12.4 Identification of the Rydberg states with the graph n* vs quantum defect. As seen in the graphs, the Rydberg states group in a constant for the "right" IP value for (a) Scheme A and (b) Scheme B. 99
12.5 Rydberg-Ritz fit of (a) Scheme A series 1, (b) Scheme A series 2 and (c) Scheme B. (Top) Measured energies (dots) of the Rydberg states and calculated energies (solid line) using the fitted parameters. (Bottom) Fit residuals with experimental statistical uncertainties as the error bars. 100
12.5 Figure 12.5 continued. 101

12.6 Variation of maximum histogram counts at different energy limits for scheme A and B. The middle graph for each scheme shows a zoom across the central peak. The fitted Gaussian is plotted as the red curve. The position of this peak equals to E_{lim} = 48605.965 for scheme A, E_{lim} = 48605.539 for scheme B and E_{lim} = 48605.987 for scheme C. The bottom graph for each scheme shows the residual of the fitting. 101
12.6 Figure 12.6 continued. 102
12.7 IP values for the series of actinides. Experimental data is taken from [10]. The new experimental result for Pu of this work is included in red dot. . . . 106

A.1 Low energy setup from the 25 MV Tandem accelerator at ORNL. Consists of the Cs-sputter ion source SNICS II located in the stable injector, a high resolution magnet and a faraday cup. 133
A.2 Schematic diagram showing the main components of the AMS setup at CIRCE. 133
A.3 Spectra of C, Cu and Au using a Cs-sputtering ion at 8 kV pre-acceleration voltage and accelerated at an energy of 100, 40 and 35 keV respectively. In all three spectra is observed cluster formations. Carbon and gold show the same odd-even pattern found for Cu clusters. The spectra of Au presents another series belonging to $^{197}Au_n$+^{63}Cu, however the peaks are only observed in even numbers of n. 135

B.1 Comparison between the spectra of the natural Cu (above) and the spectra of enriched ^{65}Cu (below). The peak at 31.5 mass disappears in the spectra of enriched ^{65}Cu. 137
B.2 Schematic diagram of the experimental setup for AMS at the ANU. 138
B.3 Candidate elements for the search of doubly charged negative ions. 139

C.1 Layout of the PROSPECT experiment. Shown are the HFIR reactor core and the two antineutrino detectors, AD-I and AD-II. 141

Chapter 1

Introduction

Many of the contemporaneous unsolved problems in physics are closely interrelated and require a multidisciplinary approach to address them. These problems do not lie only in one box of classification, and to tackle them requires the use of tools from different fields of science. Examples of leading-edge research modern experiments trying to answer the great questions in physics include: LEGEND (neutrinoless double beta decay) [11]; KATRIN (neutrino mass) [12]; LUX (dark matter)[13]; and LIGO (gravitational waves) [14]. This thesis exemplifies the use of tools from different fields of science to address the stringent demands of two important topics in current physics.

The deep underground and rare event physics experiments are becoming a major area of global research. The sensitivity of experiments that involve neutrino detection or searches of direct dark matter, crucially depends on the background levels achieved. In the study of the nature of neutrinos a large number of experiments are being deployed in underground laboratories or at reactors and accelerators all over the world, [15, 16, 17, 18]. These experiments require a good signal to noise ratio to reach the sensitivities required to achieve the physics goals. Novel techniques in the development, construction, operation and analysis of these experiments are demanded. Low background radioactivity assay and purification of detector components and materials is required.

The need for ultra pure materials with a very low contamination level of radionuclides has been increasing. The background can be controlled through shielding and careful material selection and screening [19]. Different materials like lead, copper and water are

used for passive shielding to suppress external radioactivity (gammas, neutrons, muons). However, these materials can also contain radionuclides themselves. A significant background contribution originates from the primordial actinides thorium (Th) and uranium (U) and the progenies of their decay chains. The decaying daughter nuclides of their natural decay chains can create interfering signals in the detector.

Ultrasensitive analytical techniques are required for quantitative analysis of the unwanted impurities in these low-background experiments materials. The selection of analytical techniques to be used are specific on a case by case basis, depending on the background requirements for each experiment.

The initial motivation for this work comes from the search of neutrinoless beta decay. A brief description of this rare process and its importance in neutrino physics is presented in Section 2.3. The Majorana Demonstrator [15] and GERDA [20] are examples of current experiments to search for this process on ^{76}Ge with two different approaches to remove the background contamination

GERDA uses a veto system to remove background contamination. Majorana focuses in ultra-pure materials and ultra clean environments to avoid impurities. In the next chapter we will give a brief description of these types of experiments and their successor, LEGEND, which is the collaborative effort of than 50 institutions worldwide to perform a 1-tonne scale experiment.

Different trace detection techniques have been used to measure contaminant levels for these experiments [21], including Inductively Coupled Plasma Mass Spectrometry (ICP-MS), Gamma-ray Spectrometry and Accelerator Mass Spectrometry (AMS). ICP-MS requires chemical preparation [22] and thus it can add contaminants during the detection process. Gamma-ray Spectrometry of radioactive contaminants at low levels is disadvantageous when only a very small amount of a radio-pure sample is available as it requires large samples (on the order of kg). Also the sample measurements must be performed in a very controlled environment for a long period of time to obtain a statistically significant result.

I present the motivation and impact of improved methods of ultra-trace detection for neutrino underground experiments, and for the study of actinides and super heavy elements in Chapter 2.

In this work I concentrated in two techniques: AMS (Chapters 4 and 5) and Resonant Ionization Mass Spectrometry (RIMS) (Chapter 6). AMS is a technique known for its high sensitivity. It is used widely for applications like ^{14}C dating and other isotopes like ^{36}Cl and ^{129}I [23]. I give a short description of the AMS technique in Chapter 4 and present the experimental results for actinides in Chapter 5 and Appendix A and B; (Clusters and Search for doubly negative ions).

In order to meet the modern experimental demands, we wanted to develop a more efficient technique that can compete or surpass the sensitivity of AMS. I describe the technique of RIMS in Chapter 6 and in the last chapters 7-11 address the development of three of the most important aspects in ultra-trace detection using RIMS. This includes the development of new, highly efficient excitation schemes and efficiency performance as well as the implementation of a single ion counting device to test the sensitivity of the technique. Finally, the identification of several Rydbergs states led to obtain precisely the first ionization potential (IP) of Pu presented in Chapter 12.

Chapter 2

The Need for Highly Efficient and Sensitive Techniques: Two Examples

2.1 Introduction

Two of the most important topics in physics today are: a) neutrinoless double beta decay ($0\nu\beta\beta$) and b) the physical and chemical properties of very heavy elements and their origin.

The discovery of neutrino oscillations, and its implication of non-vanishing neutrino masses and the non-conservation of neutrino flavor, implies that the Standard Model is incomplete and needs generalization. The new physics responsible for neutrino masses and mixing remains unknown and will only be revealed once more experimental data, from different areas of fundamental physics research, becomes available.

Conservation laws are critical to an understanding of particle physics. Numerous searches for physics beyond the Standard Model incorporate searches for lepton number violation (LNV). The study of the $0\nu\beta\beta$ decay, is by far the most sensitive test of LNV [24]. The current searches for this process involve large size detectors (more than 1 ton of enriched material) and the use of ultra clean materials in their construction. More sensitive analytical techniques are needed in order to assess the purity of these materials as even minute traces of actinides can jeopardize the results.

The study of physical and chemical properties of actinides and transactinides has been identified as a major topic of research [25]. Efforts are aimed at developing quantum-

mechanical theories that correctly describe spin-orbit interactions and relativistic effects which will expand our ability to predict heavy element chemical behavior. Resolving the role of f-electrons is one of the grand challenges.

The synthesis of heavier elements (such as Pu with Z=94) started in the 1940's. Discovering new superheavy elements test nuclear theories regarding the ultimate limits of the periodic table of the elements and helps to better understand how nuclei are held together and how they resist the fission process. In the last few years 4 new elements have been included in the Periodic Table with oganesson (Z=118) being the heaviest known element. Superheavy element synthesis is done with heavy ion accelerators with fusion-evaporation reactions and transfer reactions. Probing the chemical properties of the new elements to elucidate how well they conform to the trends present in the Periodic Table is a very active topic. Recently, Ronald Garcia at CERN, has proposed high precision laser-based spectroscopic studies of radioactive molecules containing heavy and deformed nuclei which could reach unprecedented sensitivity in the detection of signatures of beyond the standard model physics [26]. This experimental techniques could be suitable for studying a broad range of atoms, ions, and molecules.

The transuranic elements are the chemical elements with atomic numbers greater than 92. All of these elements are unstable and decay radioactively into other elements making their detailed study of physical and chemical properties very challenging. Uranium is the heaviest element found on earth in significant quantities. The detailed studies involving heavier nuclei requires efficient and selective methods such as the ones presented in this thesis.

2.2 Neutrino Physics

Propelled by surprising discoveries from a series of pioneering experiments, neutrino physics has progressed dramatically over the past two decades. A major new achievement was the establishment of a non-zero mass in neutrino oscillation experiments. A diverse research program exploiting particle astrophysics, accelerator and reactor experiments has uncovered a new landscape in neutrino physics, with a promising future for continued discovery [27, 28,

29, 30, 31]. Recent results indicate that answers to some of the most significant questions about neutrinos lie within reach of the next generation of experiments. Physicists now know that neutrinos exist in three types and that they oscillate, i.e., they change type as they move in space and time [29]. The observed oscillations imply that neutrinos have masses. Many aspects of neutrino physics are puzzling, and the experimental picture is incomplete. Powerful new facilities are needed to move forward, addressing the fundamental questions: What is the origin of neutrino mass? How are the masses ordered (referred to as mass hierarchy)? What are the masses? Do neutrinos and antineutrinos oscillate differently? Are there additional neutrino types or interactions? Are neutrinos their own antiparticles?

Researchers from the Oak Ridge National Laboratory and the University of Tennessee are currently involved in a broad and exciting neutrino program:

- Two surface based shallow neutrino experiments:
  - The Precision Oscillation and Spectrum Experiment (PROSPECT) located at the High Flux Isotope Reactor (HFIR) aimed to study the antineutrinos produced by a nuclear reactor (Appendix C).
  - The study of CEνNS (Coherent Elastic Neutrino-Nucleus Scattering) using the high-quality pion-decay-at-rest neutrino source at the Spallation Neutron Source (SNS).
- One deep underground experiment:
  - Large Enriched Germanium Experiment for Neutrinoless $\beta\beta$ decay (LEGEND), which precursor is the Majorana Demonstrator (MJD)

The COHERENT collaboration recently published the first observation of CEvNS; for more information about this important process and results refer to [32].

The neutrino is a subatomic particle notorious for its ability to slip through matter without interacting making its detection extremely difficult. The "shallow" experiments such as PROSPECT and COHERENT share common challenges such as having to operate on a high background environment. The reduction of background for these experiments

relies on various strategies that include local shielding, segmented design, correlated event selection, etc. The advantages are the close proximity to very intense neutrino sources.

The main motivation for this work comes from the $0\nu\beta\beta$ experiment, specifically with the backgrounds associated in this process. In the next section I will give a brief description of the $0\nu\beta\beta$ and the challenges associated with it. The strategy to reduce backgrounds on the deep underground experiments involves the use of ultra-pure materials.

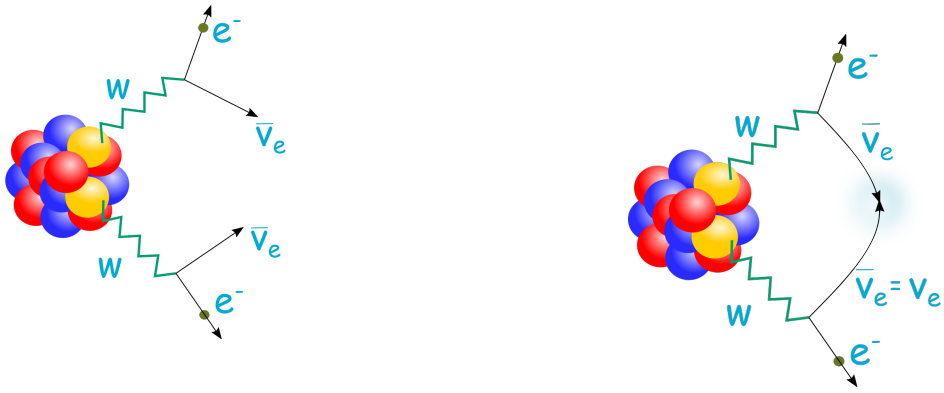
2.3 Neutrinoless Double Beta Decay

Although neutrino oscillations have established that neutrinos have mass, oscillations do not probe the absolute neutrino mass scale. In particle and nuclear physics, the only avenues for this are tritium beta decay [12] and neutrinoless double-beta decay.

Conventional (two-neutrino) double-β decay has been observed in 11 nuclei [33]. It is a rare decay process whereby the nuclei of certain isotopes decay and emit two electrons and two neutrinos. In order for (double) beta decay to be possible, the final nucleus must have a larger binding energy than the original nucleus. However, neutrinoless double-β decay, in which no neutrinos are emitted, could occur only for Majorana neutrinos (Figures 2.1a and 2.1b).

The Majorana nature of the neutrino could be confirmed by finding evidence of this elusive process. Like everything else that involves neutrinos, this is not easy. The smallness of neutrino masses guarantees that the decay is extremely rare, in other words, the half-life of the candidate nucleus is exceedingly long. $0\nu\beta\beta$ decay experiments therefore must observe a large quantity of a candidate isotope (approximately 1 ton scale) in the hope of seeing a handful of decay processes [34].

However, the $0\nu\beta\beta$ decay candidate isotopes are often rare in nature and need to be separated from other isotopes of the same element, which is already quite a complex enterprise. Furthermore, experimental backgrounds can produce electrons in the energy range that look similar to those expected from $0\nu\beta\beta$ decay. In particular, there are major backgrounds from cosmic rays and natural radioactivity of elements such as uranium and thorium, elements present in Earth's crust that cause unavoidable contamination of all



(a) **(b)**

Figure 2.1: Schematic diagram for (a) $2\nu\beta\beta$ decay and (b) $0\nu\beta\beta$ decay.

matter around us. The strategy adopted for suppressing these backgrounds involves many factors spanning from building the detectors underground to the use of ultrapure material to shield the detectors.

ORNL is a lead Laboratory for the Majorana Demonstrator (MJD). The MJD experiment is an approximately 40-kg detector array made from enriched ^{76}Ge and natural germanium and is built to demonstrate the feasibility of a future one-ton-scale $0\nu\beta\beta$ decay experiment [15]. MJD is located underground at the level of 4850 ft at the Sanford Underground Research Facility (SURF) in Lead, SD. The Majorana collaboration is working cooperatively with a similar scale prototype experiment in Europe called GERDA [16].

A future tonne-scale $0\nu\beta\beta$ experiment is one of the highest priorities or the US Nuclear Physics community and the US High Energy Physics as indicated in the latest Long Range Plan for nuclear science in the US by the Nuclear Science Advisory Committee (NSAC) [35] and the Strategic Plan for U.S. Particle Physics in the Global Context (P5 report) [36]. Members of the MJD, GERDA and others, have formed a single collaboration towards building a 1 tonne experiment to search for $0\nu\beta\beta$ [37]. Proposed future ton-scale experiments aim to achieve sensitivities of 10^{27} years, corresponding to observing about five nuclear decays per year in a detector with a ton of material.

In order to achieve the ultra-low backgrounds required, we must go to extreme lengths. The experiments have to be constructed and operated deep underground to avoid background from cosmic rays. In the case of MJD, detector mounts and cryostats are made from ultra-

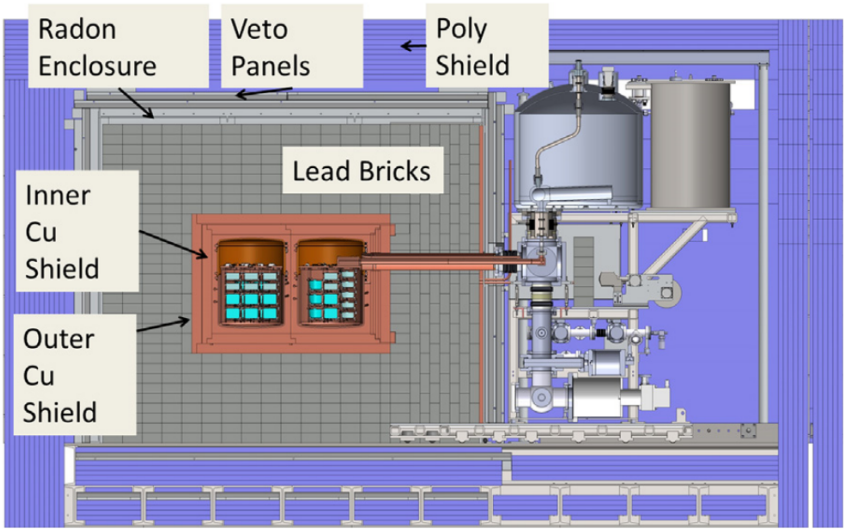


Figure 2.2: A cross-section of the Majorana Demonstrator. The germanium detectors are contained within two ultrapure electroformed copper cryostats. Each cryostat contains seven closely packed stacks of detectors, called strings, with up to five detectors comprising each string. In order to reduce further the background the Majorana Demonstrator also has a series of passive and active shielding.

pure copper that has been electroformed and machined underground [15], Figure 2.2. Monte-Carlo simulations are used to calculate radio-purity specifications for the different materials used in the experiment. The most stringent requirement is that for the underground-electroformed copper, for which the required purity levels are $< 2.4 \text{ x } 10^{-14}$ g ^{238}U/g Cu and $< 7.5 \text{ x } 10^{-14}$ g ^{232}Th/g Cu [38]. These levels are below limits achievable by direct counting assay techniques.

A direct assay of copper represents a significant challenge for any analytical techniques to provide the wide dynamic range that would be necessary to handle the large amount of background generated from the copper matrix. In Chapter 3 I will give an overview of the techniques that have been used for ultra-trace detection.

2.4 Actinides

The search for super heavy elements has been an exciting endeavor for nuclear scientists for many decades. There are still question whether they will follow the periodic table trend or if

the relativistic effects will lead to dramatic deviations. Their study is complicated by small production rates of single atoms-at-a-time and by short half-lives [39].

The periodic table of the elements has served generations of scientists as the tool of choice for ordering the 118 known chemical elements. Russian chemist Dmitri Mendeleev published the first recognizable periodic table in 1869, developed mainly to illustrate periodic trends of the then-known elements. He also predicted some properties of unidentified elements that were expected to fill gaps within the table. Mendeleev's idea has been slowly expanded and refined with the discovery or synthesis of further new elements and the development of new theoretical models to explain chemical behavior.

Since the discovery of nuclear fission in 1938 [40], researchers have artificially created 26 new elements and hundreds of isotopes, all by using nuclear reactions to modify the properties of existing nuclei. Recently in 2016, four new synthetic elements with atomic numbers Z = 113 (nihonium), 115 (moscovium), 117 (tennessine) and 118 (oganesson) joined the periodic table [41, 42]. They were all produced between 2002 and 2006 using heavy-ion fusion reactions. The road to the final confirmation took a decade and a significant and dedicated experimental effort worldwide.

Uranium is the heaviest element found on earth in significant quantities, and nowadays oganesson (Og) with atomic number Z = 118 is the heaviest known element. The half-life of Og is 0.89 ms, which is currently too short for chemical studies [39].

Despite much recent progress, scientists are still learning how to consistently describe the structure and properties of atoms and nuclei. Experimental studies of the heavy elements and nuclei continue to yield new data that challenge and inform theoretical models of atomic and nuclear structures. The heavy elements like actinides are an ideal field to study the influence of relativistic effects on chemical properties.

The spectrometry of the actinides presents a challenge to experimentalists and theoreticians alike. After Cm the actinides are only available in small quantities, they may be highly toxic and their spectra may be contaminated by the products of nuclear decay. Theoretical calculations on actinides properties face substantial deviation due among other reasons to strong relativistic effects. However the efforts for studying them is growing and various analytical methods have been developed and are being utilized by laboratories around

the world to meet the challenge of providing increasingly sensitive, precise, and accurate information in actinides. The application on the study of actinides includes numerous fields from environmental monitoring [43, 44, 45, 46], search for extinct or primordial radionuclides in nature [47, 48, 49] as well as determination of ionization potentials [50, 51, 52, 53, 54, 55] and their detection in ultrapure materials for underground experiments as described in Section 2.2.

Actinides are radioactive elements ranging from atomic number 89 through 103. First identified as a new row in the Periodic Table by Seaborg in the 1940s [56, 57], most actinides are highly reactive metals with a wide range of valence states and physical properties [25]. They are analogous to the lanthanides and result from the filling of the 5f orbitals [58], as the lanthanides result from the filling of the 4f. Thorium and uranium are the only actinides that occur in substantial quantities in nature.

Actinide elements up to ^{96}Cm are available in significant quantities synthetically, owing to their production in nuclear power reactors leading to their presence in spent nuclear fuel. Heavier elements need to be produced artificially to make them available for scientific research. All actinides heavier than uranium were discovered using other actinides as targets [59]. The slow neutron capture process (s-process) in research reactors is route to artificially produce actinides, one of the production facilities is the High Flux Isotope Reactor (HFIR) at Oak Ridge National Laboratory (ORNL) in Oak Ridge, TN, USA.

The dominant feature of the actinides is their nuclear instability, as manifested in their radioactivity (mostly decay) and tendency to spontaneous fission: both of these modes of decay become more pronounced (shorter half-lives) with the heavier elements. Every known isotope of the actinide elements is radioactive and the half-lives are such that only ^{232}Th, ^{235}U, ^{238}U and possibly ^{244}Pu could have survived since the formation of the solar system.

Measurements on ^{244}Pu from Earth's deep sea reservoir had suffer for the low efficiency of production of ^{244}Pu, using AMS techniques [49]. ^{244}Pu and ^{60}Fe [60] have been of considerable interest for some time as they can give insights in the nucleosynthesis of heavy elements. A more suitable analytical method is needed to address ultra-trace detection of ^{244}Pu.

2.5 Relativistic Effects and Determination of Ionization Potential of Heavy Elements

Until the 1970's it was generally accepted by scientists, including Nobel Prize winners P. Dirac and Sheldon L. Glashow, that for a description of the electronic structure of atoms and molecules relativistic theory was not needed [61, 62]. During the last four decades the situation changed considerably. Presently, it is generally accepted that relativistic effects must be considered for describing the chemical and physical properties for atoms, molecules and ions containing heavy elements. Even understanding of the periodic table is impossible without utilizing the ideas of theory of relativity. Relativity is increasingly important for molecules containing an element with high atomic number.

A particular example of relativistic effects can be showed with Cu, Ag, and Au elements used in coin production. The prediction of the fundamental property for the elements, the ionization potential IP, was not explained with non-relativistic theories. It was expected following the periodic table trend that $IP_{Au} < IP_{Ag} < IP_{Cu}$. However, experimental results show that the IP value for Au is the largest of these three elements. This result can be understood by implementing relativistic effects in theory calculations, Figure 2.4. Many properties, even the yellow colour of the metallic gold, are caused by relativistic effects [63]. The three main relativistic effects are:

- Relativistic shrinking and stabilization of s orbitals (and to a lesser extent also p orbitals).
- The spin–orbit splitting of p, d, etc. orbitals, see Figure 2.3.
- The relativistic self–consistent expansion and destabilization of d and f orbitals.

Electrons in d and f subshells are far from the nucleus and their velocities are much lower than the speed of light. Therefore, the last effect, relativistic radial expansion and destabilization of the d and f electronic shells are indirect and follows from relativistically affected screening of nucleus by s and p electrons. Since their radial distribution shrinks, the d and f subshells expand. Now, since inner shell 1s electrons of Au move near the

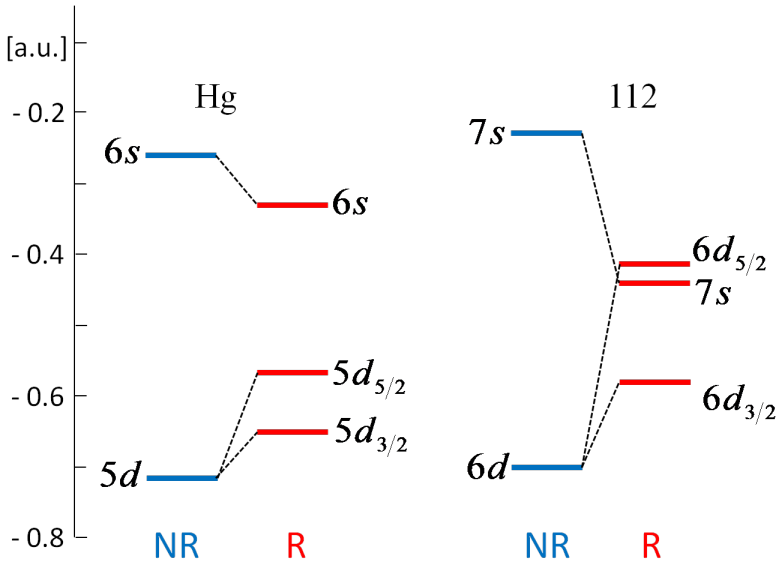


Figure 2.3: Nonrelativistic and relativistic s and d orbital energies for the mercury and the superheavy element 112 derived from HF and DHF calculation. Relativistic effects splits orbitals d [1].

nucleus with the velocity comparable to the speed of light, these electrons are relativistically stabilized and the corresponding orbitals shrink. In many–electron systems all electrons up to valence electrons "feel" this effect, being stabilized and shrunk as well. Consequently, removing an electron from the valence 6s orbital is hindered by this stabilization and leads to an enhanced ionization potential. The same mechanism explains a relativistically enhanced electron affinity (EA) of coinage metals and particularly of Au, so that Au has a larger electron affinity than other coinage metals [64].

Relativistic alteration in the electron correlation contribution is also proportional approximately to $Z^2\alpha^2$ where $\alpha = 1/c$, consequently relativistic effects are very complex for many–electron systems. For this reason a precise experimental values for IP of heavy elements like plutonium can be the benchmark for improvements in relativistic theory models to understand atomic properties of heavy and super heavy atoms. The heaviest that the IP has been measured is Lawrencium [65].

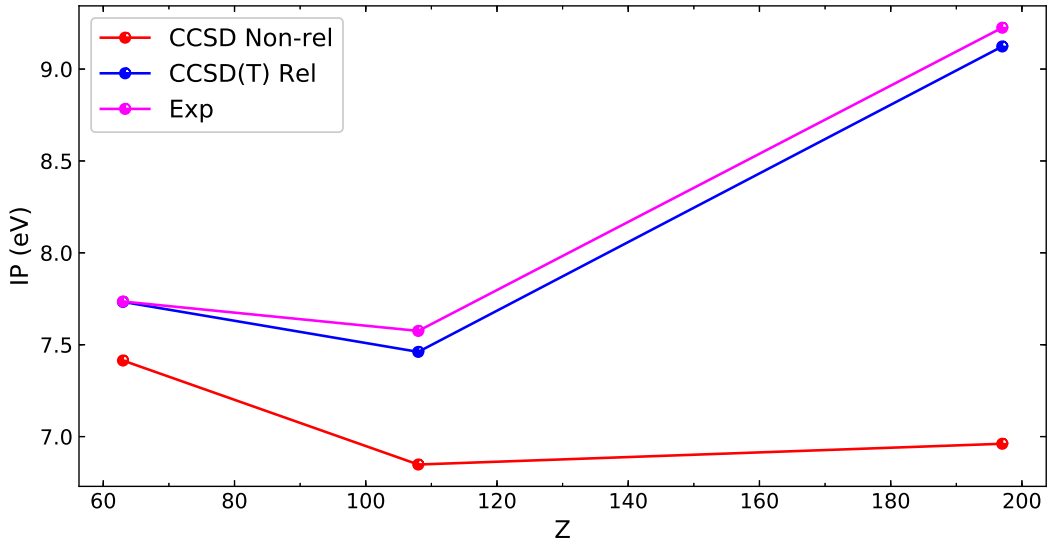


Figure 2.4: Comparison between experimental and theory IP values for Cu, Ag and Au. The non-relativistic theory could not explain the experimental IP value of these elements. The included theories are Coupled Cluster CCSD(T) relativistic and Coupled Cluster CCSD non-relativistic [2, 1].

2.6 Plutonium: History and Properties

Plutonium was first produced late in 1940 by Seaborg [66] by bombarding uranium with deuterons to produce the isotope ^{238}Pu. In March 1942, element 94 was named "plutonium" with the chemical symbol "Pu". Plutonium was named after the planet Pluto, following the pattern used in naming neptunium [67].

In 1942, Cunningham and Werner succeeded in isolating about 1 μg of ^{239}Pu, which was prepared by cyclotron irradiation of 5 kg of uranyl nitrate [68]. This experiment made plutonium the first man-made element to be obtained in a visible quantity, by 1944 the first kilogram quantities of Pu were being produced. Plutonium is now produced in much larger quantities than any other synthetic element. At the end of 2014 almost 2630 metric tons of plutonium were estimated to exist worldwide. Most of this plutonium (2390 metric tons) is found within used fuel from nuclear power plants [69].

The transuranic element, plutonium is a complex and fascinating element. It sits at an important transition point in the periodic table, separating the light actinides with itinerant

(bonding) 5f electrons from the heavy actinides with localized (chemically inert) 5f electrons [58]. The transition occurs right at plutonium, between its low- and high-temperature phases as shown in Figure 2.5. As a result, plutonium is notoriously unstable with temperature, pressure (stress), chemical additions, and time (especially because of its self-irradiation) [3]. A very interesting physical property of Pu is that exists in six allotropic modifications under ordinary pressure, and there is a seventh phase that exists under high pressure [70] (Figure 2.6). The six solid allotropes at ambient pressure are the most of any element in the periodic table.

Plutonium in the Earth's surface environment consists principally of five isotopes: ^{238}Pu ($t_{1/2}$ = 87.74 y), ^{239}Pu ($t_{1/2}$ = 24,110 y), ^{240}Pu ($t_{1/2}$ = 6563 y), ^{241}Pu ($t_{1/2}$ = 14.4 y) and ^{242}Pu ($t_{1/2}$ = 373,000 y). Plutonium isotopic compositions are well-known to vary according to the mode of production of this element; expected ranges for$^{240}Pu/^{239}Pu$ atom ratios are summarized in Figure 2.7. The Pu isotopic composition can therefore provide a "fingerprint" of different sources and is useful in studies of the movement of a specific point or regional source. Conventional techniques to measure the Pu ratios can have problems in separating isobars like ^{238}Pu from ^{238}U , background suppression or the decay-counting is very slow [71].

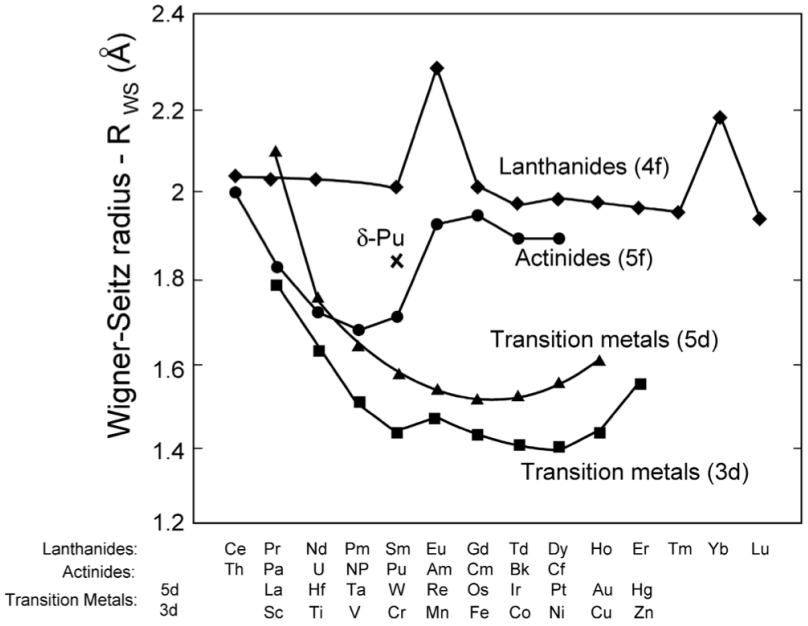


Figure 2.5: Wigner-Seitz atomic radii for the actinides, the rare earths (lanthanides), and the 3d and 5d transition metals [3]. Plutonium sets a point of transition in radius for the actinides between its low- and high-temperatures phases.

Plutonium-239 is the most important isotope of plutonium. Its half-life (24,110 years) is sufficiently long to permit the preparation of this isotope in large-scale amounts, and to make it feasible to carry out conventional scientific studies. ^{239}Pu has a high cross-section for fission with slow neutrons, and is the isotope that serves as nuclear fuel for both nuclear power and nuclear weapons. By far the greatest portion of the knowledge of the chemical and physical properties of plutonium has been acquired by the use of ^{239}Pu.

Evidence suggests that large amounts of primordial ^{239}Pu and ^{244}Pu ($t_{1/2} = 8.3 \times 10^7$ y) were present at the time of the Earth's origin. In fact ^{244}Pu serves as a clue to understand the formation of the heavy elements, which are primarily generated in stellar explosive environments. The production of the heaviest elements requires a very short and intense burst of neutron (rapid neutron capture or r-process). The requisite neutron fluxes can be provided by supernova explosions or binary neutron-star mergers. The neutron-star formation scenario is supported by observations of the Laser Interferometer Gravitational Wave Observatory (LIGO) [72, 73, 48] and by the measurements of the abundance of live ^{244}Pu in deep-sea reservoirs on Earth [49].

Reference [49], used AMS to search for live interstellar ^{244}Pu from deep sea reservoirs. They observed that the abundances of ^{244}Pu were lower than expected from continuous production in the Galaxy by about 2 orders of magnitude. With this technique they were able to detect 2 counts of ^{244}Pu for the deepest layers of the deep sediments, however their statistics could be limited by the low efficiency of the typically used Cs ion source. Motivated by the need of a higher efficiency and higher sensitivity detection system for experiments like mentioned above we investigated RIMS and the results are presented in the following in Chapters 6-12.

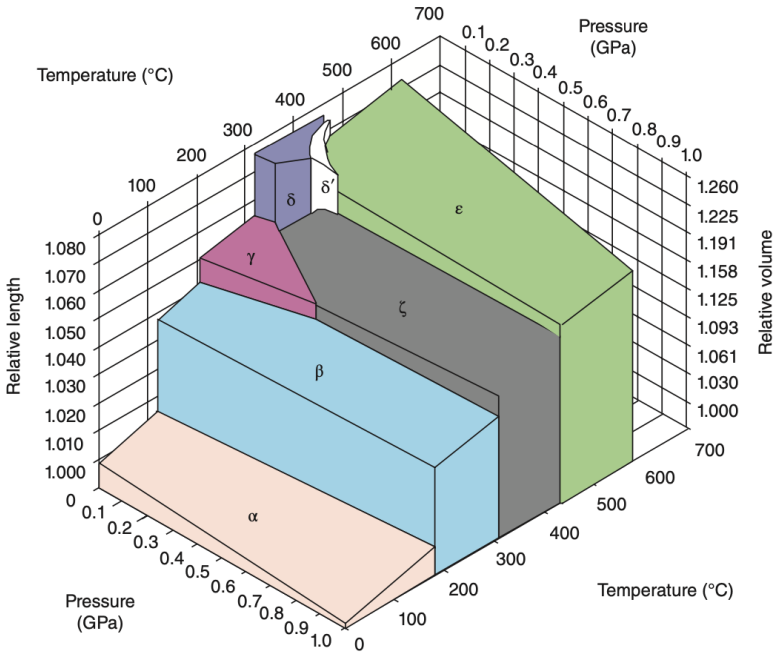


Figure 2.6: Pressure–temperature–volume diagram of plutonium metal. The six solid allotropes at ambient pressure are the most of any element in the periodic table.

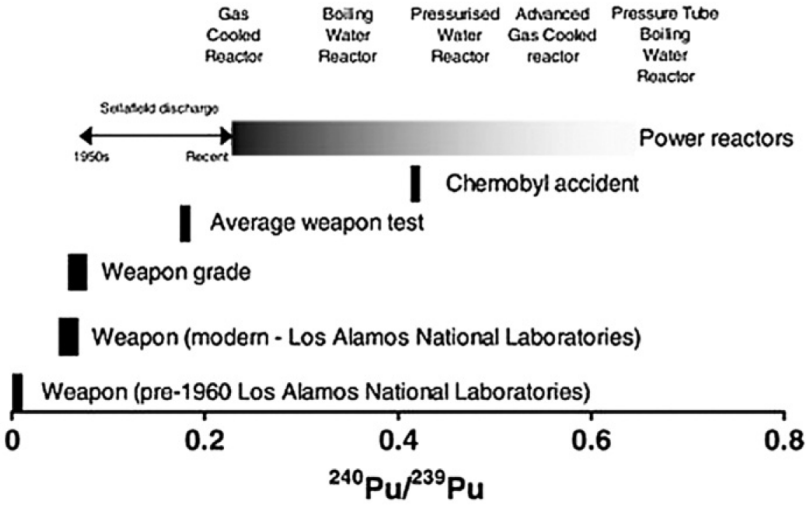


Figure 2.7: Pu composition can provide a "fingerprint" to identify its origin according to the $^{240}Pu/^{239}Pu$ atom ratios [4]

Chapter 3

Ultra-trace Detection Techniques applied in Actinides

Typical isotopic ratio analysis techniques applied in the actinides ultra-trace detection include ICP-MS, AMS and TIMS. Isotope ratio analysis requires a standard (a sample with a known amount of material, eg. for ^{236}U detection it is used ^{238}U) and blanks (to characterize the background of the detection system). The isotope of interest is present in trace amounts only in the sample material, so there is a low risk that the instrument might have contamination for that isotope. The challenges that this techniques can face come from limitation in sensitivity and isobaric interference. The techniques for this type of analysis are very well described in reviews available in the literature [23, 47, 74, 75, 76, 77].

In the case of ultra-trace detection of ^{232}Th and ^{238}U in ultrapure materials present an additional challenge: the isotopes ^{232}Th and ^{238}U account for nearly all natural U and Th with other isotopes occurring only as trace radioisotopes in nature. ^{232}Th and ^{238}U are considered almost stable ($\sim 10^{10}$ y) and are found everywhere. In the case of ultra-trace detection in ultra-pure materials the background is caused by the same ^{232}Th and ^{238}U isotopes. It would be highly desirable to develop a reference or a standard of the material that we want to analyze (ultra-pure Cu in this case) with a well known concentration of these isotopes. This can be done, for example, using gamma-ray spectroscopy in large quantities of the material [78]. A direct ultra-trace assay of pure materials therefore represents a significant challenge

for any analytical techniques to provide the wide dynamic range that would be necessary to handle the large amount of background generated from the material matrix.

The main methods for measuring the amount of radioactive contaminants in materials used for underground experiments are gamma-ray spectrometry, which measures the decay of the daughter nuclides [79] and ICP-MS which detects the nuclides directly [80, 81].

Currently, many laboratories are engaged in the field of Ultra Low-level Gamma-ray Spectrometry (ULGS), i.e. with additional background reduction by using anti-muon shields or underground laboratories [82]. However a drawback in applications of ULGS is that the measurements are very time consuming. In order to measure total activities of less than 1mBq, it is rarely enough to measure a sample for a day or two and consequently measurement throughput is low. Additionally this technique has a sensitivity limit of the order of μBq/kg [83]. For ultrapure Cu the levels of U and Th are $< \mu$Bq/kg.

In 2015 the Pacific Northwest National Laboratory (PNNL) group developed a technique to assay U and Th in ultrapure copper using ICP-MS, [22]. Efforts focused on the use of ion exchange resins to selectively concentrate the analyte or remove the copper matrix. After significant investments in the assay capability, these efforts revealed that the Th and U background found ubiquitously at these unprecedented concentration levels limited the sensitivity of the assay. In the absence of a direct assay capable of the target sensitivity, the experiment has had to rely on an assay of the bath electrolyte to infer the electroformed material purity. This indirect technique depends on the role of U and Th electrolyte concentrations in determining their concentration in the deposited copper. It would be desirable to directly measure the actinides in the Cu with a minimum sample preparation (ie. chemistry).

We employed Accelerator Mass Spectrometry (AMS) (Chapter 4) to evaluate the U and Th impurities in the ultra-pure copper materials Chapter 5. AMS is presently one of the most sensitive techniques for isotope analysis. AMS is a highly sensitive method of counting atoms. It is used to detect very low concentrations of natural isotopic abundances (typically in the range between 10^{-12} and 10^{-16}) of both radionuclides and stable nuclides. New generation AMS enables the heaviest elements (actinides) to be detected reaching outstanding sensitivities for long-lived isotopes. Mass-spectrometric methods (e.g. AMS,

TIMS, ICP-MS) can be sensitive to molecular interferences, however the main advantage of AMS compared to conventional MS (TIMS, ICP-MS) is the complete destruction of molecular isobars (e.g. ^{238}UH for ^{239}Pu) by stripping to high positive charge states in the terminal of the tandem accelerator. AMS can minimize the sample size requirements (mg and even sub-mg size) due to its low detection limit and shorter measuring times (less than 1 hr). Further, chemical preparation it is not necessary in most of the cases, thus there is no risk of adding contamination. Specific details of AMS experimental setup used in this work is described in the next chapter.

Important disagreements between AMS and ICP-MS have been reported in the literature. Such was the case with the claim of a positive result for the search of superheavy element with Z=122 and A=292 in a sample of natural thorium using ICP-MS [84]. This claim was not confirmed in subsequent studies using AMS [85]. It is possible that the signals interpreted by [84] were molecular background, which is not entirely suppressed in ICP-MS.

AMS has been used only very rarely to detect ultra low concentrations of trace elements and primordial actinides [78]. In Chapter 5 I present the development of activities geared to optimize the implementation of an AMS system by systematically studying the factors that affect the sensitivity and accuracy of the technique. We explored the conditions for the detection of U and Th using an AMS system with a Cs-sputtering source. However, a drawback for this technique is the ionization efficiency of the Cs-sputter ion source, commonly used for AMS, is of the order of 0.01-0.1% for actinides [86, 87, 88, 89] and its high experimental expenditure. There is considerable synergy between the fields of AMS and production of radioactive ion beams (RIBs) as demonstrated in our previous work on ^{36}Cl [90], ^{26}Al [91], laser photodetachment with S and Cl [92], and in the development of more efficient ion sources [93].

In this work we also explored Resonance Ionization Mass Spectrometry (Chapter 6) technique using a resonant ionization laser ion source (RILIS) that was developed for use at RIB facilities. RILIS uses multiple lasers to stepwise, resonantly excite atomic species to higher energy levels followed by ionization in the last transition. Since each element has its own unique set of atomic energy levels, the resonant excitation and ionization process can provide nearly 100% elemental selectivity and can be highly efficient. In Chapters 8-12 I

present the results of the development of more efficient three-step level schemes, efficiency measurements and sensitivity limits.

Chapter 4

Accelerator Mass Spectrometry

4.1 Introduction

Accelerator Mass Spectrometry (AMS) is presently one of the most sensitive techniques for trace elemental and isotope analysis. AMS is a highly sensitive method of counting individual atoms. It is used to detect very low concentrations of natural isotopic abundances (typically in the range between 10^{-12} and 10^{-16}) of both radionuclides and stable nuclides. The equipment used for AMS is almost exclusively based on the electrostatic tandem accelerator.

The principal difference between AMS and conventional mass spectrometry (MS) lies in the energies to which ions are accelerated. In MS, the energies are thousands of electron volts (keV) whereas in AMS they are millions of electron volts (MeV). As a consequence, the high energies of AMS allow to remove ambiguities in identification of atomic and molecular ions with the same mass. The capability of AMS in extremely sensitive radioisotope measurements has been extensively demonstrated over the past 30 years. For example, AMS has allowed refinements in the technique of ^{14}C dating in the fields of archeology and geology and in the measurement of ^{36}Cl in seawater samples (ratios ^{36}Cl/Cl$= 10^{-16}$) in the field of oceanography [94].

AMS was proposed for the first time by Luis Alvarez and his student Robert Cornog in 1939 [95, 96] which used a cyclotron to identify ^{3}He in Helium. Under its actual form, however, AMS appears by 1977 [97] as a way to solve the limitations of conventional radiometric techniques for ^{14}C dating. After this moment it has rapidly evolved to find

application in many disciplines described in review articles [98, 99, 100, 101, 102]. More than 40 laboratories have developed AMS systems, in Figure 4.1 it shown the facilities per continent and their terminal voltage. For comparison I included the 25 MV Tandem accelerator of ORNL, it was the most powerful tandem of the world.

4.2 Principles of AMS

AMS can be considered an extension of Mass Spectrometry (MS) that includes the use of a low energy mass spectrometer, an accelerator and high energy mass spectrometer. In Figure 4.2, a MS system is compared with a simple AMS system. The introduction of the tandem accelerator, followed by several ion-filtering devices reduces the background considerably.

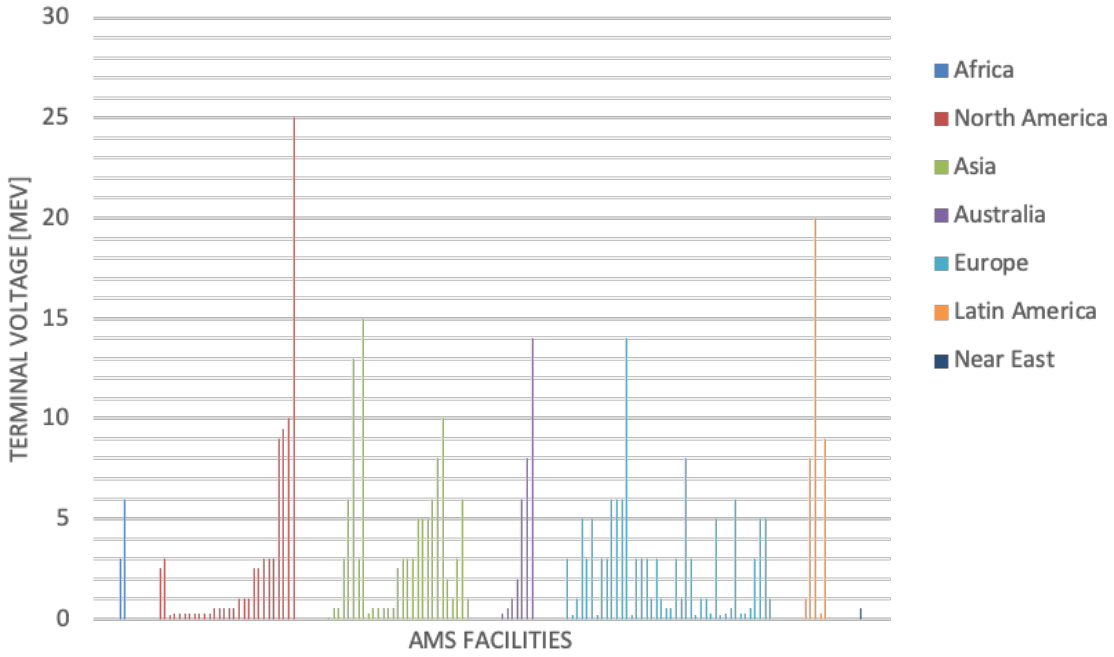


Figure 4.1: AMS facilities around the world and their terminal voltage. The 25 MV tandem accelerator from the HRIBF, ORNL is included as comparison.

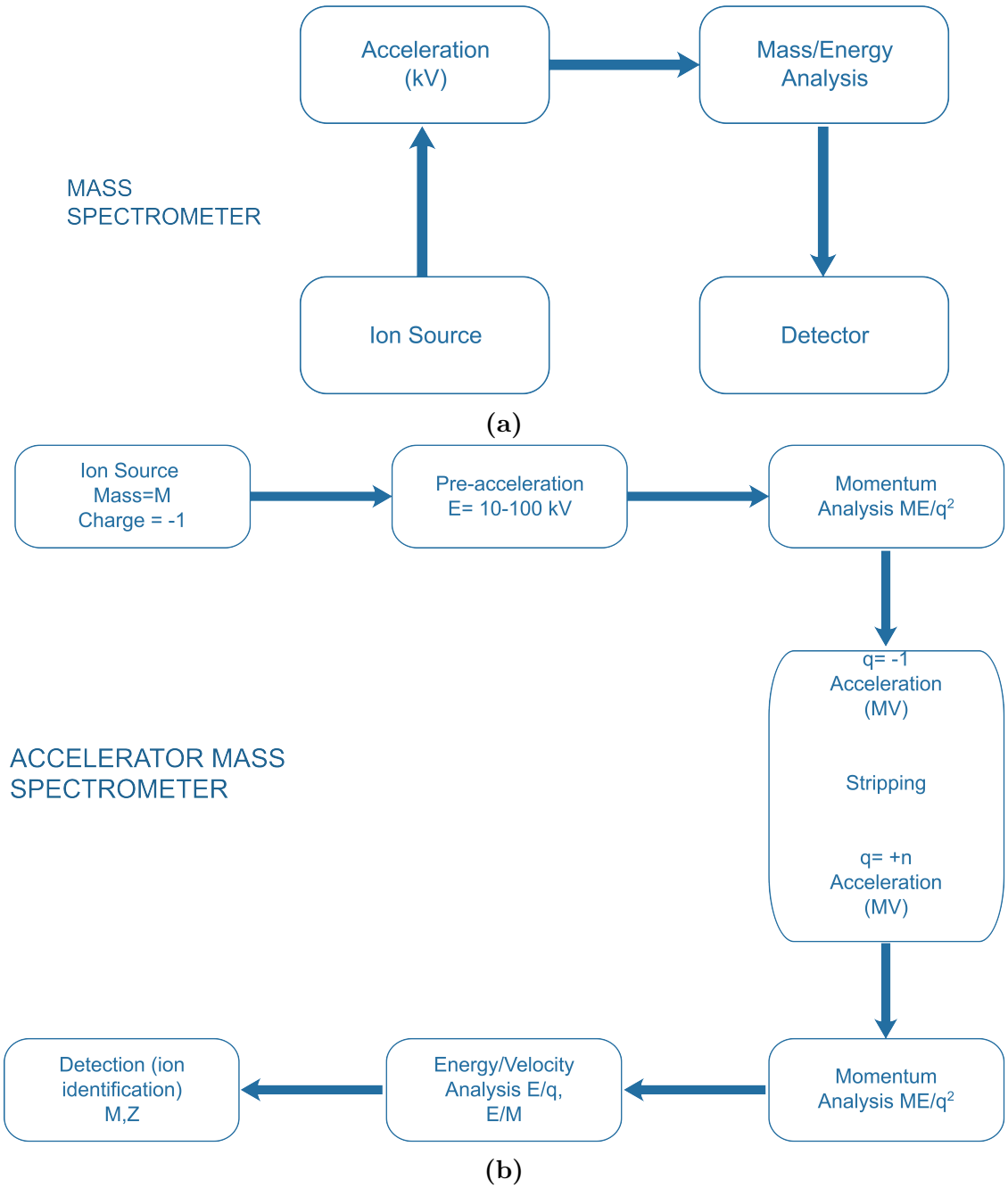


Figure 4.2: (a) MS diagram, molecules are one of the main limitations in MS, as they cannot be distinguished from the nuclide of interest when they have the same mass. (b) AMS diagram. AMS enables the analysis of isotopic ratios in some cases as low as 10^{-16}, six or seven orders of magnitude lower than most MS techniques [5].

In MS, Figure 4.2a, ions of charge q are extracted from the sample material, accelerated to energy E and then separated according to atomic mass M using a uniform magnetic field B. The curvature radius r depends of M, q and E with the following relation:

$$\frac{2ME}{q^2} = (Br)^2 \tag{4.1}$$

The current of ions with the correct value of ME/q^2 is determined with a Faraday cup providing a measure of the concentration in the sample of atoms having atomic mass M. The limitations of MS are dramatically reduced when an ion accelerator is incorporated in a MS system. Energies of the order of MeV allow the complete rejection of molecular background through multiple electron stripping, reducing the probability of spurious events and reducing isobaric interference. A typical AMS includes the following features 4.2b.

- Production of negative ions in a multi-sample, negative-ion source. The sample material containing the rare isotopes to be counted is placed in the ion source.
- Acceleration of negative ions from ground potential to a high positive voltage.
- Recharging of all ions to positive by stripping off electrons and at the same time dissociation of all molecular ions.
- Acceleration of the now positive ions back to ground potential.
- The removal of unwanted ions using electric and magnetic fields.
- Identification and counting of the individual rare isotopes with nuclear detection techniques.
- Computer control of the accelerator system to provide control of the AMS system parameters.

The detection limits of AMS depends on the efficiency for producing the beam ions, the control of background in the AMS system, and the lower limit to sample contamination that can be achieved in the field and in the laboratory.

4.3 Ion Source

Tandem accelerators require a source of negative ions [103]. The probability of negative ion formation depends on electron affinity [64]. Electron affinity is the change in energy when a neutral atom in its gaseous form gains an electron to form a negative ion. Thus the number of isotopes that can be measured by tandem AMS is restricted since there are elements that do not form negative ions. However some elements in a molecular form with other element can form negative ions [104].

Most of the AMS systems use Cs-sputter ion sources to produce negative ions from a small solid sample containing the element of interest [105, 106, 103]. The samples are bombarded by 3-10 keV Cs ions that physically knock atoms and molecules out of the sample and contribute an electron to a fraction of the ejected particles, forming negative elemental or molecular ions. Figure 4.3 shows the commonly used Cs sputter ion source, Cs vapor from an oven hits the ionizer, the Cs atoms are ionized and the positive Cs ions are accelerated and focused on the sample, which is maintained at a negative potential compared to the ionizer, and atoms are sputtered from the sample. Neutral atoms, as well as positive and negative ions, will be sputtered from the sample surface.

4.4 Injection System

To match to the entrance optics of the accelerator, the negative ions are pre-accelerated to an energy of 10-30 keV for small accelerators (< 3 MV) and 50-150 keV for large accelerators (4-25 MV). Pre-acceleration to the required energy reduces the fractional energy spread of the beam and hence the emittance as it enters the accelerator. The ions are selected in mass by an injection magnet, which deflects ions along radii determined by their value ME/q^2.

4.5 Tandem Accelerator

The low-energy spectrometer before the tandem accelerator cannot resolve the small mass differences among the rare isotope and the nuclear or molecular isobars [107]. A tandem electrostatic accelerator solves the problem of these interferences in two ways: firstly

molecular isobars are removed by charge change from negative to multiply-positive ions in the dissociation cell within the high-voltage terminal of the accelerator; and secondly nuclear ions, even isobars, can be uniquely identified using simple counting detectors, but only at the high ion energies (> MeV) that can be reached through accelerators.

Tandem accelerators have the following basic features:

- Pressure tank filled with insulating gas
- Internal insulating column to support the high-voltage terminal and the other accelerator components
- Charging system with control to hold the terminal voltage constant
- Low- and high-energy accelerator tubes
- Thin foil or gas stripper placed in the high-voltage terminal between the low- and high-energy tubes to convert negative to positive ions

The negative ions accelerate toward the positive terminal of the accelerator. They pass through a thin carbon foil or a localized gas that removes electrons from the ion through collisions with the electrons in the stationary foil or gas, making positive ions. The negative ions that enter the tandem accelerator have energy $\mathrm{E}_i = V_i e$ where V_i is the total injection voltage and e the unit of charge and are accelerated to the high-voltage terminal with positive potential V_t. After the negative ions being converted to positive ions with charge q, are further accelerated by the same positive potential leaving the accelerator with energy $\mathrm{E}_i + (q+1)eV_t$. the ion energy E after acceleration in a tandem is given by:

$$E = ((V_i + V_t)M_p/M_i + qV_t)e \tag{4.2}$$

The positive ion mass M_p differs from the negative ions mass M_i if the latter is a molecular ion which dissociates at the stripper, otherwise $M_p = M_i$. From the positive terminal, ions of all elements in the incident beam are accelerated back to ground potential, attaining energies from a few MeV to more than 100 MeV, depending on their charge state and the accelerator voltage.

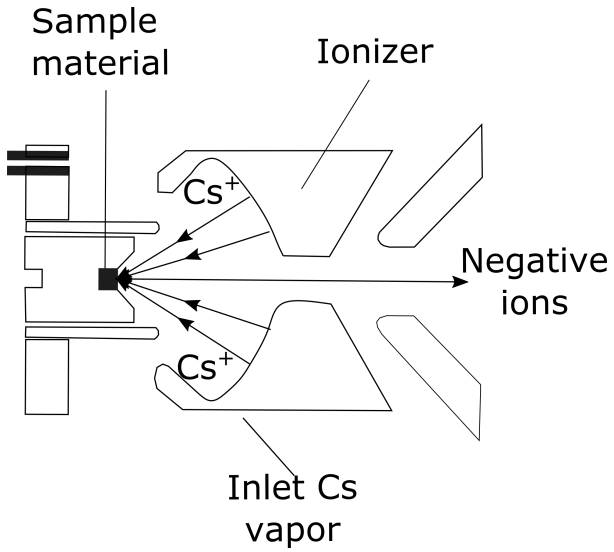


Figure 4.3: A schematic diagram of a typical Cs-sputtering ion source. A Cs reservoir is heated to produce a Cs vapor. Some of the Cs is ionized to Cs+ on a hot hemispherical tantalum surface. Cs+ ions are accelerated and focused on to the sample material.

4.6 High-energy Beam Selection

After exiting the accelerator, a variety of equipment choices is available for beam transport and analysis and for rejection of unwanted particles. The most common approach involves a magnetic analyzer to select a beam with the required value of ME/q^2 preceded or followed by an electrostatic analyzer to select E/q values or a velocity analyzer to select ions with specific E/M.

4.7 Ion Detection

The positive ions continue to the detector system where M and Z are inferred. Various detector designs have been constructed which include:

- Silicon detectors: These provide total energy measurements. They are adequate to separate species with the same M/q, but not isobars.
- Ionization chambers: These provide multiple measurements of the rate of energy loss. They may allow separation of isobars, for example ^{36}Cl and ^{36}S.

- In other cases, the AMS isotope and an unwanted isotope may be so close in mass that one isotope cannot be distinguished from others with an energy measurement in an ion chamber. This is the case for ^{236}U and the isotopes ^{235,238}U. However, their difference in mass leads to measurable differences in flight time over a distance of typically 1-2 m. A time of flight detection system has been developed to identify ^{236}U from ^{235,238}U.

In the next chapter I will describe the experimental developments and results using AMS on ultrapure Cu to detect ulta-low levels of Th and U.

Chapter 5

U and Th detection using AMS

5.1 Introduction

Although AMS has been demonstrated for the ultra-sensitive measurement of concentrations and isotope ratios for several actinides e.g. [108, 109, 110, 111, 112, 113, 114], this technique has only very rarely been used to detect ultra low concentrations of primordial actinides [78]. Natural U and Th are always present in the ion source, this could create a significant background for AMS measurements of these actinides in ultra low levels.

Typically the actinides measurements consist of the measurements of the ratio between a rare isotope e.g. ^{233}U, ^{236}U and the stable isotope e.g. ^{238}U. In our case the aim is to produce materials with ultra-low levels of ^{238}U and ^{232}Th and be able to quantify the trace amounts. the first step therefore was to establish a method to measure ^{238}U and ^{232}Th using AMS, for this we explored first the low energy mass spectrometer of the AMS setup at the Holifield Radioactive Ion Beam Facility (HRIBF) at ORNL . HRIBF was placed in shut down mode in 2012 and the 25 MV Tandem operated on its own since then intermittently for targeted experiments until March, 31st 2016, when it was shut down definitively. However the low energy mass spectrometer of the 25 MV Tandem AMS setup is still available for use, it consists of the Cs-sputtering ion source, 90 ° magnet and a faraday cup (Figure 5.1).

We first wanted to perform a mass scan of the ultrapure Cu, to investigate what other elements are present and to establish a method to extract U and Th from the solid ultrapure Cu sample. The mass scan revealed the formation of Cu clusters, the study of the clusters

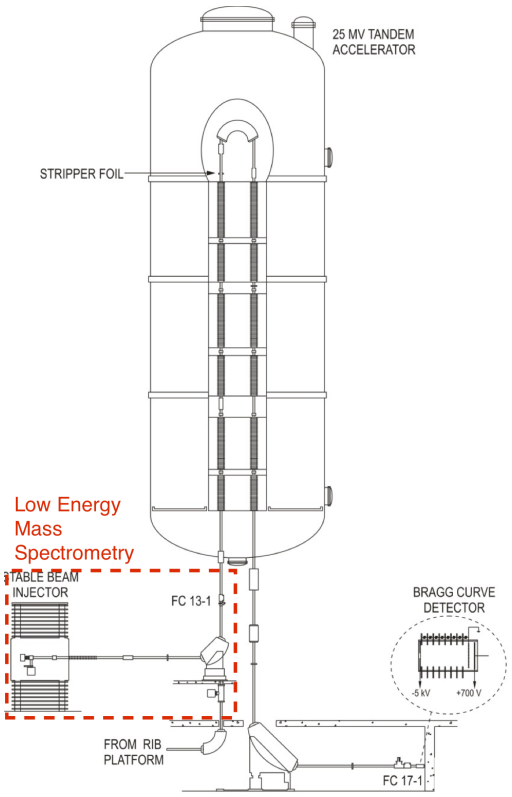


Figure 5.1: The low energy section of the 25 MV Tandem at ORNL consists of a single cathode Cs ion source, a 90° injection magnet and a faraday cup.

are explained in more detailed in Appedix A and in [115]. This study allowed us to establish a method to extract U and Th from the Cu sample. In AMS, Th and U are often extracted as negatively charged oxides. Sample handling and factor such as opening and closing the ion source can affect the yield of the negative oxides. Therefore we chose a compound of the element with the matrix material which is formed in the ion source. Th or U atoms and copper atoms can form a molecular bond when they are ionized. The resulting negative molecules are $Th^{63}Cu^-$ and $U^{63}Cu^-$, choosing the isotope ^{63}Cu because of its higher abundance.

As I mentioned before we could no longer use our 25 MV Tandem accelerator, this presented a challenge for our experiments, leading us to search for the use of other facilities. Only very few laboratories do trace AMS analysis such as [116, 117, 118, 119, 120, 121, 122, 123], but these facilities have a relatively small tandem accelerators (∼3 MV) and some of them do not perform measurements on actinides. One of the largest tandem accelerators

nowadays is the the 14 MV Pelletron accelerator model 14UD from the Heavy Ion Accelerator Facility (HIAF) at the Australian National University (ANU). We established a collaboration with the nuclear physics group led by Dr. Wallner. This group has very well established research AMS programs including measurements on actinides.

5.2 AMS at ANU

The ANU 14UD has on-going programs in nuclear structure, nuclear reactions, fusion, ion beam analysis, and AMS. The tandem operates up to 15.5 MV and services 7 beamlines. A switching magnet allows selection of the target beam line to be used. Two beam lines, "line 5" and "line 7", are dedicated to AMS, for this experiment we used the beamline 5. The (Figure 5.2) show a layout of the HIAF, showing the different beam lines for the 14UD pelletron tandem and the superconducting linear accelerator.

The basic elements of the AMS setup at ANU are shown in Figure 5.3, they consists of:

1. The Multi Cathode Source of Negative Ions by Caesium Sputtering (MC-SNICS, see Figure 4.3) attached to the top of the 14UD Tandem accelerator to produce negative ions. It should be noted that this setup is opposite as the one at ORNL, the ion source for ORNL is located on ground level and the ions are accelerated upwards, while in ANU the ion source is located at the top of the accelerator and the ions are accelerated downwards. The principles of the Cs-ion source is explained in previous Section 4, however specifically for this accelerator the cesium is evaporated in an oven and ionized by a tantalum surface ("ionizer") that is heated to about 1000 °C. As the cathode is at a potential of -5 kV relative to the ionizer, the Cs+ ions are accelerated towards the cathode. The Cs+ ions with an energy of about 5 keV sputter the target material, resulting in negative molecular or atomic ions. The cesium layer forming on the target material serves as the electron donor for negative ion formation. Negative ions leaving the target are accelerated by the cathode voltage (-5.0 kV), and to match to the entrance optics of the accelerator, the negative ions are pre-accelerated with a voltage of 100 kV.

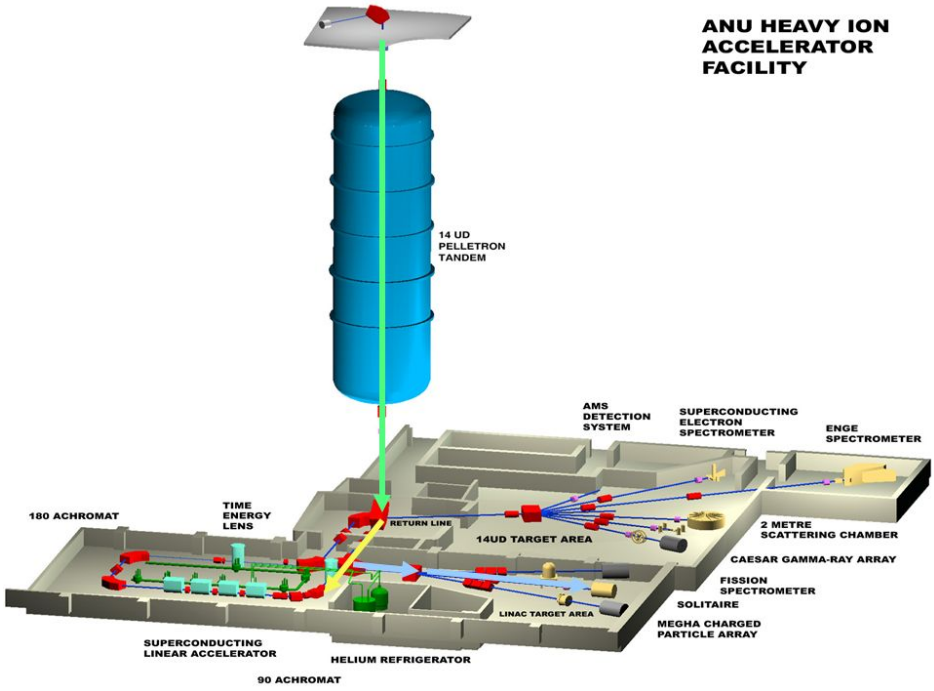


Figure 5.2: Heavy Ion Accelerator Facility (HIAF) layout. The pelletron tandem accelerator services 7 beamlines in the 14UD target area. For this work we use line 5 marked in the figure.

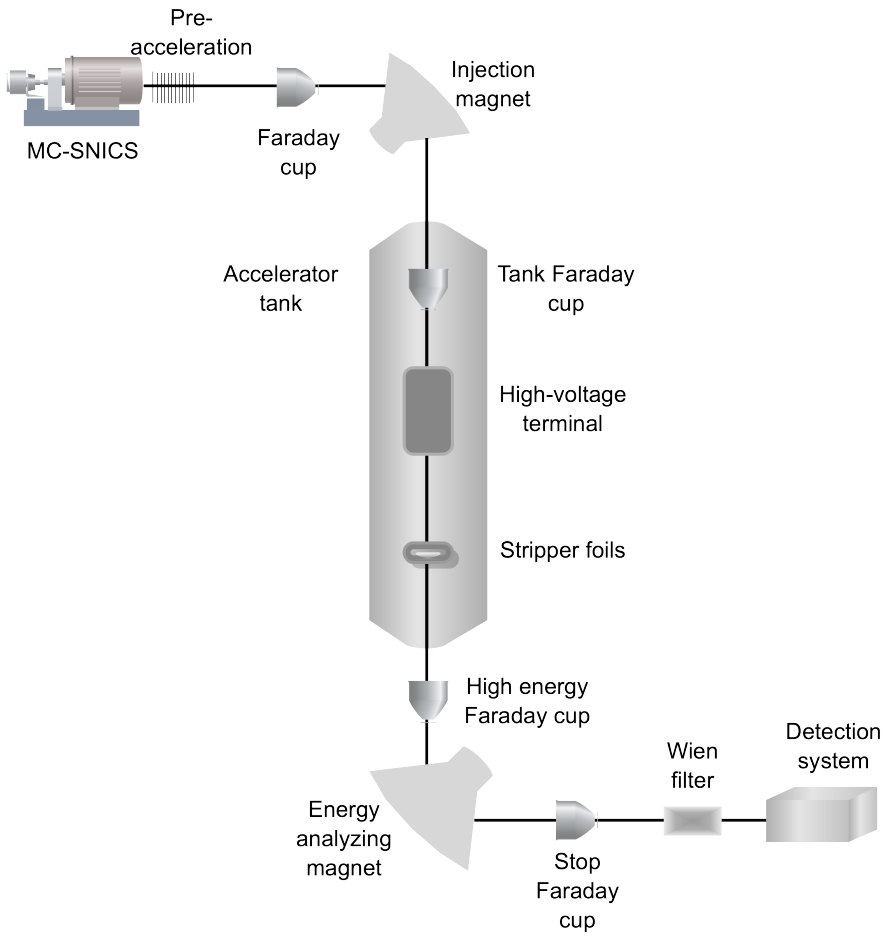


Figure 5.3: Schematic diagram of the 14UD Accelerator facility at the ANU. The negative ions are pre-accelerated at about 100kV towards the injection magnet where the isotope of interest is mass selected and accelerated towards the high voltage terminal, here the ions are stripped and molecules are dissociated. The now positive ions are mass selected by the analyzer magnet and then velocity filtered before arriving to the detector.

2. The 90° injection magnet then selects the desired ions by their mass and the singly-charged negative ions are accelerated to the positively charged high-voltage terminal at 4.176 MV.

3. The stripper is in charge of converting the negative to positive ions, and to dissociate molecular ions. Either a solid carbon foil or low-pressure gas may be used. The positive ions are accelerated away from the positive voltage on the terminal.

4. The analyzing magnet select the ions with the required ME/q^2.

5. The Wien Filter, a velocity filter selector is located after the analyzing magnet to remove any background. The ion with the given M/q value are then transmitted towards the detection system.

6. The time of flight detector consists of a start detector and a stop detector. At ANU, the start detector is a Chevron detector [124], which consist of two Microchannel Plate (MCP) attached to a 75% transmission copper grid and a 0.6 $\mu g/cm^2$ diamond-like carbon foil, for more information see [125]. The Stop detector is a 300 μm thick silicon surface barrier detector with diameter of 16 mm [126]. This detector produces a signal that indicate both the arrival of the particle and the energy deposit of that particle in the detector, a more detailed information about semiconductor silicon detectors can be found in [127]. The Figure 5.4 shows the setup for the TOF detection at ANU, the MCP is enlarged for a more detailed view.

5.3 Experimental Procedure

5.3.1 Sample Preparation

We used different Cu samples, shown in Table 5.1, with different purities for comparison and reference. The samples were formed to fit the target holder of the cathode wheel, see Figure 5.6. All the samples were solid, Figure 5.5.

Table 5.1: Cu samples with different purity.

Sample type	Description
Ultrapure electroformed Cu	Sample taken from the copper used for the MAJORANA experiment.
Kuprodur	Consist of Cu, 1.0%-1.6% Ni, 0.4%-0.7% Si [78].
Natural Cu	Industrial Cu, without special treatment. Provided by ANU.

In order to decrease background we used an aluminum cathode wheel, instead of the traditional copper wheel. After all the samples were placed in the source, we placed the wheel in the stable injector, see Figure 5.6, and we made a vacuum of the order of 10^{-7} torr.

5.4 Injection Beams

Initial tuning of the beam transport system is best done using a stable beam of nearby mass, Cu clusters were used in this work for this purpose, Table 5.2 has the different beams used. The settings of the inflection magnet, terminal voltage and Wien filter (all other parameters were held fixed) for the ^{232}Th and ^{238}U isotopes were initially determined by extrapolation from Cu clusters settings. The Cu clusters beam also allows estimation of the transmission from the ion source to detector. Transmission is defined as the ratio of the number of U^{+5} or Th^{+5} ions reaching the Faraday cup just before the detector to the number of $^{232}Th^{63}Cu$ or $^{238}U^{63}Cu$ ions injected into the accelerator following initial mass analysis by the inflection magnet.

The beam was more stable when was extracted as Cu compound. The normalized counts for ultrapure Cu sample are shown in Figure 5.7. The normalization is calculated by dividing the counts by the measuring time and the Cu cluster ion current after the inflection magnet used for scaling.

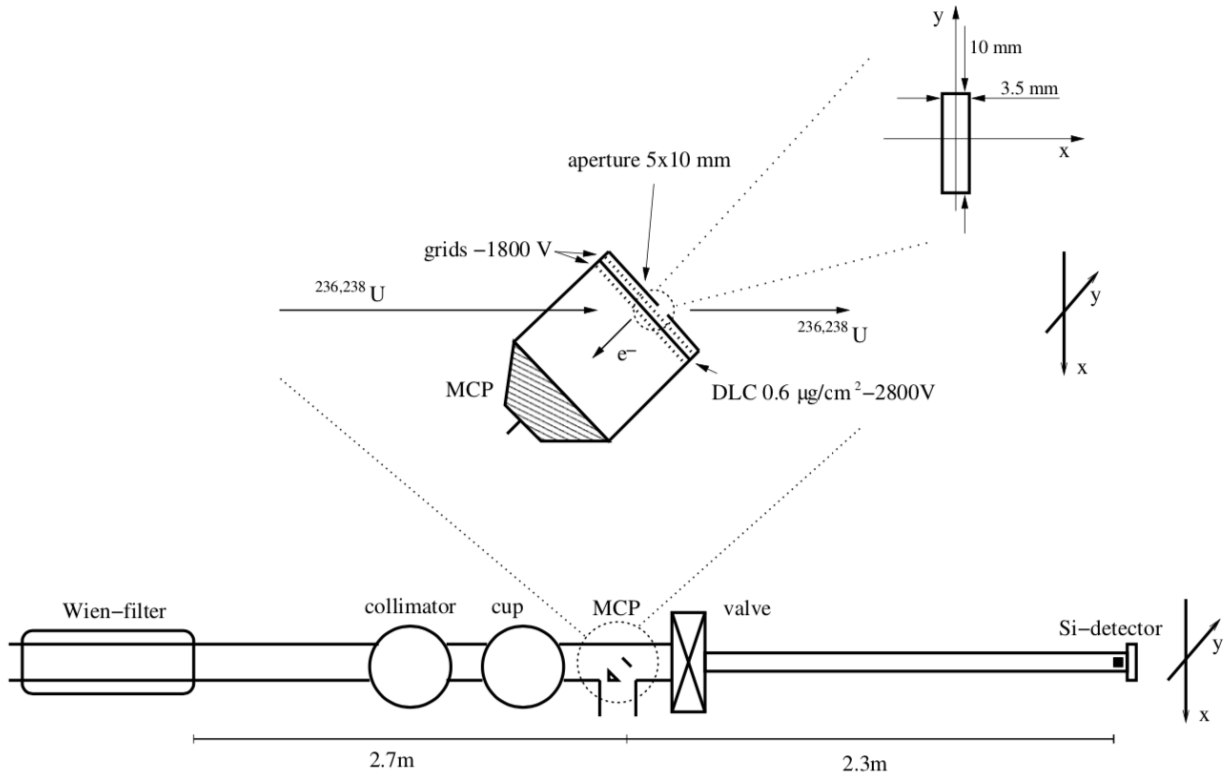


Figure 5.4: Schematic diagram of the time-of-flight detector system. The ions passing the Wien filter pass the MCP, the start detector which is enlarged in this figure for a more detailed view. The stop detector is a silicon detector 2.3 m away from the MCP [6]

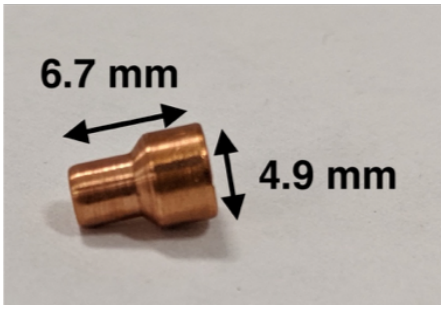


Figure 5.5: Sample size and shape to fit the target holder of the cathode wheel.

Table 5.2: Input beam molecules and tuning beam molecules.

Input beam	Scaling/tuning beam
$^{238}U^{63}Cu$	$^{63}Cu_4{}^{65}Cu$
$^{232}Th^{63}Cu$	$^{63}Cu_4{}^{65}Cu$
^{238}U	$^{63}Cu_3{}^{65}Cu$
^{233}Th	$^{63}Cu_3{}^{65}Cu$
$^{238}U^{16}O$	$^{63}Cu_3{}^{65}Cu$

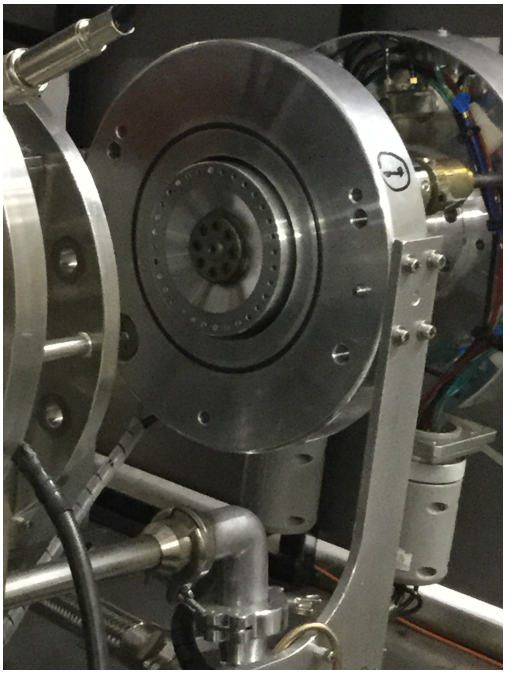


Figure 5.6: Aluminum cathode wheel in the MC-SNICS used for the Cu measurements. Commonly for AMS measurements a copper wheel is used, however for our measurements the Cu wheel was not chosen as it can potentially create strong backgrounds.

5.5 U and Th in Cu Samples and Outlook

We have successfully established a method to detect U and Th in ultra-pure electroformed Cu. Events of Th and U were observed in all Cu samples, Figure 5.8. Further quantitative work would require the establishment of a reliable reference sample with a well defined concentration of U and Th. It is recommended to measure the standard sample with another technique such as gamma-ray spectrometry. There are three laboratories in the US that have the capabilities for an underground gamma-ray spectrometry:

- The low-background counting facility located underground at the Waste Isolation Pilot Plant (WIPP) near Carlsbad, NM operated by Los Alamos National Laboratory.
- The Kimballton Underground Research Facility (KURF) is located at Lhoist North America's Kimballton mine in Ripple mead, VA and is operated by the Virginia Polytechnic Institute and State University.
- The low background facility (LBF) at Oroville, operated by Lawrence Berkeley National Laboratory (LBNL) which now has moved to the Sanford Underground Research Facility (SURF).

Once the value of the standard is determined the concentration c in the samples can be obtained using equation 5.1, in which t is the measuring time, I is the current of the copper cluster $^{63}Cu_4^{65}Cu$ at the cup in front of the accelerator and n is the number of events in the detector of the sample, and c_s; t_s; I_s and n_s are the values for the standard.

$$c = c_s \cdot \frac{t_s \cdot I_s}{n_s} \cdot \frac{n}{t \cdot I} \tag{5.1}$$

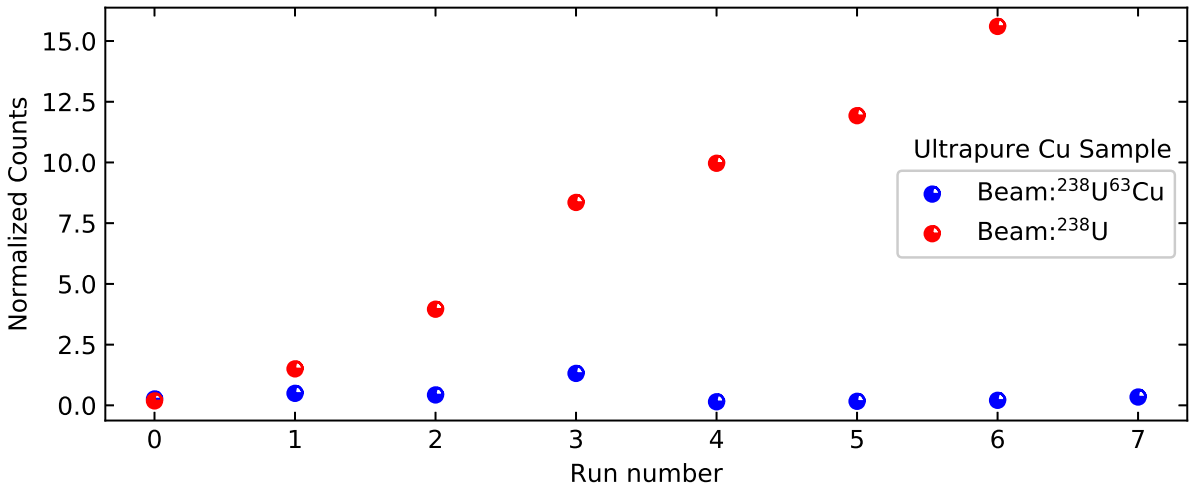


Figure 5.7: Beam intensity comparison for ultrapure Cu sample. The beam extracted from $^{238}U^{63}Cu$ was more stable than the beam extracted directly as U.

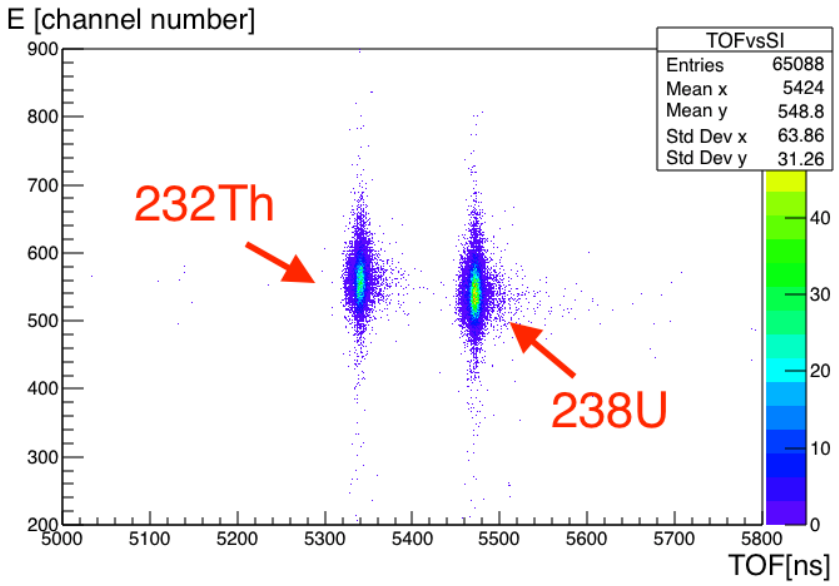


Figure 5.8: Overlay of $^{238}U^{+5}$ and $^{232}Th^{+5}$ 2D histogram of energy vs time of flight showing the events detected in ultrapure Cu sample.

Chapter 6

Resonant Ionization Mass Spectrometry

6.1 Introduction

Resonance Ionization Mass Spectroscopy (RIMS) has been proposed as an efficient spectroscopic technique well suited for trace analysis and related studies by various authors [128, 129, 93]. In this technique resonant laser light at different wavelengths are used to stepwise resonantly excite the atoms to higher energy levels and finally ionize them in the last step. The ions are mass selected and then counted quantitatively.

RIMS was first proposed around the beginning of the 1980's and from that time has been developed and adopted by an increasingly larger group of scientists [130, 131, 132, 129, 133] . It has been applied in fields such as chemistry, physics, geology, and biology. The main advantages of RIMS are:

- High efficiency of excitation and detection: Nowadays the availability of reliable and powerful laser systems, ranging from the ultra-violet to the infrared spectral region, ensures the efficient excitation of all steps of the resonant ionization spectroscopy (RIS) scheme. Hence, the ionization process can be effectively realized. Afterwards the ions and/or electrons are detected. In that way high detection efficiency is obtained, since the detection of charged particles is much more efficient than e.g. that of photons.

Also particle detection eliminates the problem of scattered excitation photons,which is a problem in purely optical methods.

- High elemental and isotopic selectivity: In each individual optical excitation step the resonance condition must be fulfilled. This provides complete elemental selectivity and, in favorable cases, isotopic discrimination may also be achieved. The problem of interference, which is of major concerning conventional optical trace analysis, can be avoided in RIS. Furthermore, isobaric interference as observed in mass spectrometry is strongly reduced.

- Mass selection: The selectivity of RIS can be further enhanced by a mass selective step before detection of the resonance ions. This combination of RIS with mass spectrometry is called RIMS (Resonance Ionization Mass Spectrometry).

- Low background: In RIS and RIMS the background can be kept low, due to the use of suitable particle detectors and , in case of RIMS, due to the background reduction arising from the mass selective step.

RIMS instrumentation includes a source of atoms (molecules), tunable laser(s), and a mass analyzer or detector [134]. Resonance ionization requires free atoms. Although a variety of atomization approaches have been employed [133, 135, 136], efforts in our laboratory have focused on the use of the surface ionization with a hot cavity ion source, this together with the lasers form what is called Resonant Ionization Laser Ion Source (RILIS), which is discussed in the next Section 6.2.

6.2 Resonance Ionization Laser Ion Source

Resonance ionization uses efficient stepwise excitation through strong atomic transitions and successive ionization, induced as final excitation step. Figure 6.1 illustrates the basic principle of a resonance ionization scheme with 2-step (left) or 3-step excitation (right). The frequency of the lasers used is precisely tuned, to resonantly excite strong transitions of the atoms of interest. The usual starting point is the ground state of neutral atoms.

Alternatively, energetically low-lying states with reasonable thermal population can be used as well. Multi-step resonance ionization specifically addresses a set of individual atomic levels, which are unique for each element in the periodic table. Correspondingly, the excitation and ionization are highly element selective. Resonance ionization mass spectrometry (RIMS) combines the resonant ionization process with a subsequent mass selection process. This can be achieved by using, for example, a magnetic mass separator or a quadrupole mass filter.

RILIS is based upon this principle of stepwise photo-ionization. This process was demonstrated by Letokhov and colleagues in 1972 [128]. The theory of resonance ionization is discussed in detail, with emphasis on the technique of resonance ionization spectroscopy, in Letokhov's book Laser Photoionization Spectroscopy [131].

The RILIS at the Oak Ridge National Laboratory (ORNL) was initially developed for the production of isotopically pure radioactive ion beams at the Holifield Radioactive Ion Beam Facility (HRIBF). Although HRIBF has not operated as a National User Facility since April 2012, some of its infrastructure and expertise was maintained including RILIS [137] and the Injector for Radioactive Ion Species 2 (IRIS2) [138, 139].

The RILIS consists of a hot-cavity ion source and three all-solid-state, pulsed Ti:Sapphire lasers to provide up to three- step, three-photon ionizations. A cross sectional side view of the HCSIS assembly is displayed in Fig. 6.2 which shows the principal components: the hot-cavity ionizer, the sample tube, the graphite housing, and the extraction-electrode of the ion source.

The hot-cavity ion source is mounted on the platform of the IRIS2, while the Ti:Sapphire lasers are installed in a dedicated laser room adjacent to the IRIS2 target and ion source room. The laser beams are collimated and combined in the laser room, transported into the IRIS2 room, and then focused into the hot-cavity ion source through the viewport of the mass analysis magnet, as illustrated in Figure 6.3. The total laser beam path is about 18 meters.

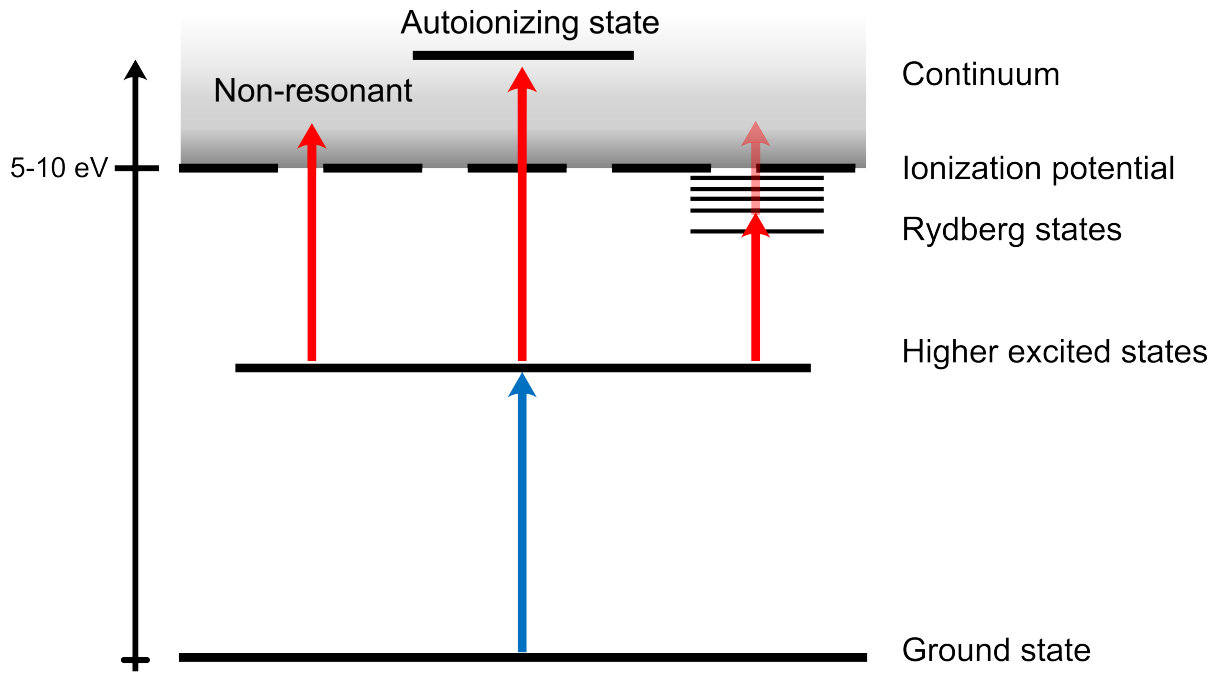


Figure 6.1: Excitation schemes for resonance ionization, two-step resonant excitation is taken as an example. The final ionization can be achieved by three different processes: non resonant, autoionizing and Rydberg states.

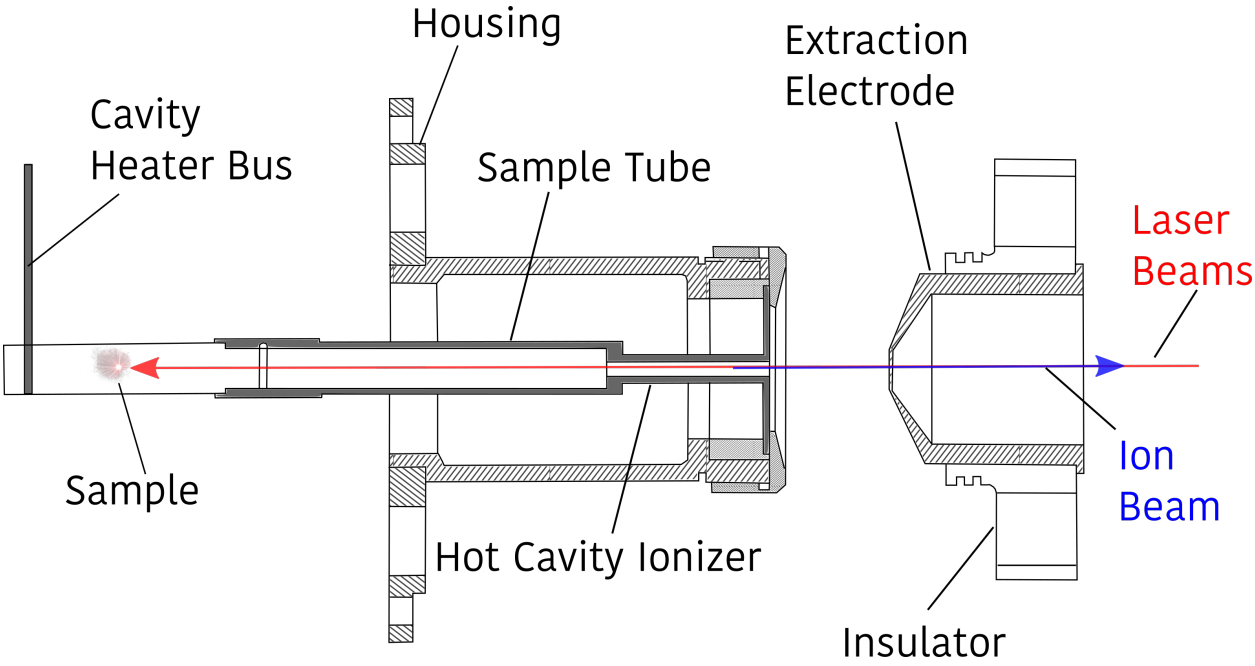


Figure 6.2: Cross sectional side view of the hot-cavity ion source assembly showing the main components of the source and the direction of the laser and ion beams.

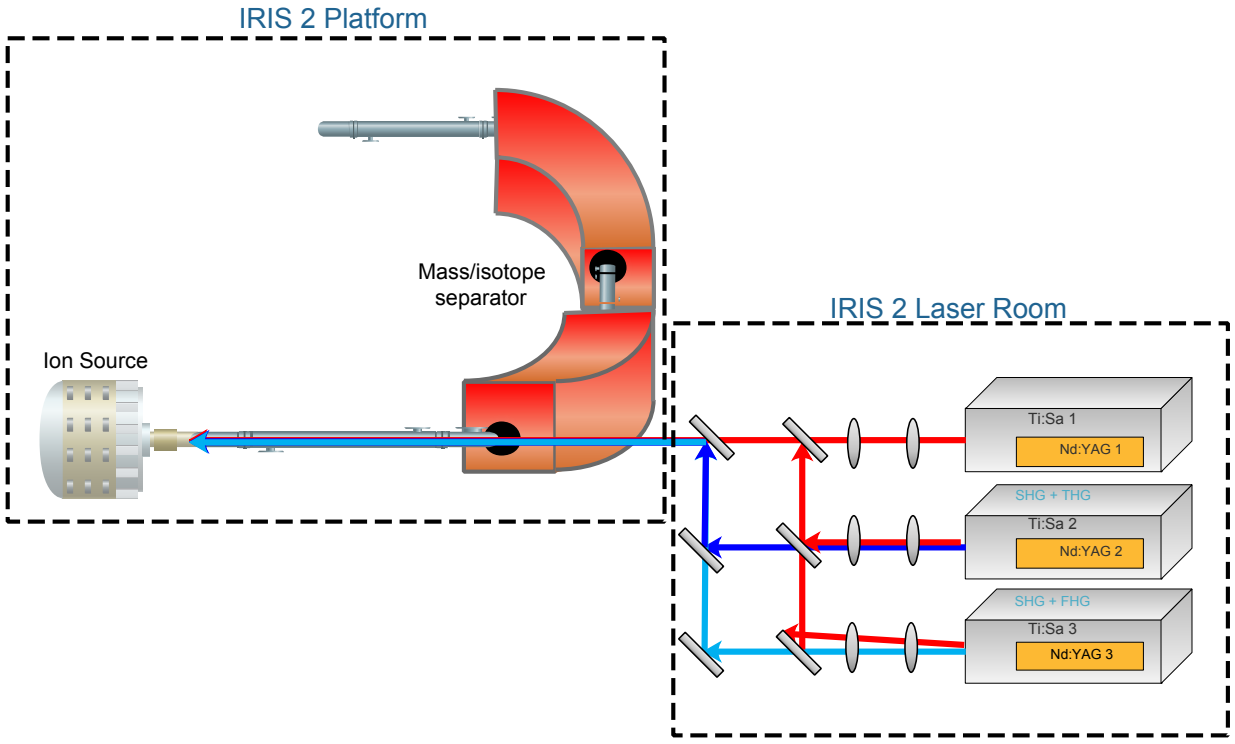


Figure 6.3: Representation of the laser beam path from the laser room to the hot cavity ion source located in IRIS2.

6.3 Hot Cavity Surface Ionization source

The hot-cavity ionizer is a cylindrical cavity of 3-mm inner diameter (ID), 30-mm long and 1-mm wall thickness. The ionizer is connected to a closed-end Ta tube of 8.5-mm inner diameter and about 100 mm long, in which samples are placed.The ionizer and the sample tube are heated resistively by passing a current through the tubular structure and can be heated to temperatures exceeding 3000 K in the ionizer. The sample materials in the sample tube are heated along with the sample tube and the ionizer. The volatile species effuse from the sample tube into the ionizer where they are ionized by surface ionization. The ions are extracted by the conical electrode.

Atoms or molecules impinging on a hot metal surface may be emitted as atoms or ions, depending on the work function, Φ, of the metal surface and the first ionization potential, IP, of the atom or molecule [140, 136]. The degree of ionization, a, is given by the Saha-Langmuir equation:

$$\alpha = \frac{n_i}{n_0} = \frac{g_i}{g_0} exp(\frac{\Phi - IP}{kT}) \tag{6.1}$$

where n_i and n_0 are the concentrations of the ions and neutrals leaving the surface and g_i and g_0 are the statistical weights of the ionic and atomic states, respectively, k is the Boltzmann's constant, and T is the temperature of the surface. The surface ionization efficiency, b, is defined as,

$$\beta = \frac{n_i}{n_i + n_0} = \frac{\alpha}{1 + \alpha} \tag{6.2}$$

From Eqs. (6.1) and (6.2) it is evident that high ionization efficiencies can be obtained for high work-function materials and low ionization-potential species such as the alkali metals [141]. The degree of ionization predicted by Eq. (6.1) assumes that the ions are extracted as soon as they are formed. The neutral species undergo significantly higher number of wall collisions with the hot-cavity configuration and thus have a much larger probability to be ionized. A thermal plasma, consisting of surface ionized positive ions and thermionic electrons emitted from the hot walls, could form inside the hot-cavity. The plasma may

reach near thermodynamic equilibrium with the cavity wall. Due to the high thermionic electron density at the wall, a negative plasma sheath potential with respect to the wall is created so that the positive ions can be confined to the plasma, preventing ion-wall collisions and thus ion losses.

6.4 Laser System Description

The laser system includes three pulsed Ti:Sapphire (Ti:Sa) lasers, Figure 6.4, operating at 10 kHz pulse repetition rate, all manufactured by Photonics Industries International, Inc. in Ronkonkoma, New York. Each Ti:Sapphire laser is individually pumped by a Q-switched Nd: YAG laser at 532 nm with an average output power of 19 W at 10 kHz pulse repetition rate. The Ti:Sa output pulses are typically 25–30 ns wide. The advantage of using individual pump lasers is that the three Ti:Sapphire laser outputs can be easily synchronized in time by synchronizing the pump lasers with external triggers. Consequently, higher Ti:Sapphire laser output power can be obtained. All three Ti:Sapphire lasers use a diffraction grating for wavelength selection so that they are continuously tunable over the available spectral range.

The Ti:Sa lasers are typically tunable between 720 nm and 960 nm, with about 2.5 W peak power near 810 nm, see Figure 6.5. At the fundamental frequency, the spectral range of tunable laser systems is not sufficient to enable their application for efficient resonant ionization of a wide range of elements . In fact, for many elements, suitable first excited states lie at an energy that is far into the UV region, corresponding to a wavelength less than half of that achievable at the short-wavelength end of the tuning range of a dye-laser system. These transitions are, however, accessible if the second or third harmonic of the fundamental emission frequency is generated. Two of the three Ti:Sa lasers are combined with units for second-harmonic generation (SHG), third-harmonic generation (THG), and fourth-harmonic generation (FHG). The Ti:Sa lasers are compact. Each Ti:Sa laser and its pump laser are mounted together as one unit. The Ti:Sa laser has a dimension of 22”×7.5”×3.75 ” (Length×Width×Height). A more detailed description of the laser system can be found in [7, 142].

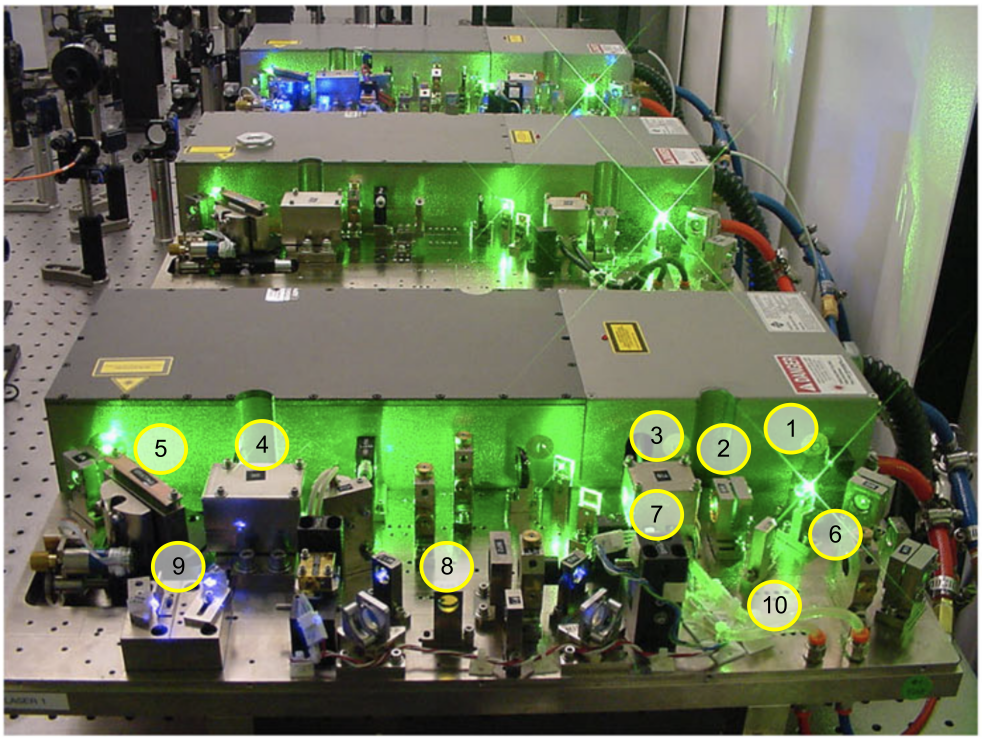


Figure 6.4: The three Ti:Sa lasers at ORNL. The main components are labeled: ① Photonics Nd:YAG pump laser and pumping beam optics; ② Lens; ③ Ti:Sapphire crystal; ④ Pockel cells; ⑤ Grating; ⑥ Lens; ⑦ Second-harmonic generation (SHG) crystal; ⑧ Beam optics for SHG; ⑨ Laser beam exit; ⑩ Chiller tubes.

6.5 Experimental Setup at ORNL

The RIMS equipment used in this experiment at the Oak Ridge National Laboratory (ORNL) was initially developed for the production of isotopically pure radioactive ion beams at the Holifield Radioactive Ion Beam Facility (HRIBF) [143]. Although HRIBF has not operated as a National User Facility since April 2012, some of its infrastructure has been maintained including the resonant ionization laser ion source (RILIS), three compact tunable Ti:sapphire lasers and the Injector for Radioactive Ion Species 2 (IRIS2) used as a mass spectrometer. Figure 6.6 is a schematic diagram of the overall experimental setup. The positive ions generated by laser radiation are extracted from the hot cavity and accelerated to energies of 15-40 keV. Faraday Cup 1 measures the total beam current from the ion source, Faraday Cup 2 measures the beam current after a 25-degree dipole magnet that provides initial mass

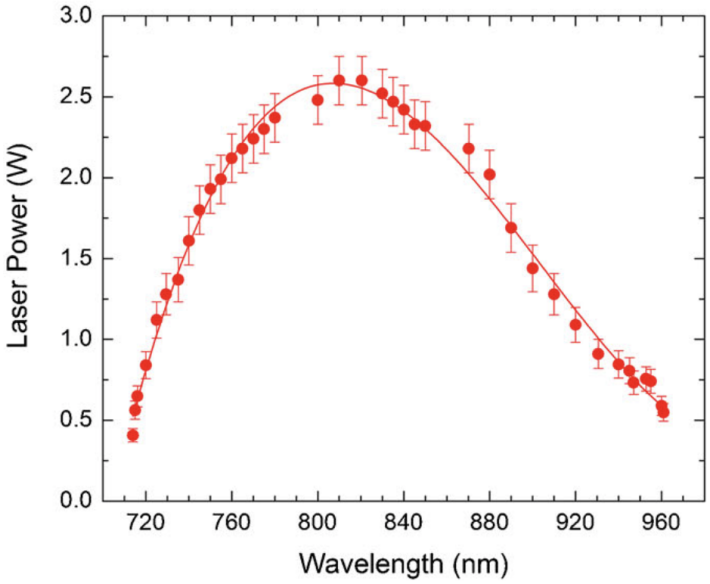


Figure 6.5: Typical tuning curve of the Ti:Sa lasers [7]. The peak on the curve is at 2.5 W peak near 810 nm.

selection with low resolution, and Faraday Cup 3 measures the ion current after a high-resolution, 120-degree dipole magnet mass separator. Faraday Cup 4 measures the final ion current that is recorded together with the wavelength.

The fundamental wavelengths of the three Ti:Sapphire lasers were monitored simultaneously using a calibrated wavelength meter (HighFinesse WS6-600) equipped with a 4-channel opto-mechanical switcher. The tuning of the ion beam was performed using the optics of IRIS2 and by adjusting the lasers. The adjustment of the lasers was done through New Focus 8752 picometer controller for very fine tuning of the laser beam optics. I created a GUI interface to communicate remotely to the picomoter drivers, a screen shot of the program is shown in Figure 6.7. In the next chapters I will describe our level schemes search and the measurements performed in Pu for efficiency and sensitivity studies using this experimental setup.

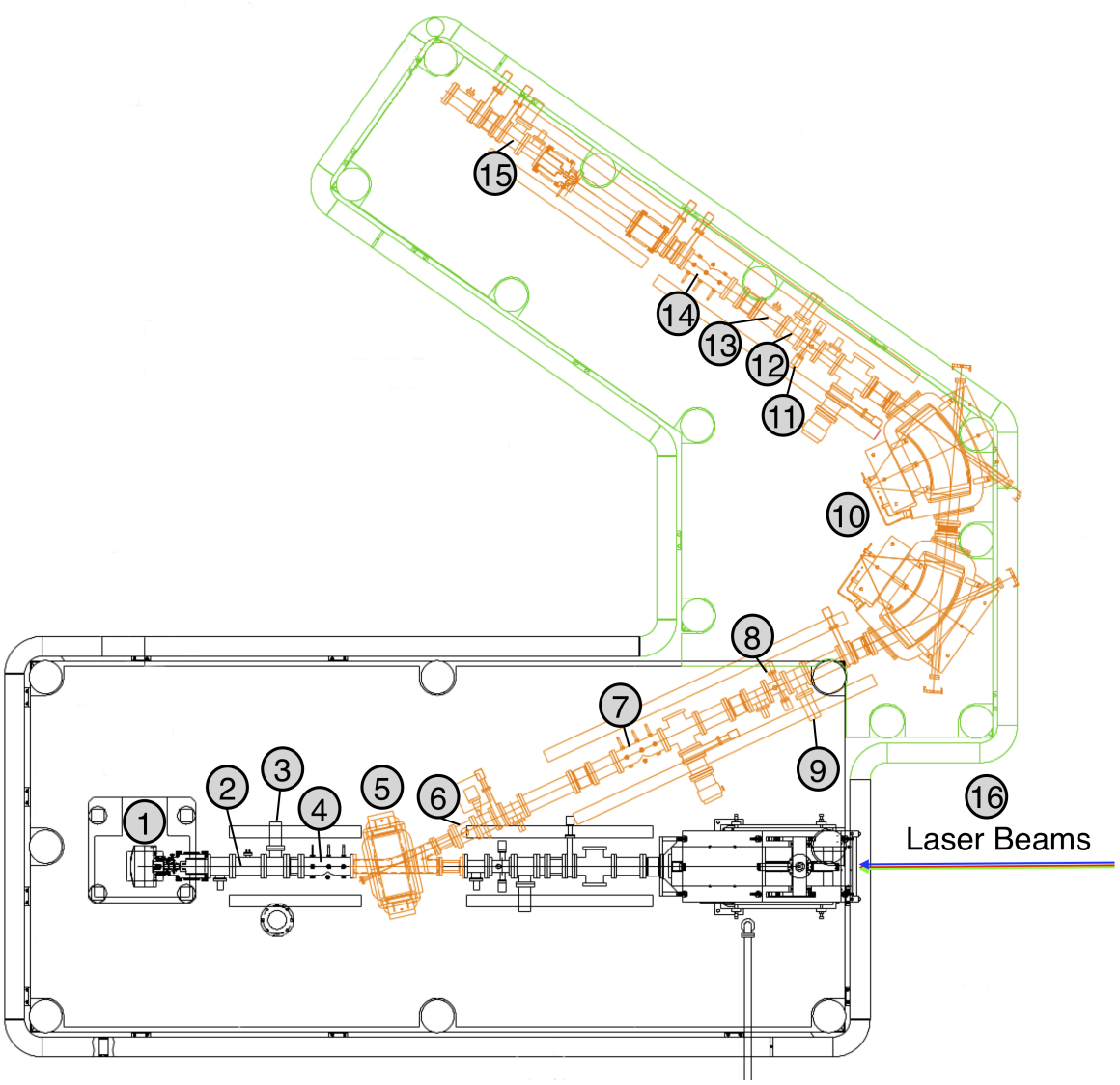


Figure 6.6: RIMS setup at the Oak Ridge National Laboratory. Individual elements of the system are labeled by numbers: (1) Hot cavity ion source, (2) Electrostatic Steering (ES) 1, (3) Faraday cup (FC) 1, (4) Electrostatic quadrupole (EQ) 1, (5) Low resolution magnet, (6) ES 2, (7) EQ 2, (8) Slits, (9) FC 2, (10) High resolution magnet ($m/\Delta m = 1000$), (11) Slits, (12) FC 3, (13) ES 3, (14) EQ 3, (15) FC 4 (16) Laser beams entering the beamline through a vacuum window.

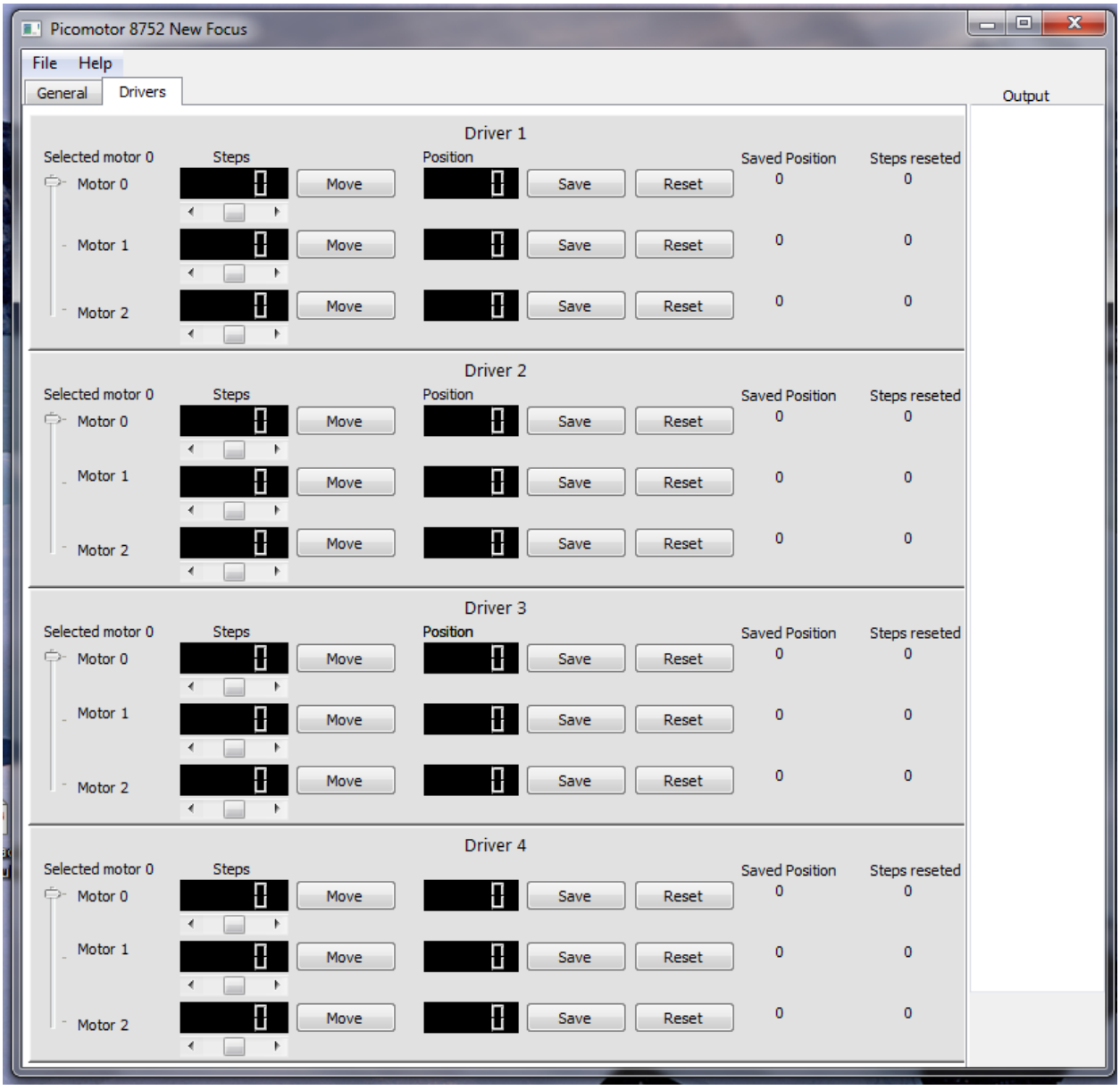


Figure 6.7: In order to perform fine tuning of the lasers I created this GUI interface to operate the New Focus 8752 picometer drivers remotely. Each picometer driver can control three motors for x, y and z movement. This interface allowed the movement in different step sizes and saved the current position for each motor for each driver. It also allowed us to go back to the saved position with the reset button. The output window showed the errors caused by the user.

Chapter 7

Plutonium Sample

7.1 Introduction

All of the actinide elements are radioactive, and, except for thorium and uranium, special containment and shielded facilities are mandatory for safe handling of these substances. Gloved boxes are required and personal protective equipment (PPE). Even when radiation can easily be shielded, as is the case with alpha-particle emitters, containment to prevent inhalation is still essential because of the toxicity of the transuranium elements. Inhaled transuranium isotopes may be deposited in the lungs and ingested isotopes may be absorbed to the bone, where the intense alpha radioactivity over a period of time can give rise to cancer.

The amount of PPE is determined by the strength of the radioactive source. Our sample consisted of 1 mg of plutonium-242 spike, dry nitrate from the New Brunswick Laboratory (NBL) with a radioactivity of 30 μCi. The sample came in layers of packaging starting with an outside container consisted of a sealed 5 steel gallon drum, a sealed plastic bag, a sealed can and a plastic wrapping around the Teflon bottle (shown in Figures 7.1a, 7.1b, 7.1c and 7.1d). The packaging was inspected with swaps performed by the physics division Radiation Control Technician, all the swaps were free of contamination.

The Teflon bottle is designed to prepare a solution of the concentration desired on a weight basis avoiding transferring of the material. We prepared the solution to have 100

parts per million (ppm). For 1 mg of ^{242}Pu we needed 10 ml of the solvent in order to have a concentration of 100 ppm.

7.2 ^{242}Pu Sample Dilution

The radioactivity of the 1 mg sample of ^{242}Pu is 1.1x10^{6} Bq (30 μCi) as of January 1, 1987. ^{242}Pu has a half-life of 373,300 years, thus the change of its radioactivity as of today is negligible. It is important to know the radioactivity because the Physics Division has technical requirements for the conduct of work depending on how hot the sample is; 30 μCi is considered highly radioactive to ORNL standards and therefore it was required the highest training on radiation, space work permits, work plan, special requirements for handling and protective personal equipment (PPE) to handle the ^{242}Pu sample. The Physics Division has a hot sample laboratory, shown in Figure 7.2, that we used to store and prepare the ^{242}Pu samples. The radiological work permits were made for this laboratory and the platform IRIS2 (mentioned in Chapter 6).

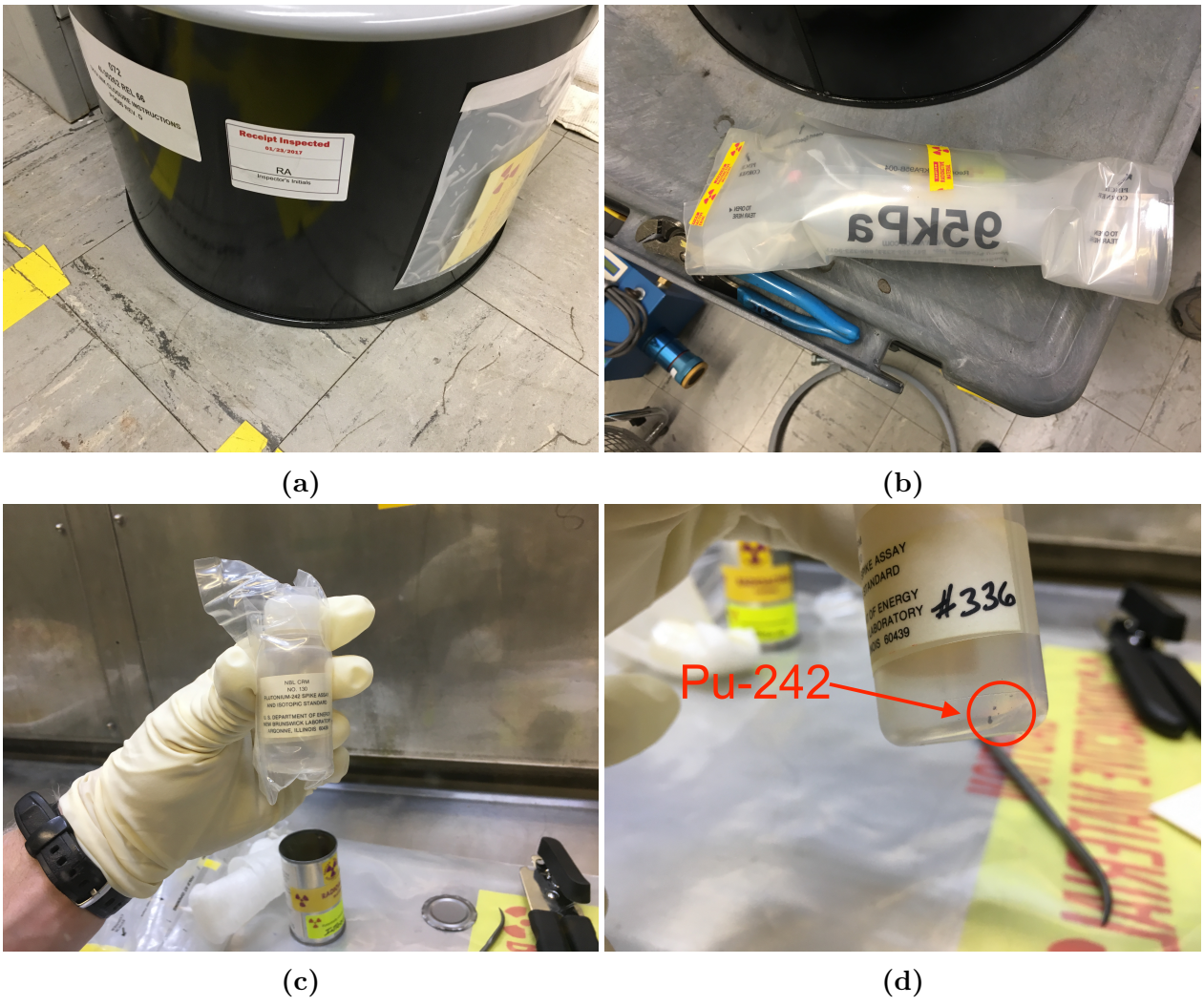
We adopted the procedure to dilute the sample from the certificate of analysis that came with the sample. In order to know our final solution concentration we used the equation 7.1, which depends on the weight of the bottle before and after the solution, for this reason we used a precision scale when we were preparing the sample. In order to ease the dilution we heated the solution with a hotplate and we controlled the temperature using a gun thermometer to avoid direct contact with the radioactive solution.

$$^{242}Pu\ \mu moles/g = \frac{(Certified\ content\ of\ ^{242}Pu,\ \mu moles)}{(wt.\ of\ bottle\ and\ solution[g]) - (tare\ of\ bottle,\ [g] - 0.0020)} \quad (7.1)$$

in which 0.0020 grams is the nominal weight of evaporated plutonium nitrate residue.

The following steps summarized our procedure for dilution to obtain a concentration of 100 ppm:

- We wiped the Teflon bottle with a damp chamois cloth to dissipate any static charge which may cause expulsion of the material upon opening.



(a) **(b)**

(c) **(d)**

Figure 7.1: Layers of packaging for the 1 mg of ^{242}Pu. The inspection was carried out by the Physics Division radiation control technician (a) 5 gallon drum shipping package, (b) Exterior packaging around the Teflon bottle (c) The 30 ml Teflon bottle, (d) 1 mg of ^{242}Pu



Figure 7.2: Hot laboratory at the physics division for the preparation of the Pu sample. PPE consisted on body and feet coverall, 2 pair of gloves and glasses. From left to right: Scotty Matthews (RCT), Dr. Galindo-Uribarri and Elisa Romero.

Table 7.1: Weight of the bottle before and after dilution.

Description	Weight (g)	Average (g)	Error (g)
Bottle weight with cap	19.6658 19.6633 19.6626 19.6610	19.6632	0.0006
Bottle weight with cap plus 1ml 8 M HNO3	20.8845 20.8864 20.8870 20.8881 20.8869 20.8870	20.8867	0.0006
Bottle weight with cap and 10 ml of total solution	29.7685 29.7680 29.7685 29.7684 29.7687	29.7684	0.0006

- We weighed the bottle then unscrewed the cap, add a 1 ml of 8M HNO_3 and carefully warm the bottle to insure total dissolution. We were very careful to no heat the bottle above 150°C because bottle deformation could have occurred.

- We replaced and tightened the cap, then we let the bottle to cool to ambient temperature. After approximately 15 min, we loosened the cap to equalize air pressure, we re-tightened, wiped the bottle with a chamois damp cloth, and weighed again.

- We shaked vigorously to homogenize the contents and this is our original dilution that we used later on to create more samples with different concentrations.

Table 7.1 shows the values of weights of the bottle at different stages of the procedure. These values are important to know to calculate the content of atoms in our samples since from this solution we prepared the samples needed for efficiency and sensitivity measurements.

7.3 Sample Drying Process for RILIS

Once we prepared the liquid solution of ^{242}Pu, the next step was to create the samples needed for each experiment by drying the solution with the desired amount in Zr foil. Every stage of the experiment required different concentrations and amount of ^{242}Pu sample. For example, for the level schemes searches we required the largest amount of material since we performed comprehensive scans for the second and third step and we wanted to run without the need of changing the sample. The campaign to search for the three step level schemes lasted around 2 months with 40 μg of ^{242}Pu.

For the efficiency measurements we had to exhaust all the sample in one run to calculate the ratio of the amount of atoms measured over the total neutral atoms of the sample. In this case, having a smaller sample was more convenient to exhaust the sample in a short period of time. For the efficiency measurements we ran continuously for 24 hrs with 4 μg of ^{242}Pu. Finally for the sensitivity measurements we tested our limit of detection by testing smaller and smaller samples. The values of the samples sizes and dilutions are shown in Table 7.2.

The drying process of the samples was also made in the hot lab using all the safety procedures to handle highly radioactive sources even when we used a very small amount of material. The following procedure to dry the sample was the same for any sample size.

In order to have a precise volume measurement of ^{242}Pu solution to make the samples, we used an air displacement micropipette. This type of pipettes deliver a measured volume of liquid and are capable of being very precise and accurate. However, since they rely on air displacement, they are subject to inaccuracies caused by the changing environment, particularly temperature and user technique. For these reasons users must be trained to exercise correct and consistent technique.

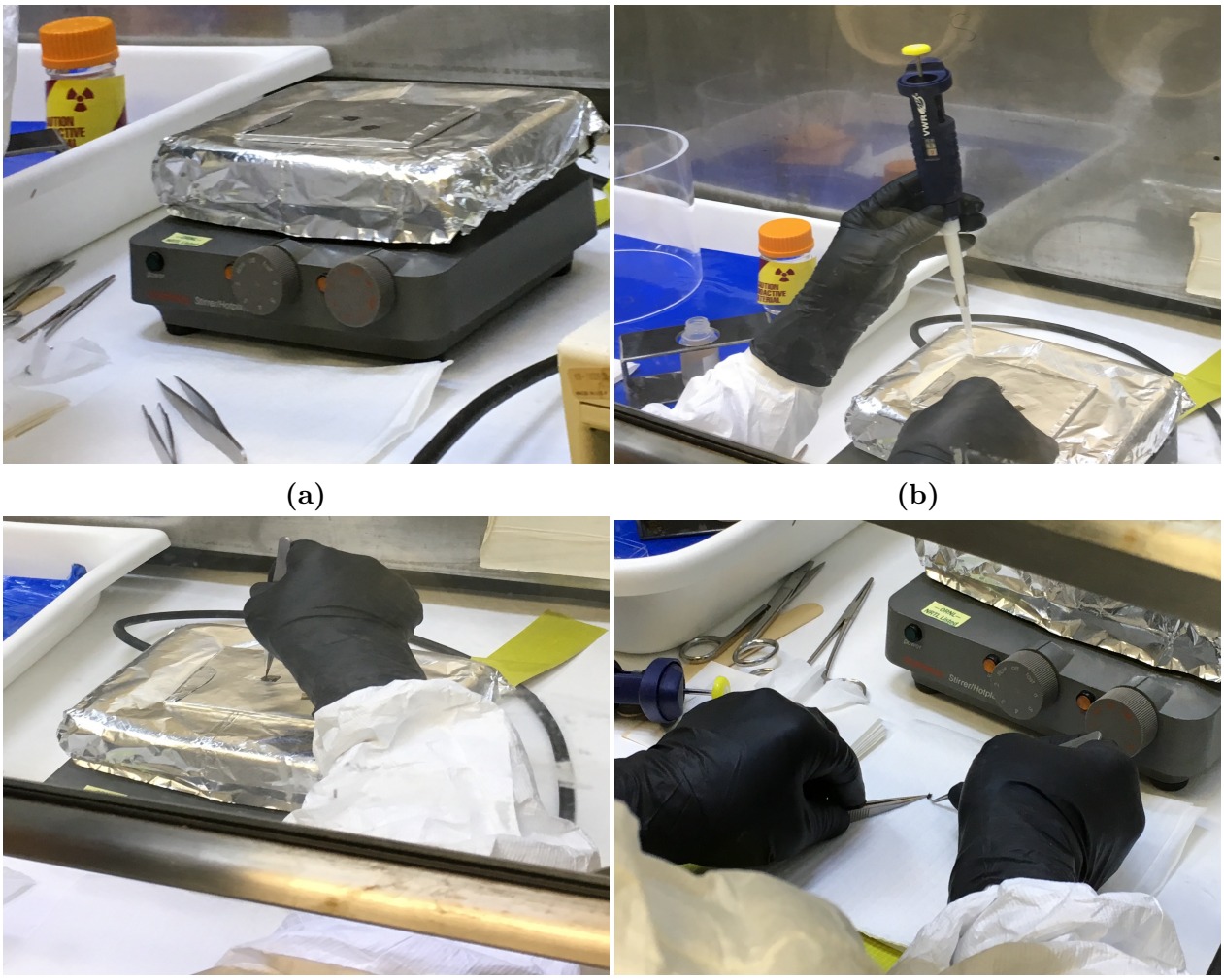
We used Zr foil of about 4 mm $\times$ 4 mm $\times$ 0.025 mm and we placed it on a hot plate. We wait a couple of minutes for the plate to heat up the foil, and then we took the volume of the sample with the pipette from the solution and we deposit it drop by drop in the foil. This would ensure the sample will dry completely and will not spill out of the foil. Once we finish drying the sample, we folded the foil in about 1 mm $\times$ 1 mm $\times$ 1 mm size, and this

was the final step ready to be placed in the sample tube of the ion source. Figures 7.3a-7.3d show the main steps for drying the sample.

Once we have the dry sample folded in the Zr foil, we transported it in a safe container to the IRIS2 platform where RILIS is located. With the presence of a radiation control technician, we placed it in the sample tube of the RILIS ion source. We used different concentration for each stage of our measurements which I will describe in the following chapters.

Table 7.2: Different sample dilutions and sizes for different stages in the experiment.

Name	Experiment	Concentration (ppm)	Concentration (weight per volume)	Dilution	Dry sample weight
Original	Three- step level schemes searches	100	$\frac{1\mu g}{10\mu L}$	- 1mg of ^{242}Pu - 10 ml of solvent	40 µg
	Efficiency measurement	100	$\frac{1\mu g}{10\mu L}$	- 1mg of ^{242}Pu - 10 ml of solvent	4 µg
1	Sensitivity measurements	1	$\frac{1ng}{10\mu L}$	- 10 µL of original sample - 1 ml water	10 ng
2	Sensitivity measurements	0.01	$\frac{10pg}{10\mu L}$	- 1 µL of sample #1 - 1 ml water	100 pg
3	Sensitivity measurements	0.001	$\frac{1pg}{10\mu L}$	- 1 µL of sample #1 - 1 ml water	1 pg
4	Sensitivity measurements	10^{-5}	$\frac{1fg}{10\mu L}$	- 1 µL of sample #2 - 1 ml water	10 and 100 fg



(a) **(b)**

(c) **(d)**

Figure 7.3: Summarized steps of drying the ^{242}Pu sample in Zr foil. (a) Placing Zr foil in hot plate and heating it up, (b) Depositing solution drops on the Zr foil using the micropipette, (c) Waiting for the solution to dry, (d) Folding the Zr foil with the dried sample on it.

Chapter 8

Plutonium Level Schemes Search

8.1 Introduction

The isotope selective ultra-trace analysis of plutonium by RIMS requires an efficient excitation and ionization scheme. Performing the wide range searches for new transitions in plutonium at ORNL is particularly advantageous since our RILIS setup includes three tunable grating-based Ti:Sa lasers and IRIS2 platform allowing the ion signal to be recorded continuously. We started from plutonium ground state $5f^6 7s^2\ ^7F_0$, J = 0, frequency doubled Ti:Sa laser light with λ_1= 420.76 nm = 23,766.14 cm^{-1}, previously used as first step in [71, 8]. The next step is to search for second and third transitions and find the level scheme with highest yield. The next sections will describe the method and results for the second and third laser scans.

8.2 Second Step Scan

Resonance transitions for the second step from the ground state ^{7}F$_0$ level at E$_1$ = 23766.14 cm^{-1} were searched by scanning the second laser (λ_2) between 770 - 845 nm, while the third laser wavelength (λ_3) was fixed for non-resonant ionization. Around 20 significant peaks were observed, as numbered in Figure 8.1. The spectra are plotted as a function of $E_2 = E_1 + h\nu_2$, where ν_2 being the second laser frequency and E$_1$ = 23766.14 cm^{-1}. The λ_2 scan range corresponded to λ_2 = 11800-12950 cm^{-1} and the scan was repeated at two third-photon

energies of λ_3= 761.94 nm and λ_3= 763.07 nm, respectively. The λ_2 resonance centroids obtained with the two different third photon energies were found in excellent agreement. However the spectra with λ_3= 763.07 nm had higher yield and better resolution and these are the values reported in Table 8.1 with statistical uncertainties, FWHM and excitation wavelength for individual transitions.

8.3 Third Step Scan

Three-step ionization via the states marked in color in Table 8.1 were investigated. The first excitation was obtained by frequency-doubled light and the second and third transitions were accomplished with the fundamental laser light between 720 – 960 nm. The third laser was scanned to search for resonant transitions to high lying Rydberg and autoionizing states. Figures 8.2a-8.2f shows the third-step scans for each one of the chosen peaks of step two.

The third-step scans were performed over the course of several days and under different experimental conditions such as the ion source temperature, ion beam transmission, and laser power, etc., which were not the same when measuring the spectra, therefore the absolute intensity of the peaks is not reflected in the scans of Figure 8.2. However the relative intensities of the most prominent peaks were compared the same day under the same experimental conditions, but this comparison is still an estimated indication of their transition strengths as it could be affected by unknown fluctuations in laser power, temporal and spatial overlapping between the laser pulses during the scan. The results of this comparison is shown in Figure 8.3. The current of each scheme was measured in FC3. We found a three-step level scheme, shown in Figure 8.4, about 5 times larger than the one reported in literature [8]. This scheme was selected to perform efficiency and sensitivity measurements, described in Chapters 10 and 11.

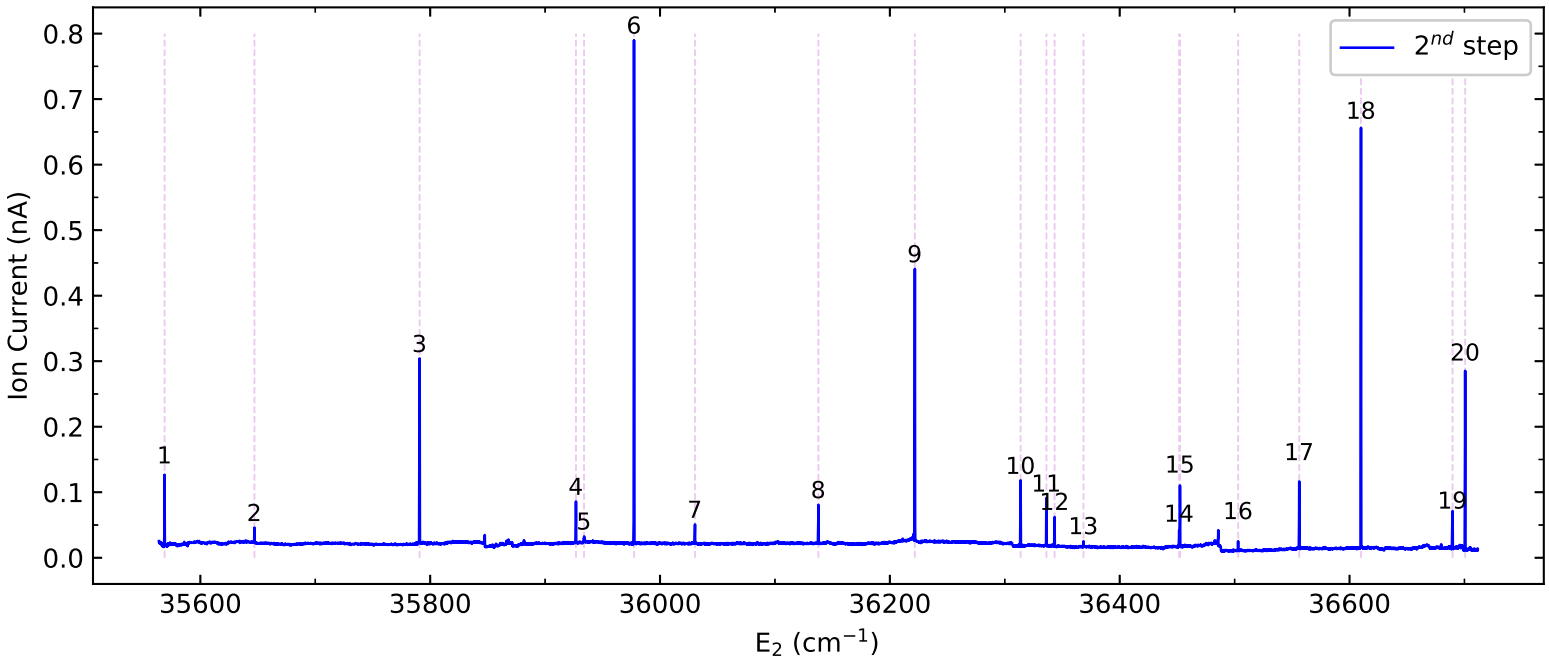
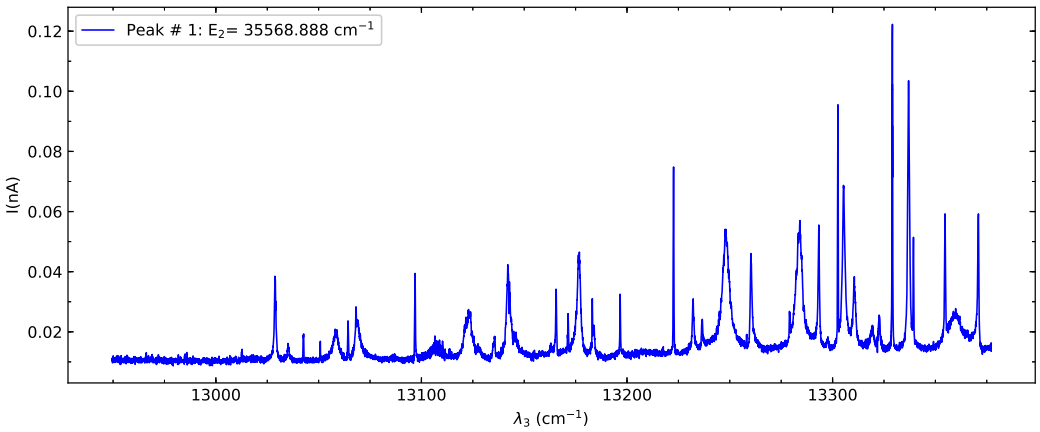


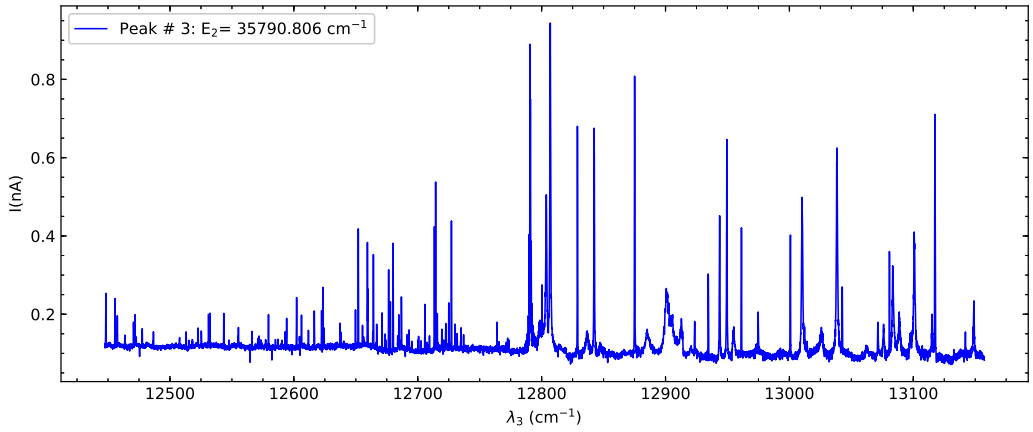
Figure 8.1: Measured λ_2 scan spectra with 20 resonance peaks observed, λ_1= 420.76 nm, λ_3= 763.07 nm. Light ping vertical lines help to guide the eye in the locations of the peaks. About 20 peaks were identified, in total 6 peaks were chosen for a third step scan.

Table 8.1: Measured energies of the second excited states and the FWHM of the resonance transitions. The given uncertainties for λ_2 are the standard deviations of the scan-up and scan-down measurements, not including the systematic error. The uncertainties for E_2 includes error propagation from λ_1 and λ_2. The pink shaded rows are the peaks we chose for the third-step scan. Units are in cm^{-1}.

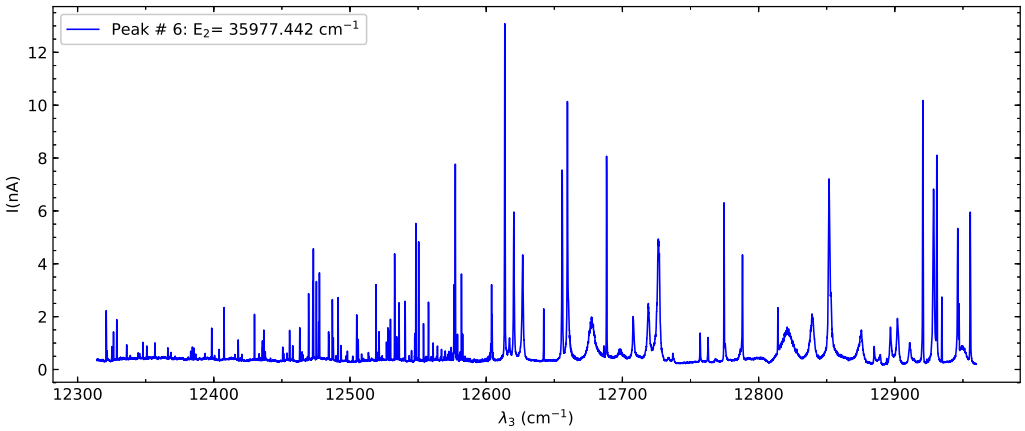
Peak #	λ_2	λ_2 (nm)	$\sigma(\lambda_2)$	FWHM	E_2	$\sigma(E_2)$
1	11802.748	847.260	0.002	0.256	35568.888	0.004
2	11880.912	841.686	0.014	0.176	35647.052	0.014
3	12024.666	831.624	0.003	0.294	35790.806	0.004
4	12160.718	822.320	0.002	0.199	35926.858	0.003
5	12167.732	821.846	0.037	0.999	35933.872	0.037
6	12211.302	818.914	0.003	0.315	35977.442	0.004
7	12264.242	815.379	0.005	0.260	36030.382	0.006
8	12371.684	808.297	0.005	0.243	36137.824	0.006
9	12455.616	802.851	0.001	0.257	36221.756	0.003
10	12547.641	796.963	0.001	0.285	36313.781	0.003
11	12570.118	795.538	0.002	0.172	36336.258	0.004
12	12577.212	795.089	0.002	0.235	36343.352	0.004
13	12602.380	793.501	0.011	0.224	36368.520	0.011
14	12685.629	788.294	0.006	0.227	36451.769	0.007
15	12686.364	788.248	0.002	0.286	36452.504	0.004
16	12736.965	785.116	0.003	0.198	36503.105	0.004
17	12790.117	781.854	0.004	0.244	36556.257	0.005
18	12843.845	778.583	0.002	0.250	36609.985	0.004
19	12923.506	773.784	0.008	0.371	36689.646	0.008
20	12934.519	773.125	0.001	0.263	36700.659	0.003



(a)

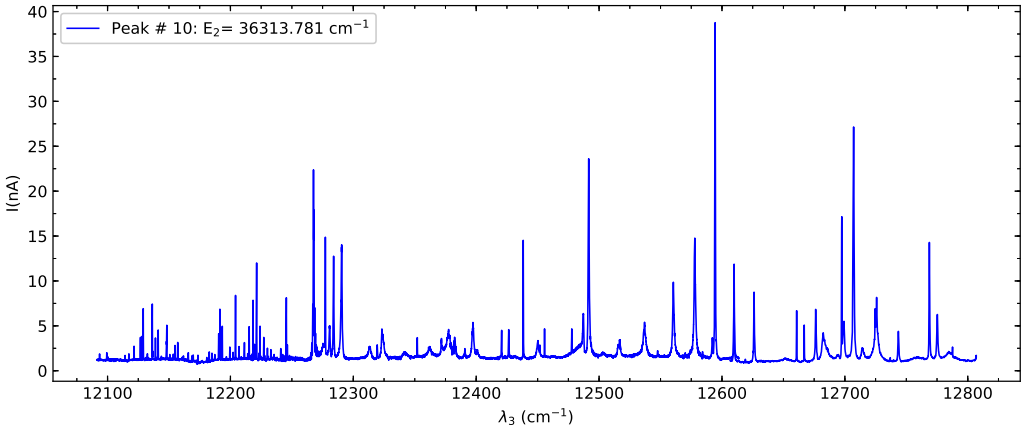


(b)

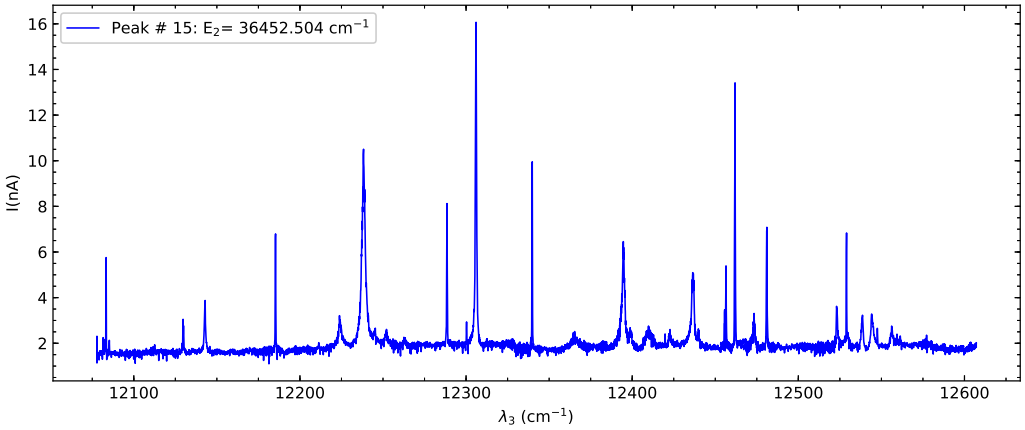


(c)

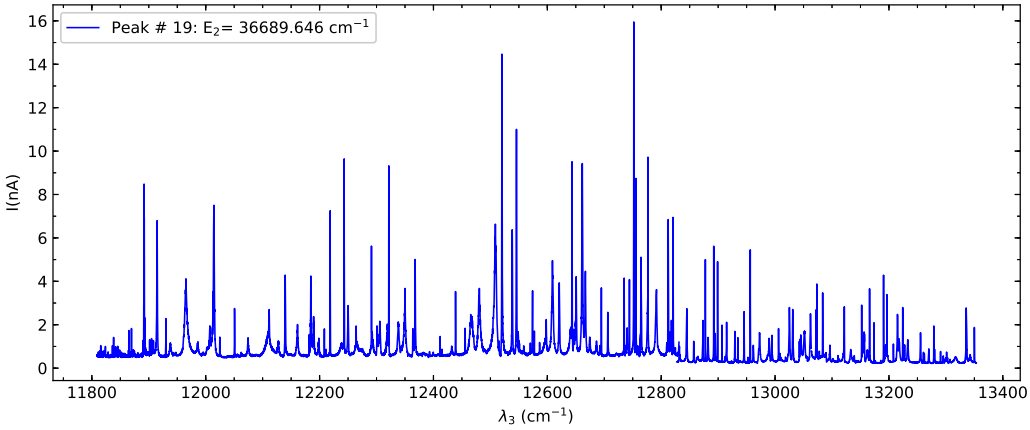
Figure 8.2: Third step ionization scans for (a) E_2= 35568.888 cm^{-1}, (b) E_2= 35790.806 cm^{-1}, (c) E_2= 35977.442 cm^{-1}, (d) E_2= 136313.781 cm^{-1}, (e) E_2= 36452.504 cm^{-1}, (f) E_2= 36689.646 cm^{-1}.



(d)



(e)



(f)

Figure 8.2: Figure 8.2 continued.

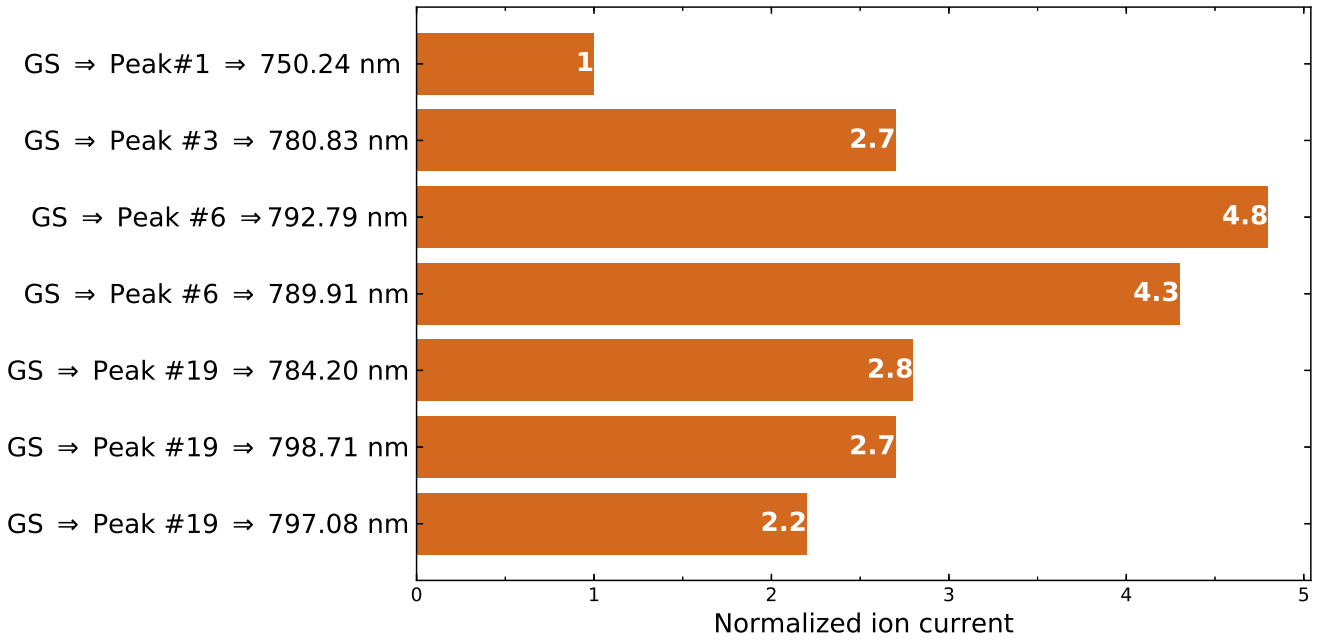


Figure 8.3: Comparison between three step scans with GS (ground state), λ_2= Peaks 1, 3, 6, 19 of Table 8.1. The current was measured under the same experimental condition in FC3. The current was normalized to λ_2=Peak #1, λ_3=750.24 scheme since it has been used previously in the literature [8]. We observed peaks 2-5 times larger than the one reported in literature.

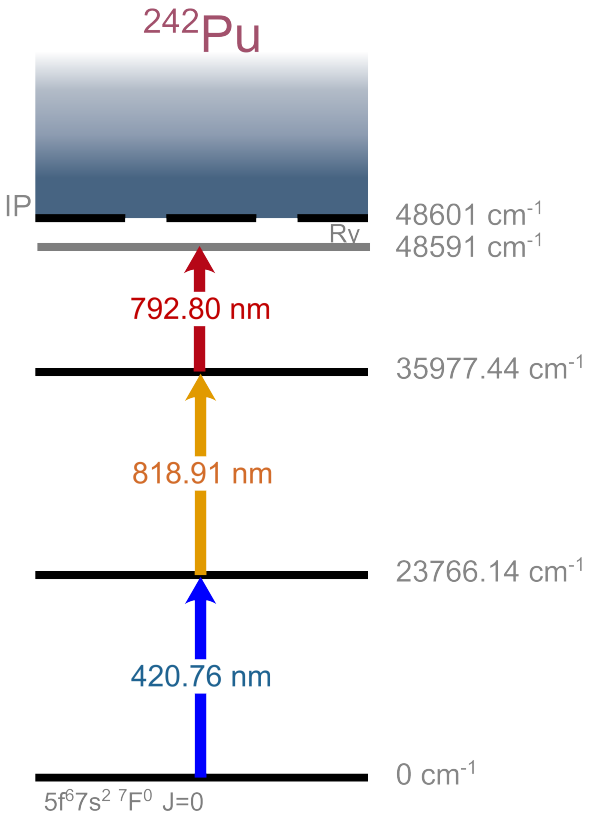


Figure 8.4: The highest yield three-step, three-photon ionization scheme in our searches for ^{242}Pu. This level was used for for the ionization efficiency measurement and sensitivities tests.

Chapter 9

Saturation and Power Broadening

9.1 Introduction

At sufficiently large laser intensities the optical pumping rate on an absorbing transition becomes larger than the relaxation rates. This results in a noticeable decrease of the population in the absorbing levels. This saturation of the population densities also causes additional line broadening, this effect is referred as saturation broadening. Detailed discussions about this topic can be found in [144, 145, 146, 147].

For simplicity we can consider a two-level system with a lower state $|1\rangle$ and an upper state $|2\rangle$. One can introduce the dimensionless saturation parameter S_0, which describes the ratio of the pump rate p_{12} from $|1\rangle$ to $|2\rangle$ and the average relaxation rate r_2 of $|2\rangle$. It can also be interpreted as a standardized intensity

$$S_0 = p_{12}/r_2 = I/I_{sat} \tag{9.1}$$

The saturation can be also observed in the correlation between the used laser intensity I and the resulting ionization rate r or extracted ion current. When applying a RIMS excitation ladder, the correlation for any excitation step can be described as

$$r(I) = r_{res}\frac{I}{I + I_{sat}} + \alpha_{nr} I + r_0 \tag{9.2}$$

In this context, the saturation intensity I_{sat} represents the intensity which is needed to obtain half of the maximum ionization rate r_{res}. The linear term α_{nr} reflects a contribution from non-resonant ionization. This term vanishes, if the photon energy $E(\nu)$ is smaller than the difference between the IP and any populated atomic state. A constant background of r_0 might be present, caused by non-resonant ionization due to laser radiation of previous steps in the excitation ladder or surface ionization in the ion source.

The saturation of the individual transitions by the laser power P can be described on the basis of equation 9.2.

$$I = I_0 + A\frac{P}{P + P_{sat}} \tag{9.3}$$

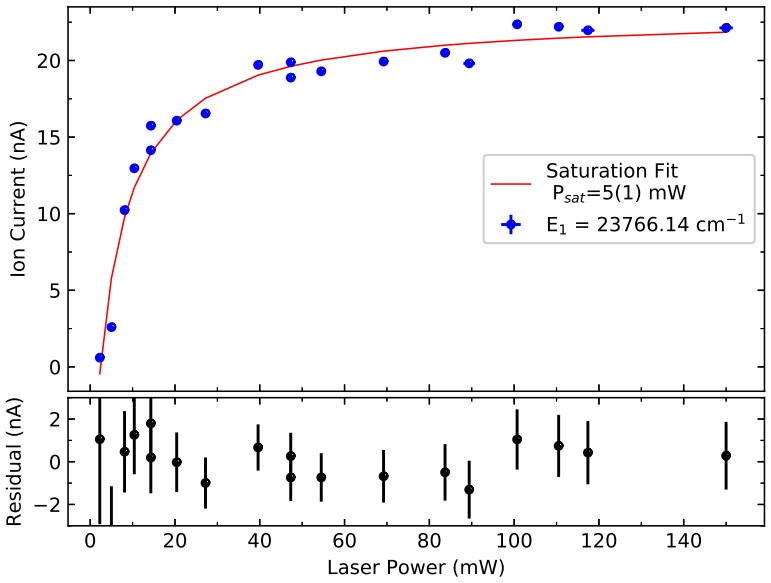
where I is measured ion current, P is measured laser power, P_{sat} is the saturation laser power, I_0 is the background ion current, and A is a constant The saturation power P_{sat} describes the laser power required to reach half the ionization rate of the convergence amplitude A. The saturation values measured in this case are not exclusively determined by physical properties of the optical excitation process, but also consider apparatus-related variables as well as the spatial extent of the laser radiation in the interaction region, which can not be reproduced exactly with each measurement. The saturation power determined in this way thus reflects an apparatus saturation power which, under similar conditions, saturates the optical excitation in the ionization volume. The specified values are therefore to be interpreted as an order of magnitude which shows whether the available laser power is in principle sufficient for the corresponding transition.

9.2 Saturation Measurement

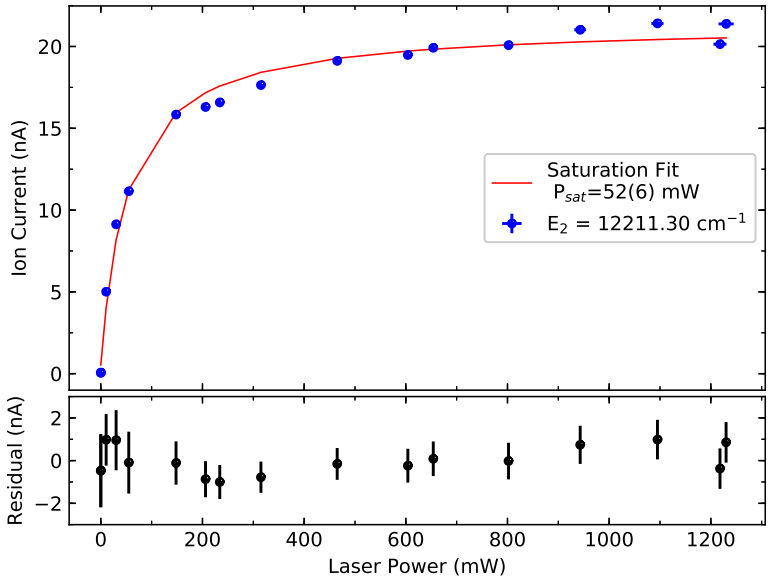
The laser power used in the present study was between 1 - 2 W fundamental output for second and third excitation and 100 – 150 mW frequency-doubled output for the first excitation step. We measured the laser power needed to saturate each excitation step in the laser room, before the laser go to the IRIS2 platform. We used three level ionization scheme of the Figure 8.4, corresponding to E2 = 35977.49 cm^{-1} and E3 = 48591.16 cm^{-1} since this three-level scheme seemed to result in higher ion currents. The ion current was measured

as a function of the laser power for each excitation step and the data were then fitted to the formula 9.3. For each measurement of laser power vs current for each excitation step we performed a time scan, which I fitted to obtain the average current.

The fitting results are presented in Figure 9.1. From the fittings we obtained P_{sat} = 5(1), 52(6), and 388(35) mW for the first, second, and third excitations, respectively. This means that the selected three-step transitions can be saturated with laser powers that are easily available. From the laser room typically 70 – 80% of the laser power was injected into the ion source, therefore the actual saturation power P_{sat} for the excitation steps was about 70-80% of the above fitted values.

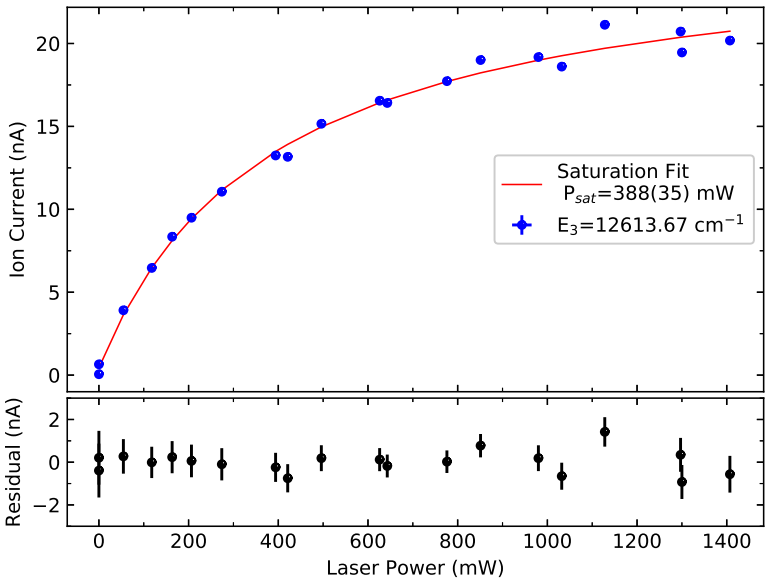


(a)



(b)

Figure 9.1: Saturation curves of the (a) first laser step, (b) second laser step, and (c) third laser step excitations via $E_2 = 35977.442$ cm^{-1} level. Dots represent the measured data and lines are fits to equation 9.3. We include a residual plot for each fitting.



(c)

Figure 9.1: Figure 9.1 continued.

Chapter 10

Efficiency Measurements of Actinides

10.1 Introduction

In Chapters 2.2 and 2.4, I described the importance of the ultratrace detection for actinides. One key component in the ultratrace detection is the efficiency of the ion sources as it determines the size of sample needed, selectivity, background and production of ions.

High temperature cavity ion sources have been used for more than 30 years at isotope separator on-line (ISOL) facilities for producing radioactive ion beams of elements of relatively low ionization potentials [148, 149, 150, 151]. More recently, cavity-type surface ionization sources [152, 153, 154, 155, 156] are employed for thermal ionization mass spectrometry (TIMS) systems for the purpose of improving the ionization efficiency and thus detection limits of low-level isotope analyses of elements such as U, Th, and Pu for which the conventional filament-type thermal ionization sources have very poor efficiencies. Measured ionization efficiencies of 3–8.5% for U [152, 153, 156] ,1–3% for Th [152, 154] and 4-10% for Pu [155, 156] have been reported for those sources.

Extensive spectroscopy studies on resonant ionization schemes for actinide elements, including U, Th, and Pu using Ti:Sapphire [157, 158, 159, 8] and diode [160] lasers have been carried out by the LARISSA group at the University of Mainz. Their studies revealed numerous atomic energy levels in U and Th that were previously not known and identified various excitation and ionization schemes optimized for Ti:Sapphire or diode lasers. Based on their prior work, we selected several three-step, three-photon ionization schemes and

then conducted further spectroscopic studies to exploit new schemes and search for the most efficient scheme for U and Th. However for Pu the we based our search from one level scheme previously reported [8] as starting point as there are not ionization schemes reported in the literature as with U and Th.

Therefore in this chapter I will describe the general procedure for efficiency measurements on Pu, which is the same procedure for U and Th.

10.2 Experiment Description

After the development of ionization level schemes for Pu, described in Chapter 8, we selected the best level scheme found in our extensive search; this means the scheme with the highest yield in current, shown in Figure 8.4. We used a much smaller sample of 4 µg compared with the sample of 40 µg used for the search level schemes. This sample contained 9.97×10^{15} atoms, this is calculated from the equation 7.1 and replacing the variables for the experimental values:

$$^{242}Pu\ \frac{\mu\text{moles}}{\text{g}} = \frac{4.1403\mu\text{moles}}{29.7684\ \text{g} + 0.002} = 0.4096\ \frac{\mu\ \text{moles}}{\text{g}} \tag{10.1}$$

$$0.4096\ \mu\frac{\text{moles}}{\text{g}} = 0.4096\ \frac{\mu\text{moles}}{\text{g}} \times 6.0221 \times 10^{23} mol^{-1} \times 10^{-6} \tag{10.2}$$

$$= 9.971 \times 10^{15}\text{atoms} \tag{10.3}$$

This sample was was placed inside the sample tube (Figure 6.2) and gradually heated to release neutral ^{242}Pu atoms as the ion source was resistively heated to high temperatures up to 400 A. The laser ionized ^{242}Pu ion current extracted from the ion source and after mass separation was continuously recorded in Faraday cup 4 until it dropped below 2-3 nA, indicating that the sample materials were mostly evaporated, as shown in Figure 10.1. During the process of the efficiency measurement, we blocked the lasers to prove the selectivity of the laser and determine our background, which as shown in Figure 10.1. In this way the ratio of the laser ion current and laser-independent background current was monitored over the course of the measurement.

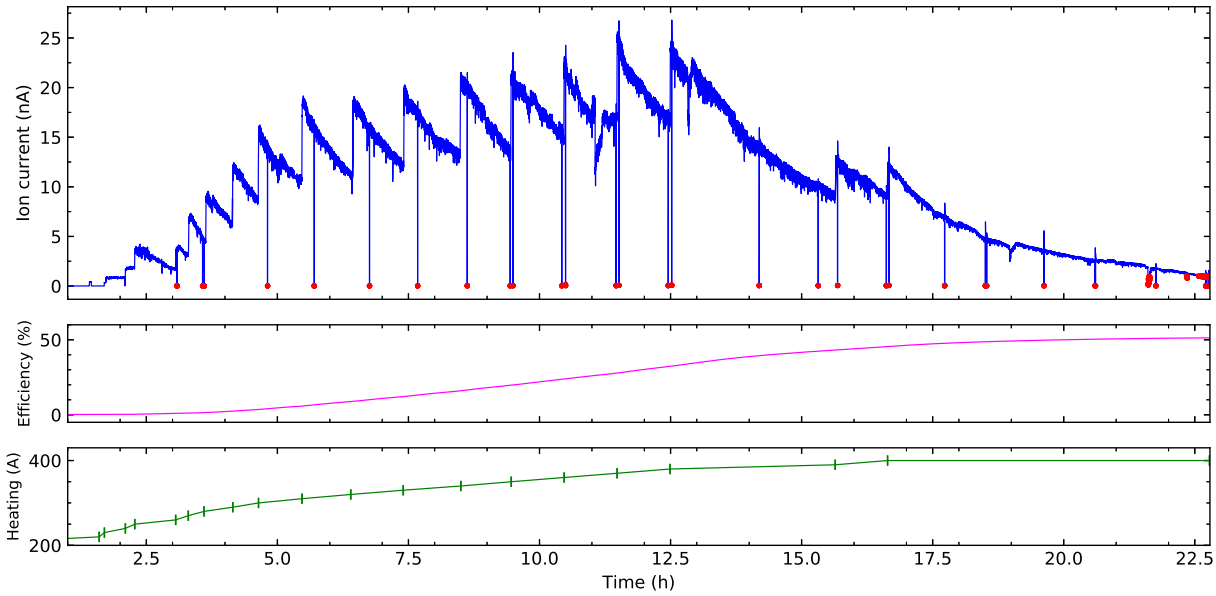


Figure 10.1: Development of a typical efficiency measurement on ^{242}Pu. Blue line shows the efficiency measurement on a sample of 9.97×10^{15} atoms of ^{242}Pu. The sample was gradually heated and the signal of laser ions as well as of non-resonant background was recorded as a function of time. The surface ionization (non-resonant background) was measured by blocking the lasers, shown in red points. Magenta line shows how the evolution of the efficiency value and the green line shows the range of heating, with a maximum of 400 A.

In Figure 10.2 we can see that after unblocking the laser beams the ion current goes higher than it was before blocking the lasers and then goes back to normal after a minute. This effect shows that there is an accumulation of neutral atoms in the ionizer when the lasers are blocked, therefore depletion of the ionizer volume is strongly enhanced with the laser ionization. The depletion of the gaseous sample is slowed down without laser beams, as the source provides a slightly better buffer capability for neutral atoms than for ions.

The ionization efficiency was calculated as the ratio of the integrated total number of detected ions over the total number of neutral atoms in the sample:

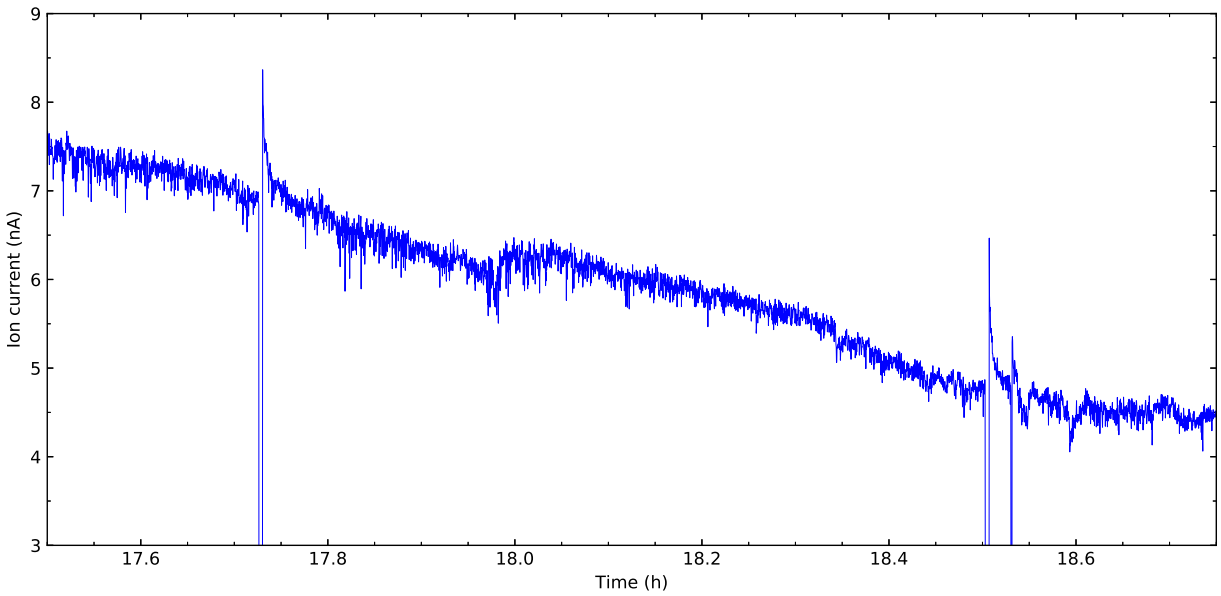


Figure 10.2: Zoom in the spectrum to show the effect in the ion current after unblocking the lasers. The current jumps above the value that had initially before blocking the lasers

$$\text{Ionization efficiency} = \frac{\#\text{ ion detected}}{\#\text{ neutral atoms in the sample}} \tag{10.4}$$

$$= \frac{\text{Total current (A)} \times \text{time (s)}/e_{\text{charge}}}{\#\text{ neutral atoms in the sample}} \tag{10.5}$$

$$= \frac{5.11 \times 10^{15} atoms}{9.971 \times 10^{15} atoms} * 100\% \tag{10.6}$$

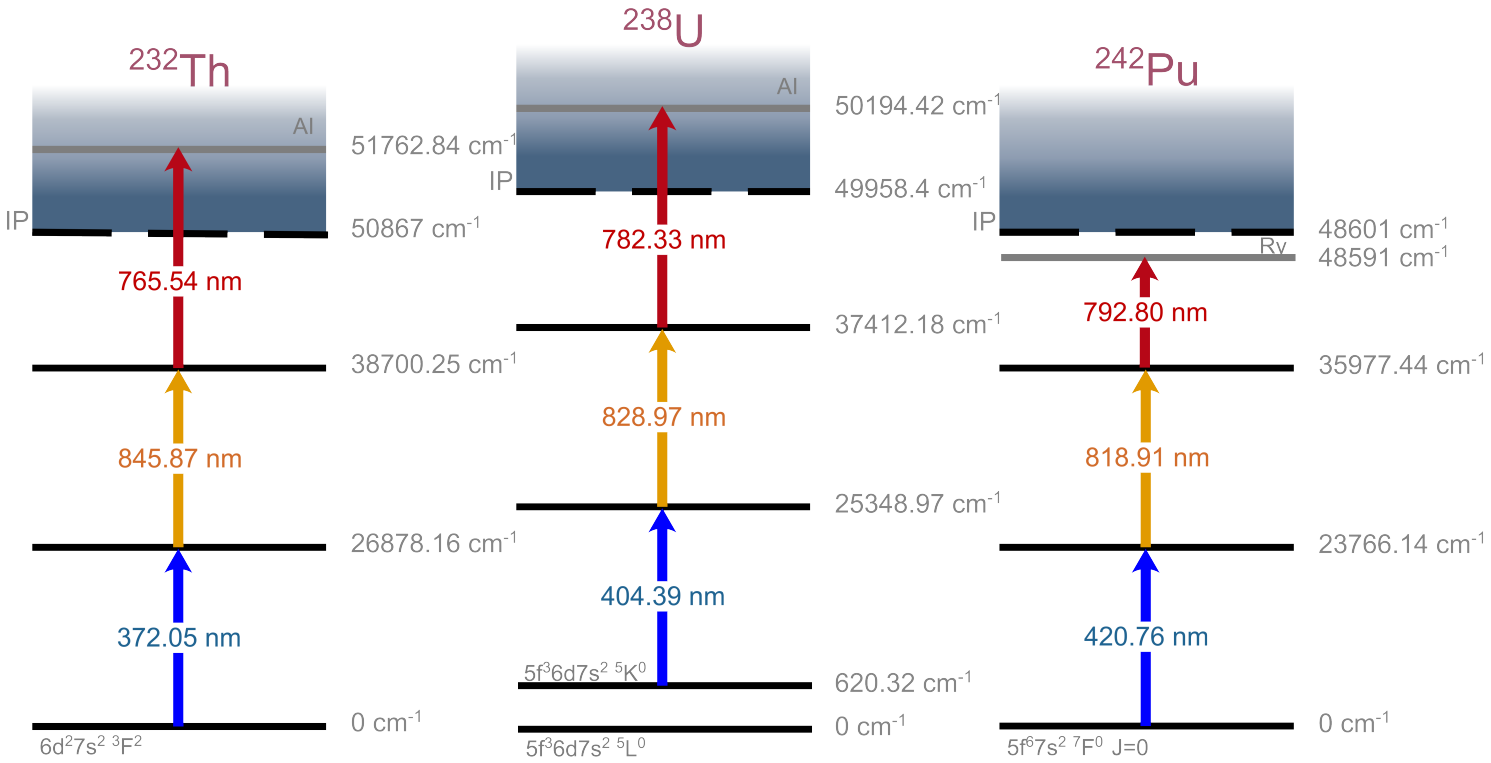
$$= 51.29\% \tag{10.7}$$

For the scheme shown in Figure 8.4, the overall ionization efficiency obtained was about 51.29%, calculated with equations 10.4-10.6. The uncertainty was calculated from the ion current $\frac{\delta_{\text{ion current}}}{\text{ion current}} = 0.05$ and the neutral atoms $\frac{\delta_{\text{neutral atoms}}}{\text{neutral atoms}} = 0.06$ giving a total uncertainty of $\sqrt{0.05^2 + 0.06^2} * 100 = 8.06$ and $8.06\% \times 51.29 = 4.13\%$.

10.3 Results

Using the method described above, we calculated the efficiency for U, Th and Pu. For U and Th we used a level schemes already investigated by [159] for Th and [157, 160] for U

showed in Figure 10.3. The samples for U and Th were prepared similarly to the described process in Chapter 7. The difference in the preparation for Pu was the need for more personal protective equipment and a detailed procedure for dealing with a highly radioactive samples. The sample materials were made from 1000 ppm U or Th atomic absorption (AA) standard solutions, which contain U and Th in a nitric acid matrix in the form of uranyl nitrate and thorium nitrate, respectively. Small samples containing about 40 μg of U or Th atoms were used to evaluate the source, as I mentioned earlier for Pu we used 4 μg. U and Th samples were dry in Ti foil following the same procedure mentioned in Chapter 7. The overall efficiency for Th is 32%, for U 9 % and for Pu 51%, errors and wavelengths for the transitions are given in Figure 10.3. These efficiencies reported here are the highest reported for these elements with any technique. Our next step is to focus on the performance of our RIMS setup with smaller materials down to femtogram to test our sensitivity. These results are reported in the next Chapter.



(a) 32 ± 3% **(b)** 9 ± 0.7% **(c)** 51 ± 4%

Figure 10.3: Ionization level schemes chosen for the efficiency measurements for (a) ^{232}Th, (b) ^{238}U and (c) ^{242}Pu.

Chapter 11

Sensitivity Measurements with Plutonium

11.1 Introduction

Various analytical methods have been developed and are being utilized by laboratories around the world to meet the challenge of providing increasingly sensitive, precise, and accurate information in actinides research. The group from Bürger et al. at ORNL have a complete review on sensitivity limits for actinides using various techniques [74], here I will focus on sensitivity studies using RIMS. The potential for achieving very high sensitivity and elemental selectivity with laser ionization methods was demonstrated by G. S. Hurst et al. in 1976 [161]. Since then sensitivity measurements have been performed on actinides using RIMS [162, 8, 163]. However the lowest limit reported is of the order of 10^4 atoms.

In the next section I will describe our work for the first sensitivity measurements at ORNL using different concentration of ^{242}Pu sample detected in a channeltron detector. For all sensitivity measurements we used the best level scheme found in our searches, shown in Figure 8.4.

11.2 Channeltron Detector

For the purpose of the sensitivity measurements, I installed a MAGNUM Electron Multiplier (EM) 5900 series.This EMr was installed after FC4 in Figure 11.2. Electron multipliers are durable and efficient detectors of positive and negative ions. Figure11.1 illustrates the basic structure and operation of the EM. A glass tube having an inner diameter of approximately 1 mm and an outer diameter of generally 2-6 mm is constructed from a specially formulated lead silicate glass, this glass exhibits the properties of electrical conductivity and secondary emission. When an ion strikes the input face of the EM typically produces 2-3 secondary electrons. These electrons are accelerated down the channel by a positive bias. The electrons strike the channel walls, producing additional electrons (and so on) until, at the output end a pulse of 10^7 to 10^8 electrons emerges. For positive ions, the input is generally at a negative potential of 1200 to 3000 volts and the output is at ground. For detection of negative ions, the input is generally at ground or some positive potential and the output is at a high positive voltage. Today, electron multiplier detectors are the most widely used detector in quadrupole and ion trap mass spectrometers.

The gain of a Channeltron is defined as the ratio of the output current to the input current (I_o/I_i). Gain is, in general, a function of the secondary emission coefficient (δ) of the glass, the applied voltage (V), and the length-to-diameter ratio (l/d) of the tube. As the

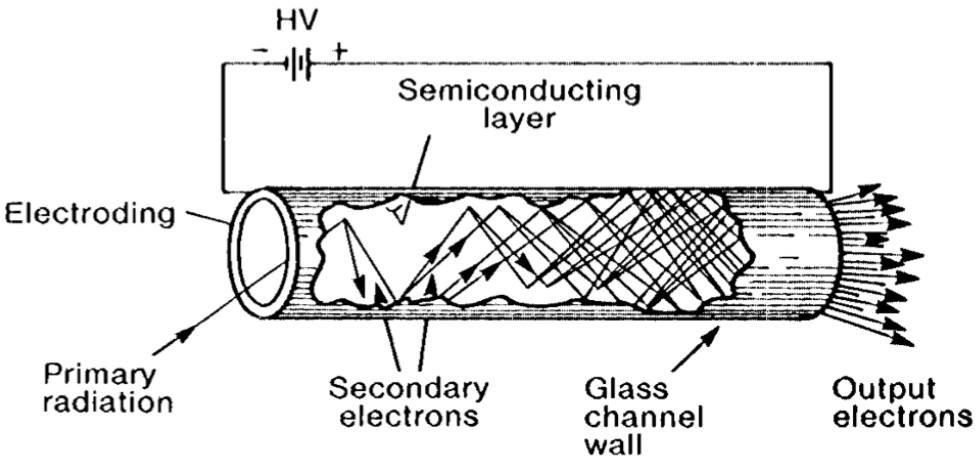


Figure 11.1: Cutaway view of an electron multiplier detector. Basic operation schematics.

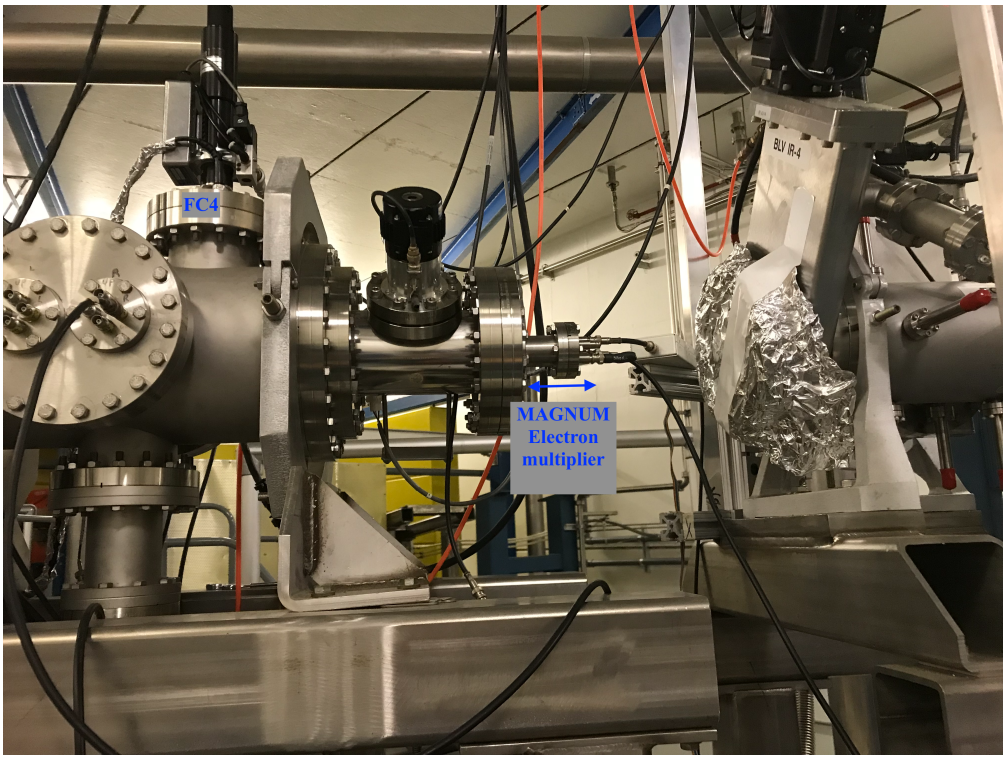


Figure 11.2: IRIS2 beamline end showing the channeltron detector installed after FC4.

voltage applied to the CEM is increased, a point is reached where space charge saturation occurs.

11.2.1 Channeltron installation

Since the FC4 can be remotely be move in and out of the beamline, we decided to place the channeltron after the FC4, shown in Figure 11.2 . For the operation of the EM we required a power supply and a detection method. We used an ET Enterprises multi-channel scaler/counter timer module MCS-CT3 coupled with a ET Enterprises amplifier/discriminator AD8 as counting system. The IRIS2 platform is inaccessible when is operating, therefore we need a system to communicate with the EM from the laser room. We used fiber optic cable to communicate with the power supply and the MCS-CT3. A schematic diagram of the connections are shown in Figure 11.3.

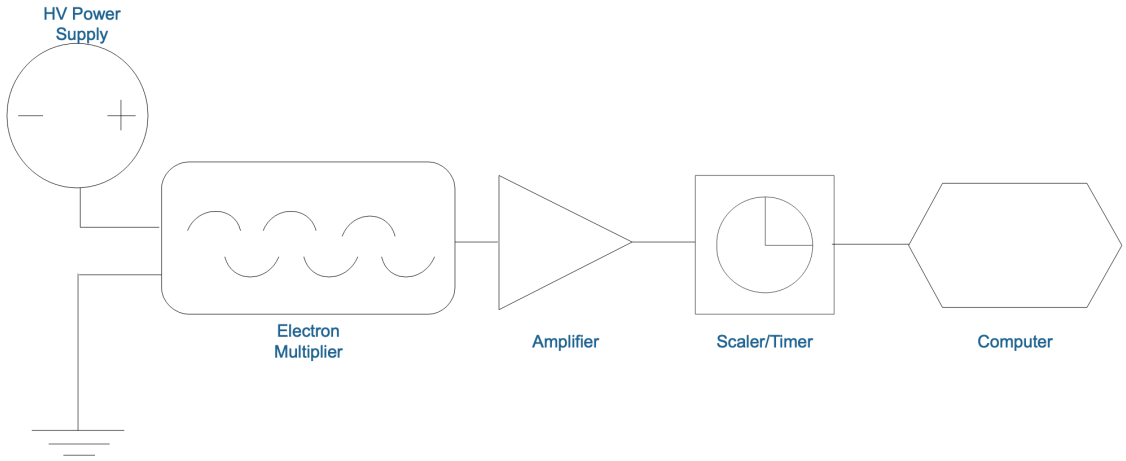


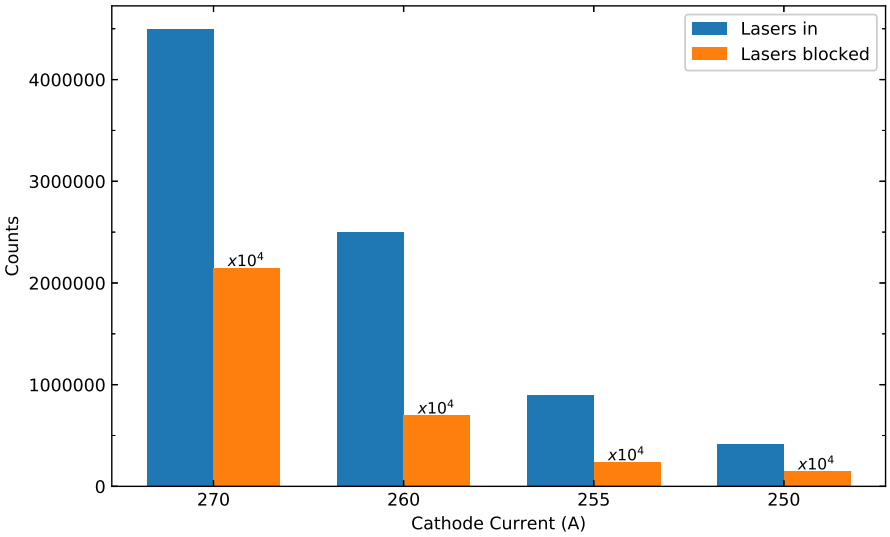
Figure 11.3: Electronics diagram of system detection using the electron multiplier.

11.3 Channeltron Characterization

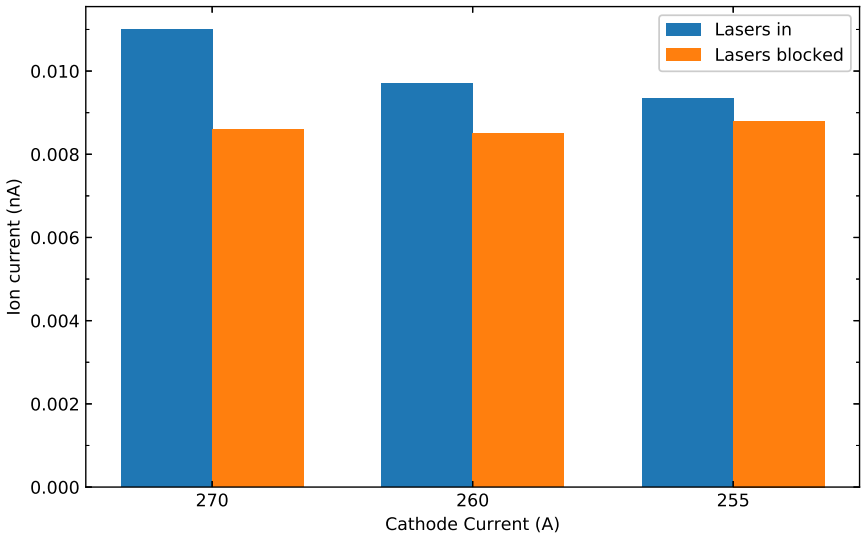
Since this was the first time we use a single counter in the IRIS2 platform, we made a comparison between the intensities of the channeltron and faraday cup after the high resolution magnet (FC3) and the last faraday cup of the beam line (FC4) using 10 ng of ^{242}Pu. For this comparison we change the cathode current to different values (hence the temperature of the ion source) and recorded the intensities for the channeltron and faraday cups. During this process we also blocked the lasers and the beam to compare the background between them. Table 11.1 summarized the values obtained for each cathode value. Figures 11.4a, 11.4b and 11.4c show a comparison between lasers in and out in channeltron, FC's 3 and 4. In the three cases the counts decrease with cathode current, however at 250 A the ion current in FC3 is about the same as the background and the ion current in FC4 the signal and background are indistinguishable.

Table 11.1: Channeltron and faraday cups intensities comparison between different cathode values.

Cathode (A)	270	260	255	250
Channeltron				
All lasers in	4.5E+06	2.5E+06	9E+05	4.2E+05
All lasers blocked	215	70	24	15
Laser 1 blocked		80		
Laser 3 blocked	1E+05		2E+04	9008
No beam	0	0	0	0
FC4 (nA)				
All lasers in	0.0110	0.0097	0.00935	
All lasers blocked	0.0086	0.0085	0.0088	
Laser 3 blocked	0.0085	0.0090		
No beam	0.0083	0.0085	0.0090	
FC3 (nA)				
All lasers in	0.0128	0.0113	0.01114	0.010852
All lasers blocked	0.01065	0.01047	0.010675	0.01065
Laser 1 blocked			0.0107	
Laser 3 blocked	0.01065	0.0105	0.0107	
No beam	0.0106		0.0107	0.01066

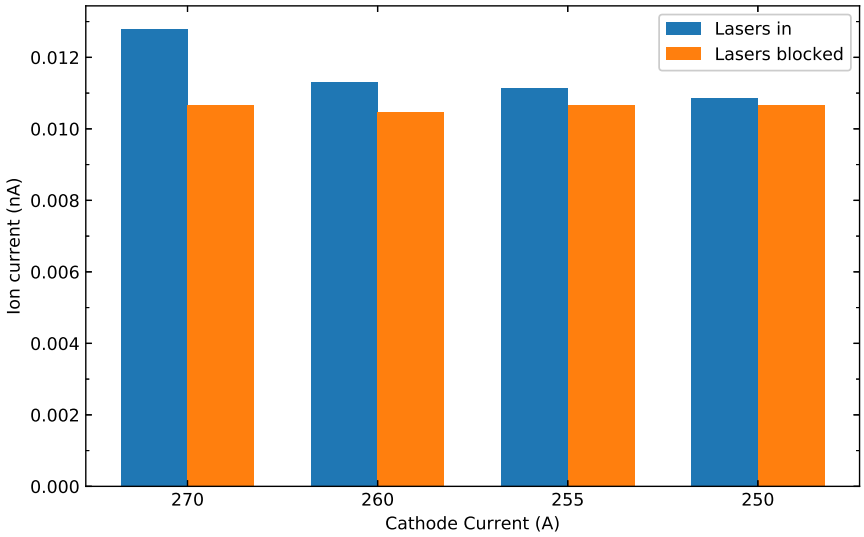


(a)



(b)

Figure 11.4: (a) Comparison between the channeltron counts of lasers blocked and unblocked using ^{242}Pu beam . The signal of the lasers blocked is enlarge 10^4 times for a better appreciation; (b) Comparison between the FC4 ion current of lasers block and unblocked using ^{242}Pu beam. We could not record a value for 250 A as we could not distinguish between background and signal; (b) Comparison between the FC3 ion current of lasers blocked and unblocked using ^{242}Pu beam.



(c)

Figure 11.4: Figure 11.4 continued.

11.4 Background Characterization

Ultra-trace analysis requires a very good understanding of the background contamination in the analytic system. In order to characterize the Pu background in our system we measured ^{242}Pu with an empty source. We used an ion source that has not been used with ^{242}Pu before to make sure that the ion source is clean from any ^{242}Pu residuals. However, we observed residual of ^{242}Pu in the system, the counts were up to 500 using very high value in the cathode of 380 A, this is shown in Figure 11.5.

11.5 Detection Limits

The standard ^{242}Pu sample received from NBL was prepared with trace amounts of other isotopes listed in Table 11.2. We used a 10 fg of ^{242}Pu sample and we used the sample isotopic composition to measure the detection limit of our system as the present isotopes are 4 or 5 orders of magnitude lower than ^{242}Pu. First we tuned the system for ^{242}Pu, this signal was above the background, at 280 A the signal recorded was 26,000 counts/s compared to 500 counts/s at 380 A measured with the empty source in Section 11.4. After tuning for ^{242}Pu

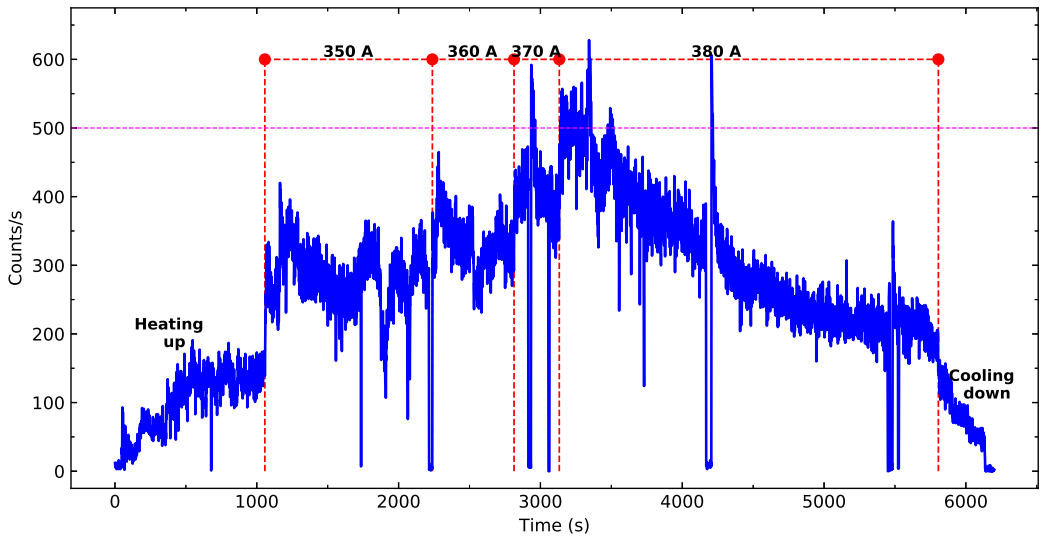


Figure 11.5: Characterization of the background, we detect up to 500 counts/s using a very high value of cathode 380 A. The magenta line is the reference line at 500 counts/s. Each value of the cathode is marked, the maximum value was 380 A, we let it exhaust for some period of time.

and confirming is above background, we searched for the rest of the isotopes by changing the magnets.

In our search we could observed ^{240}Pu, which is 4 orders of magnitude lower than ^{242}Pu. We confirm was plutonium by blocking the lasers and seeing the counts drop to background, see Figure 11.6. We also confirm that was ^{240}Pu as the experimental ratio between these two isotopes match the expected ratio from the sample. This result gives a detection limit of 10^{-18} g, as the initial sample was 10 fg and we could detect 4 orders of magnitude lower than that. This limit corresponds to 6×10^3 atoms. This sensitivity is the lowest reported for actinides.

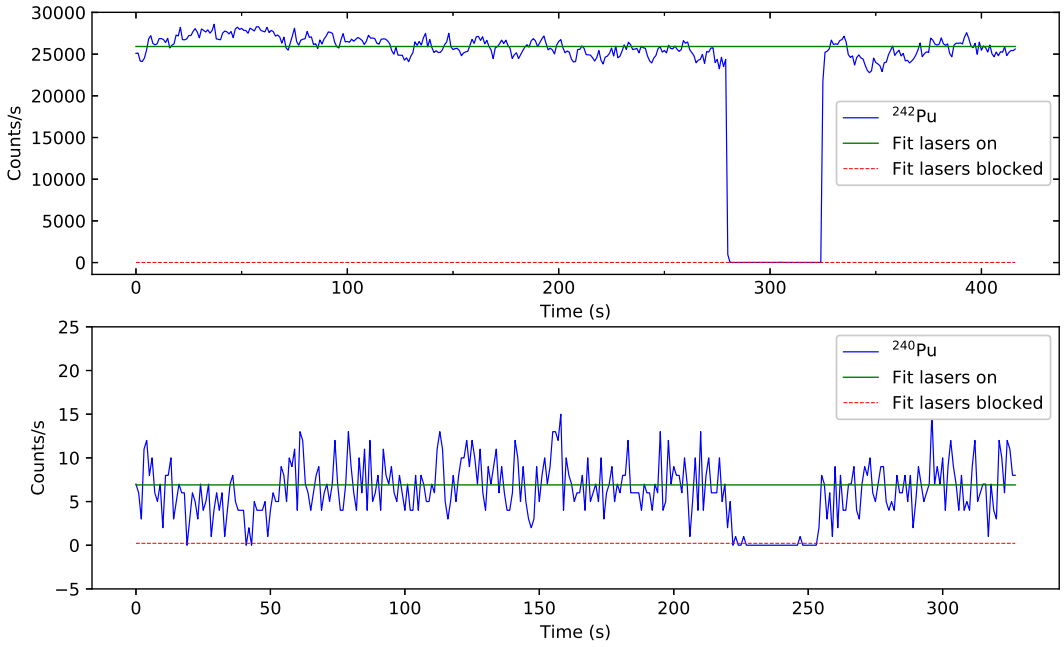


Figure 11.6: Intensities of ^{242}Pu and ^{240}Pu showing laser effect by blocking the lasers, confirming we observed Pu. The fitted lines are to obtain the average counts observed for each isotope.

Table 11.2: Isotopic composition of the ^{242}Pu sample and the respective isotopic ratio. Experimental counts were obtained by fitting the experimental data of Figure 11.6. The experimental ratio for ^{240}Pu match the expected ratio of the sample.

Isotope:	^{238}**Pu**	^{239}**Pu**	^{240}**Pu**	^{241}**Pu**	^{242}**Pu**	^{244}**Pu**
Atom Percent:	0.00419	0.00478	0.01974	0.02466	99.94623	0.0004
Uncetainty:	0.00026	0.00012	0.00038	0.00034	0.00065	0.0001
Expected ratio:	4.2×10^{-5}	4.8×10^{-5}	2×10^{-4}	2.5×10^{-4}	1	4×10^{-6}
Experimental counts:			7		25917	
Experimental ratio:			2.6×10^{-4}			

Chapter 12

Plutonium Rydberg States

The Rydberg atom is the atom in which one of its electrons is in the highly excited state with large magnitude of the principal quantum number. The concept of Rydberg states started back with the spectral line emissions of the hydrogen atom. In 1885, Balmer created the formula to describe the wavelengths of the visible series of atomic H, giving by:

$$\lambda = \frac{bn^2}{n^2 - 4} \tag{12.1}$$

where b=3545.6 Å. The parameter b is the limit that this series converge and n $\geq$ 3. Equation 12.1 give us the wavelengths of the transitions from n=2 states to higher lying levels. Balmer created this formula empirically and only applies for these specific transitions.

Johannes R. Rydberg based his empirical formula in the experimental results by [164] and [165]. He realized that the wavenumbers E (the inverse of the wavelength in vacuum) of the series members were related by,

$$E_n = E_{lim} - \frac{R_y}{n^*}^2 \tag{12.2}$$

$$n^* = n - \delta_n \tag{12.3}$$

$$\delta_n = \delta_0 + \frac{a}{(n - \delta_0)^2} \tag{12.4}$$

Where $R_y = 109737.316cm^{-1}$ is the Rydberg constant, E_{lim} is the limit of the series, n* is the effective quantum number where δ_n is the quantum defect explained more in detail in Section 12.2, δ_0 is the asymptotic limiting value of the quantum defect and a is a constant. Furthermore he noticed from [164] work that all the spectral lines from an atom are related, leading him to a general expression for the wavenumbers of lines connecting different series,

$$E_2 - E_1 = R_y(\frac{1}{(n_1 - \delta_2)^2} - \frac{1}{(n_2 - \delta_1)^2}) \tag{12.5}$$

Rydberg formulated equations 12.2 and 12.5 before Niels Bohr made his atomic model in 1913. With Bohr's atomic model, the number n had a physical meaning, which is the quantization of the angular momentum. In the hydrogen atom, Bohr's model assumes the electron of mass m_e in a circular orbit of radius r around the positive charge +e, balancing the centripetal acceleration of the electron with the Coulombic force from the nucleus we have,

$$\frac{m_e v^2}{r} = \frac{kZe^2}{r^2}; k = \frac{1}{4\pi\epsilon_0} \tag{12.6}$$

where ϵ_0 is the permittivity of free space and v is the electron speed. Quantization of the angular momentum $m_e vr = n\hbar$, where $\hbar$ is the Plank constant, give us the relationship ,

$$r_n = \frac{n^2\hbar^2}{Ze^2mk} = \frac{a_0 n^2}{Z} \tag{12.7}$$

where a_0 is the Bohr radius. The total energy of a state is obtained by adding its potential and kinetic energy,

$$E = \frac{mv^2}{2} - \frac{kZe^2}{r} = \frac{-k^2Z^2e^4m}{2n^2\hbar^2} \tag{12.8}$$

The transitions between energies is then given by,

$$E_2 - E_1 = \frac{k^2Z^2e^4m}{2\hbar^2}(\frac{1}{{n_1}^2} - \frac{1}{{n_2}^2}) \tag{12.9}$$

thus from equation 12.5 we have that,

$$R_y = \frac{k^2 Z^2 e^4 m}{2\hbar^2} \tag{12.10}$$

12.1 Rydberg Properties

The radius of a Rydberg atom increases drastically with n according to the equation 12.7, where $a_0 = 0.529 \times 10^{-8}$ cm, therefore for $n > 100$ Rydberg atoms reach macroscopic sizes (> 1 µm). Even that the dependence of r is inversely proportional to Z, its ionic charge, this dependence is weaker than the n dependence. From equation 12.7 and the angular momentum we can get the period and velocity in terms of n,

$$v_n = \frac{Z v_0}{n}; \quad v_0 = \frac{\hbar}{a_0 m_e} \tag{12.11}$$

$$T_n = \frac{2\pi}{\omega} = \frac{2\pi * r}{v} = \frac{2\pi a_0 n^3}{v_0 Z^2}; \tag{12.12}$$

where v_0 is the atomic unit of velocity, thus the velocity of a Rydberg atom is very small compared with the atom in ground state or low excited states. On the contrary, the period T_n increases rapidly with n increasing and Z decreasing.

Rydberg atoms are very sensitive to external electric fields, the Stark effect. To illustrate this lets consider the H atom under an electric field, thus the potential that the electron experience along the z axis can be written as,

$$V = -\frac{k}{|z|} + Ez \tag{12.13}$$

This equation is plotted in Figure 12.1. If we set the derivative of equation 12.13 to zero we find the saddle point is located at $Z = -E^{-1/2}$ where the potential is $V_s = 2\sqrt{kE}$. If we equate this energy with the binding energy of the Rydberg electron we obtained the classical field of ionization,

$$E_c = \frac{{R_y}^2}{4kn^4}; \quad E_c = \frac{1}{16 n^{*4}} (\text{atomic units}) \tag{12.14}$$

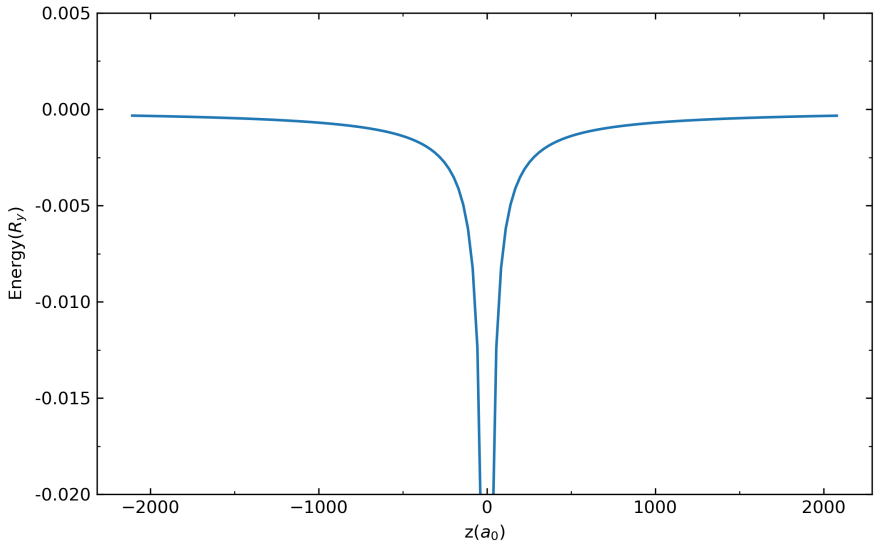


Figure 12.1: Stark - Coulomb potential for a Rydberg atom in a static electric field of 5.14kV/cm in the z direction.

where n^* is the effective principal quantum number, $n - \delta_\ell$ and δ_ℓ is he quantum defect.

12.2 Quantum Defect

Quantum defect is explained in detail in [166, 167, 168, 169]. The term of quantum defect was given by Schrödinger , even that Rydberg included in his formula he called a constant [166]. The quantum defect is the result of the ionic core of the other electrons in the atom. The quantum defect accounts for the corrections to the Coulomb potential by the core electrons. We can introduce an effective quantum number $n^* = n - \delta_{n,\ell}$. Already on the basis of the hydrogen wave functions we see that the probability to find the Rydberg electron within the core decreases with larger ℓ, therefore the quantum defect should also decrease with larger ℓ.

One important property of quantum defect theory is that the scaling relations we already saw in the hydrogen case remain valid, with the principal quantum number n being replaced by n*.

12.3 ^{242}Pu Spectrum with Rydberg States

In our search for efficient level schemes, we observed Rydberg series in three spectra converging to the ionization potential of neutral Pu which is equivalent to the ground state of Pu^+ ($^8F_{1/2}$). The series are labeled Scheme A, Scheme B and Scheme C. Scheme A (Figure 12.2a) corresponds to E_2= 35977.42 cm^{-1}, Scheme B (Figure 12.2b) corresponds to E_2= 36689.62 cm^{-1}and Scheme C (Figure 12.2c) corresponds to E_2= 35790.80 cm^{-1}. The observed ranges are n=39-87 for Scheme A and n= 39-79 for Scheme B. In the case of Scheme C we could not identify the Rydbergs states as there was perturbations all around the spectrum. However as presented in Subsection 12.4.2 we can determine the IP without identifying the Rydberg states by the quantum defect histograms.

12.4 Determination of the Ionization Potential

The first ionization potential of the atom (IP), i.e., the binding energy of the outermost valence electron, is one of the most fundamental quantities of each element in the Periodic Table. Its accurate determination is important for determining the electronic structure of an atom as the first ionization potential is directly connected to the atomic spectra. The IP's can also serve for a better understanding of relativistic effects in heavy elements, which are expected as a result of the relativistic mass increase of the inner electrons [170]. The most accurate value for IP is the one obtained for Hydrogen with a precision of 10^{-12}, however the theoretical predictions and experimental measurements of the IP become more challenging as the element gets heavier. This challenge is due to a complexity in the Coulomb attraction and repulsion properties of more than two interacting charge particles by cause of strong shielding effects.

Figure 12.3 gives a compilation of the IP values of all the elements and its precision shown in logarithmic scale. The ionization energy exhibits periodicity on the periodic table, generally increases moving from left to right across an element period (row). Ionization is at its minimum value for the alkali metal on the left side of the table and a maximum for the noble gas on the far right side of a period, which is the trend observed in Figure 12.3.

Ionization decreases moving top to bottom down an element group (column). This is because the inner electrons screen the outer electrons from the attractive force of the nucleus.

Lanthanides and actinides present a different trend as the one described above. The atomic systems of these series are formed by consecutive filling of the 4f or 5f electron shell, respectively, located inside an outer s^2 valence electron pair, this leads to a similar chemical behavior along the series. The atomic structure of the actinides and lanthanides make theoretical predictions difficult as they they can only address particularly clear spectra with a maximum of one open shell outside a closed electron core, actinides and lanthanides have three to four open shells. As we can see in Figure 12.3, the precision measurements of IP for lanthanides and actinides is rather limited.

In this work we report our studies of IP in plutonium using Rydbergs convergence. We present two analytical methods to obtain the IP.

12.4.1 Method 1

The first step to determine the ionization potential is to identify the members of the Rydberg series. One method for the identification can be done with the plot of n*vs $\delta_n mod_1$. From equation 12.2 and 12.3 we have:

$$n^* = \sqrt{\frac{R_M}{E_{lim} - En}} \tag{12.15}$$

$$\delta_n mod_1 = mod_1(\delta_n) \tag{12.16}$$

$$= mod_1(n - n^*) \tag{12.17}$$

$$= mod_1(-n^*) \tag{12.18}$$

$$= mod_1(-\sqrt{\frac{R_M}{E_{lim} - En}}) \tag{12.19}$$

The members of the series are then chosen when for a given value of E_{lim} there is a converging behavior, i.e. when the members of the series have a constant trend for that given E_{lim}. We identified Rydbergs in 3 level schemes with E_2= 12211.29 cm^{-1} (Scheme A), and E_2= 112923.49 cm^{-1} (Scheme B) and E_2= 12024.67 cm^{-1} (Scheme C). As mentioned before for

Scheme C we could not identify the rydberg states with this method, however for Scheme A and B we were able to identify them.

The Figures 12.4a and 12.4b shows a visualization of the process of this method, in these figures we can recognize the alignment of the series members, in fact we can distinguish 2 series in Figure 12.4a. We can also observe for different E_{lim} the trend of the series, the red dashed line is the average of the fitted quantum defect for reference. The colorbar of the graph shows the intensity of each peak, this helps to identify any perturbation, as we can see in Figures 12.4a and 12.4b there is a perturbation peak around n*=67.

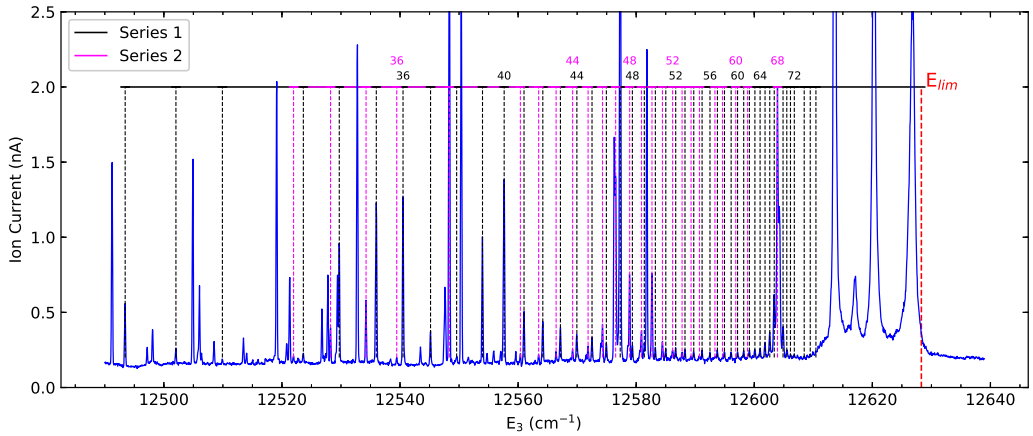
Once identified the Rydbergs states, I fitted the equations 12.2-12.4 to get E_{lim}, this is shown in Figures 12.5a -12.5c. The results are summarized in Table 12.1. The IP values for both series are very close.

12.4.2 Method 2

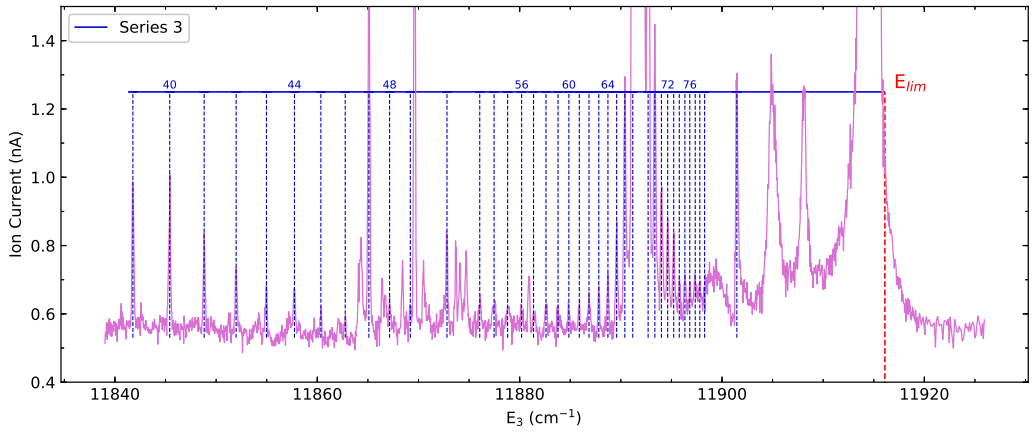
A second method to obtain the IP is described in more detail in [171]. It consists of obtaining δ histogram for different E_{lim} values, for each histogram we obtain the maximum count and these maxima are plotted against their respective E_{lim}. The algorithm to build the δ-histograms was written in Python. This analysis allows the extraction of the position of the ionization limit from a Rydberg scan without identifying the Rydberg states like presented in Method 1 in the previous section. In Figures 12.6a-12.6c is shown the histograms for a range of E_{lim}= 48500-48700 cm^{-1} with 0.1 steps (in total 2000 bins). In both schemes we observe a defined peak that is zoomed in the middle graph for each scheme. For each peak we fitted a Gaussian and the fitted center is what we consider as the IP.

Table 12.1: Results of Rydberg-Ritz fit for schemes A and B. The given uncertainties are the standard deviation of the fit. Last column is the value of IP derived from the series limits.

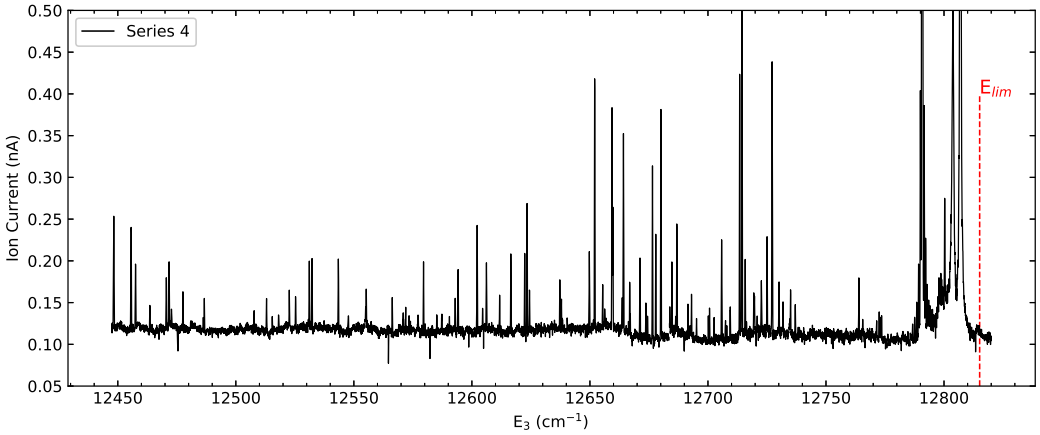
Series	λ_1	λ_2	$\mathbf{E}_{lim}$	**IP**
Scheme A-series 1	23766.14	12211.302	12628.290	48605.731
Scheme A-series 2	23766.14	12211.302	12628.170	48605.611
Scheme B	23766.14	12923.506	11916.134	48605.780



(a) Scheme A



(b) Scheme B series converging to the first ionization potential.



(c) Scheme C

Figure 12.2: We identified in total 4 series converging to the IP. In the case of Scheme C we could not identify the rydbergs exactly as the were perturbations.

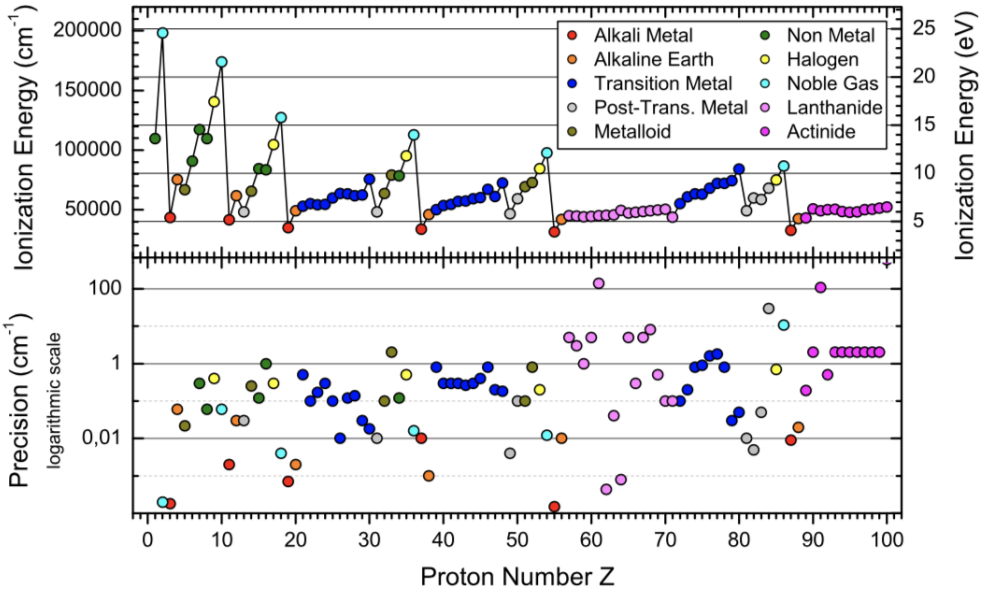
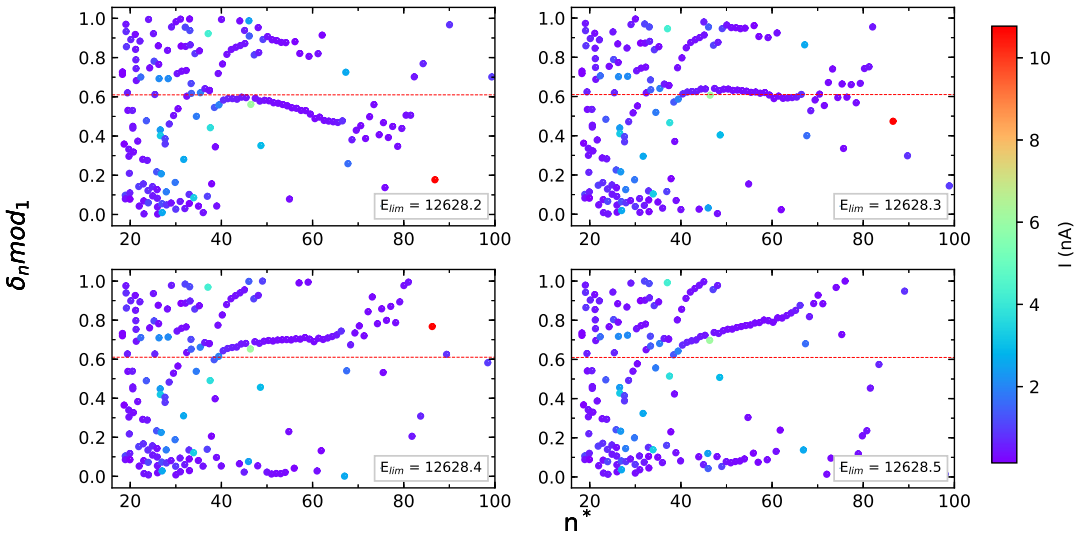
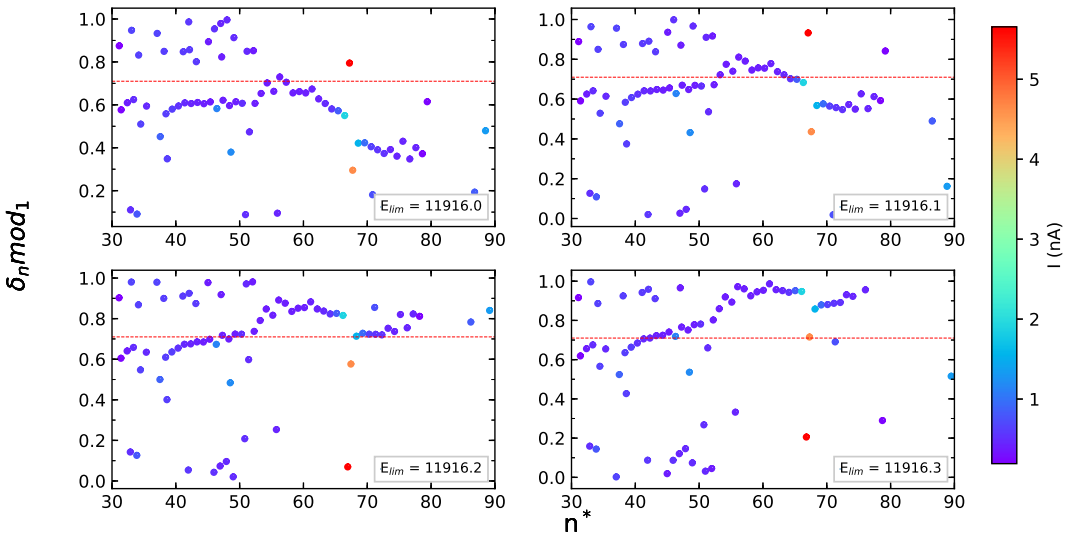


Figure 12.3: IP values as a function of Z and their precision. Figure taken from [9]

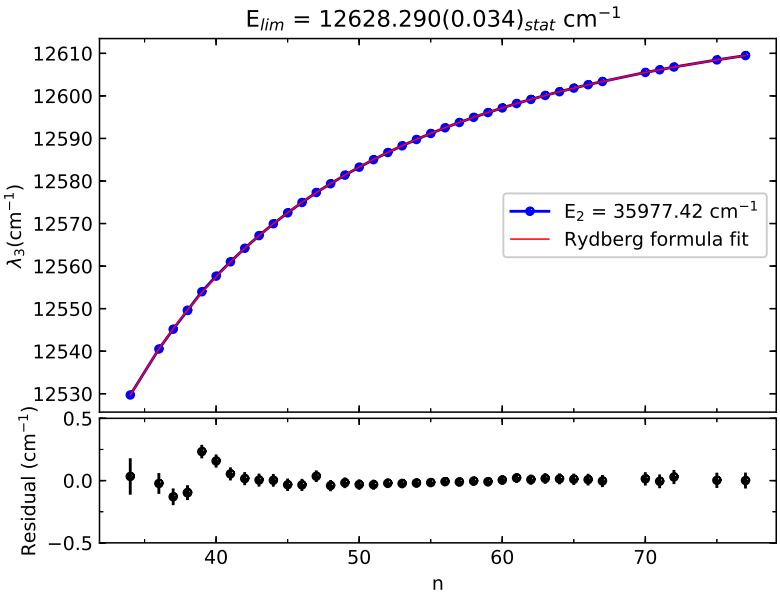


(a)

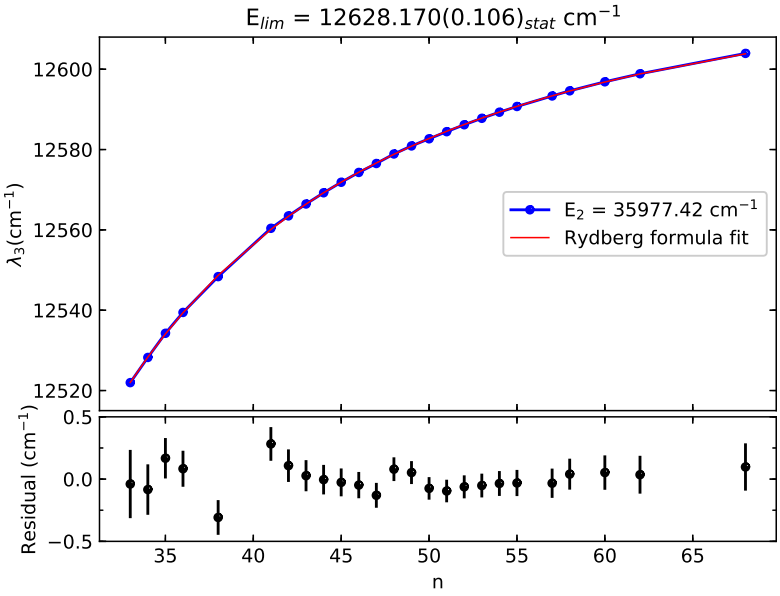


(b)

Figure 12.4: Identification of the Rydberg states with the graph n* vs quantum defect. As seen in the graphs, the Rydberg states group in a constant for the "right" IP value for (a) Scheme A and (b) Scheme B.

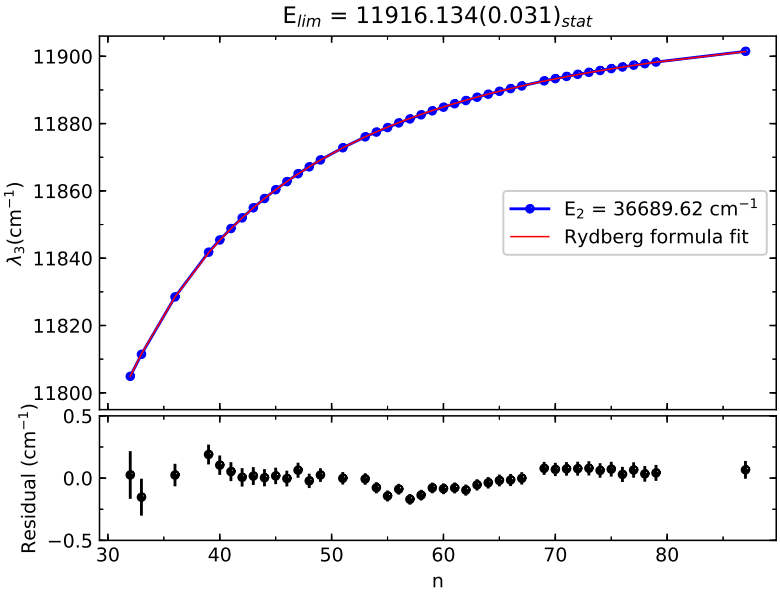


(a)



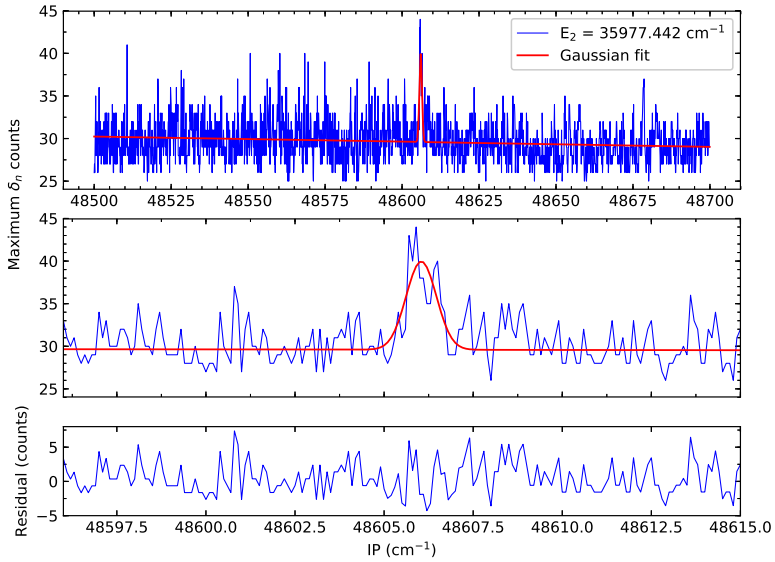
(b)

Figure 12.5: Rydberg-Ritz fit of (a) Scheme A series 1, (b) Scheme A series 2 and (c) Scheme B. (Top) Measured energies (dots) of the Rydberg states and calculated energies (solid line) using the fitted parameters. (Bottom) Fit residuals with experimental statistical uncertainties as the error bars.



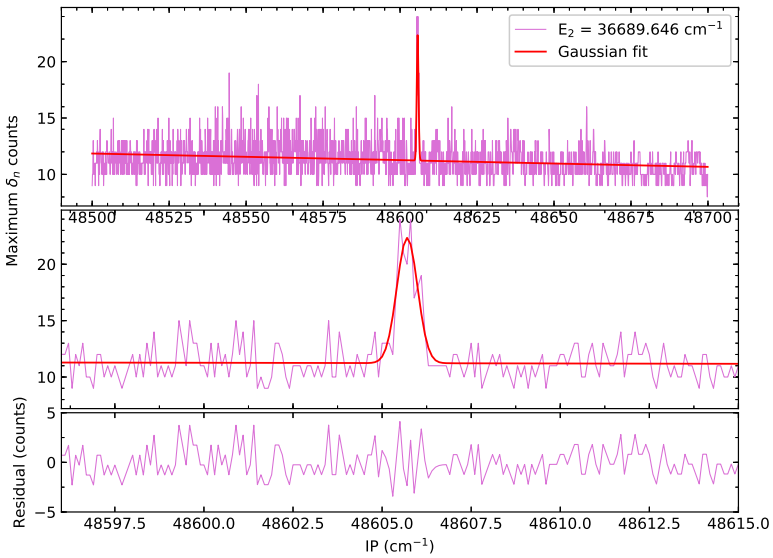
(c)

Figure 12.5: Figure 12.5 continued.

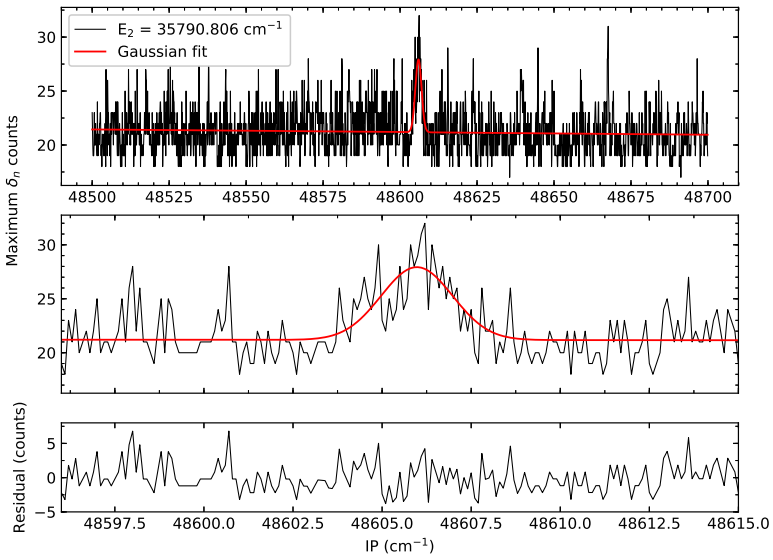


(a) Scheme A.

Figure 12.6: Variation of maximum histogram counts at different energy limits for scheme A and B. The middle graph for each scheme shows a zoom across the central peak. The fitted Gaussian is plotted as the red curve. The position of this peak equals to E_{lim} = 48605.965 for scheme A, E_{lim} = 48605.539 for scheme B and E_{lim} = 48605.987 for scheme C. The bottom graph for each scheme shows the residual of the fitting.



(b) Scheme B.



(c) Scheme C.

Figure 12.6: Figure 12.6 continued.

12.5 Pu IP Error Analysis

Before reporting our values I would like to explain the error analysis. The final IP is obtained by adding the energies of the first and second level to the energy limit of the third level calculated by the different methods:

$$IP(Pu) = \nu_1 + \nu_2 + E_{lim} \tag{12.20}$$

The uncertainty in measuring the laser wavelengths was dominated by the absolute accuracy of the wavelength meter, which is 600 MHz or 0.02 cm^{-1} according to 3-sigma criterion. This uncertainty was taken as the systematic error of our measurement. For the step 1 we doubled the frequency therefore Δ_W=2*0.02 cm^{-1}

It has been observed that there was a scan-direction dependent shift that the spectral line centroids obtained by scan-up and by scan-down were slightly different with an average difference of about 0.04 cm^{-1}. To mitigate this effect, each spectrum was measured at least twice by scan-up and scan-down, respectively. The line centroids were then determined as the average values of the scan-up and scan-down measurements and the experimental statistical uncertainty was calculated as the standard deviation of the measurements. This procedure was used for all the spectra measured in this study. The statistical error for E_{lim} comes from the fitting in both methods. The Table 12.2 summarized the errors for each step.

12.6 Discussion

The most recent calculation of the plutonium IP was published in 1997 [172] and is this value the one accepted by the National Institute of Standards and Technology (NIST) [10]. The IP was calculated using a technique called *photoionization threshold*, this method uses RIMS in the presence of an electric field. The wavelength of the laser for the ionizing step is scanned across the threshold in the presence of the electric field strength E. The ionization threshold W_{th} is indicated by a sudden increase of the ion count rate. Determination of W_{th} for different values of the electric field strength E and extrapolation to E = 0 leads directly

to the first ionization potential. The relation between the electric field and the ionization is given by the equation:

$$W_{th} = IP - const\sqrt{E} \tag{12.21}$$

Using 400 pg of Pu and three step excitation schemes $\lambda_1 = 649.072$ nm, $\lambda_2 = 629.751$ and $\lambda_3 \approx 579$ nm this group obtained a value of IP = 48601 (2) cm^{-1}.

A most accurate IP value for Pu was calculated about the same time in 1993 by [54]. In this work they used both techniques laser photoionization threshold and Rydberg convergence. For the photoionization threshold they use two - and three-step laser excitation using 6 different combinations of level schemes. The IP's obtained for each level scheme were averaged giving a value of IP= 48582(6) cm^{-1}. For the Rydberg convergence method they used 4 different combinations of level schemes giving an average value IP=48604(1) cm^{-1}. In this paper there is also a report of other IP values obtained with other techniques such as surface ionization and spectroscopy, however the values obtained by [54] has been the most accurate of all values reported.

In Table 12.3 are summarized the most recent values of IP for plutonium. The photoionization threshold measurements results are the lowest and divert from the Rydberg convergence IP limits within their quoted uncertainty. The results from the two analyzing methods and level schemes agree within their error. The final result for the IP from this work reported in Table 12.3 was averaged over all values from the 4 series observed and the two methods, the uncertainties were propagated through all the values. The IP obtained in this work is 3 times more accurate than the previously reported values. Figure 12.7 shows the trend of the IP's for the actinides series with the new value obtained in this work.

Table 12.2: Results with statistical and systematic errors for both methods in A and B schemes. MiSi means Method i, Series i with i 1 or 2. All units are in cm^{-1}.

	Value	Δ_{stat}	Δ_{wm}	IP	Total Δ_{stat}	Total Δ_{sys}
			Scheme A			
ν_1	23766.14	0.060	0.04			
ν_2	12211.302	0.012	0.02			
E_{-lim}-M1S1	12628.290	0.034	0.02	48605.731	0.070	0.049
E_{-lim}-M1S2	12628.170	0.106	0.02	48605.611	0.122	0.049
E_{-lim}-M2S1	12628.536	0.046	0.02	48605.978	0.077	0.049
E_{-lim}-M2S2	12628.176	0.053	0.02	48605.618	0.081	0.049
			Scheme B			
ν_1	23766.14	0.060	0.04			
ν_2	12923.506	0.012	0.02			
E_{-lim}-M1	11916.134	0.031	0.02	48605.780	0.069	0.049
E_{-lim}-M2	11915.893	0.014	0.02	48605.539	0.063	0.049
			Scheme C			
ν_1	23766.14	0.060	0.04			
ν_2	12024.666	0.012	0.02			
E_{-lim}-M2	12815.176	0.099	0.02	48605.982	0.116	0.049

Table 12.3: Plutonium IP values obtained with Rydberg convergence and photoionization threshold techniques. The value reported for this work is the average of all the values obtained from Table 12.2 and the uncertainty is given by the error propagation of those values.

IP (cm^{-1})	**Ref.**	**Method**
48 582(6)	[54]	Photoionization threshold
48604 (1)	[54]	Rydberg convergence
48601 (2) (NIST)	[172]	Photoionization threshold
48605.748 $(95)_{stat}$ $(49)_{sys}$	This work	Rydberg convergence

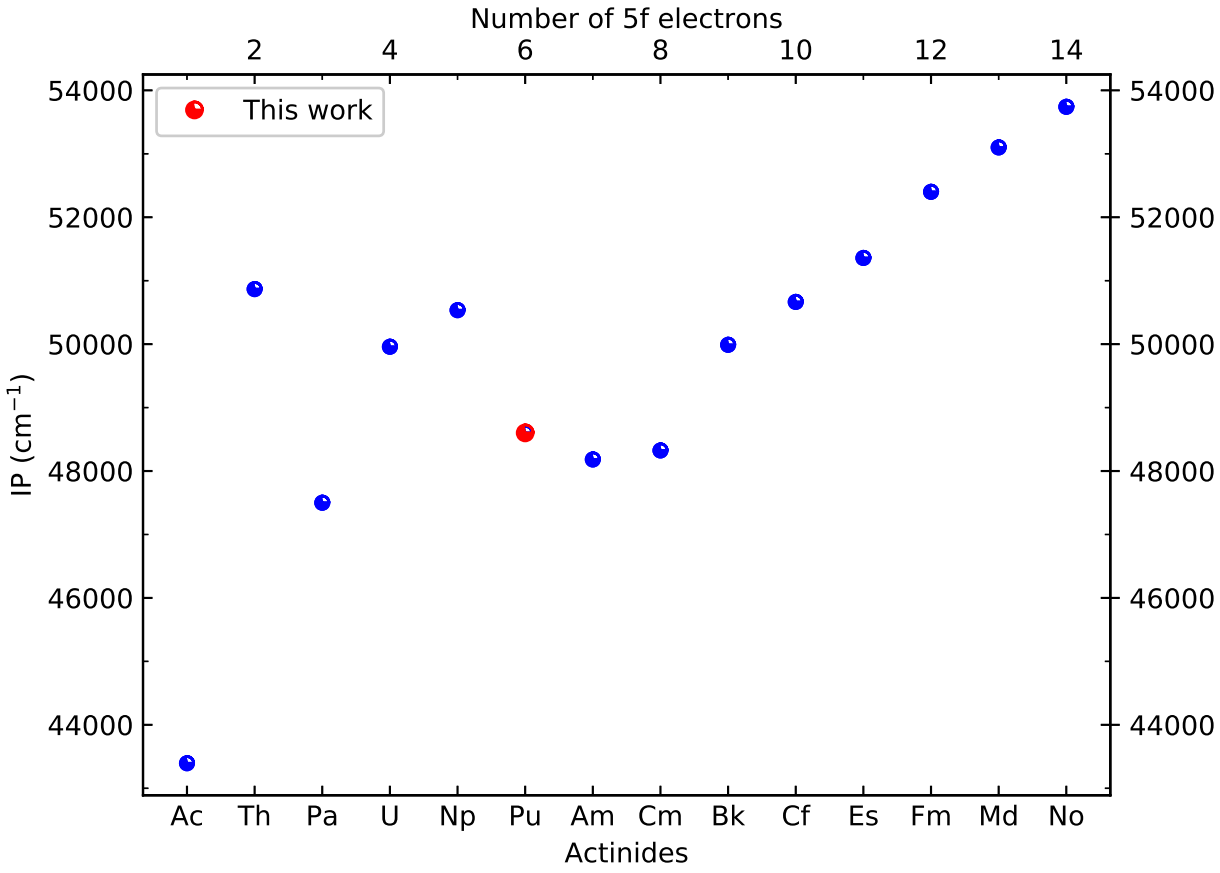


Figure 12.7: IP values for the series of actinides. Experimental data is taken from [10]. The new experimental result for Pu of this work is included in red dot.

Chapter 13

Conclusions

Motivated by the demanding needs of current underground neutrino experiments; significant advances have been made on the ultra-trace detection of actinides. I focused on two techniques: negative-ion based Accelerator Mass Spectrometry and positive-ion based Resonance Ionization Mass Spectrometry.

AMS has been very rarely used to detect ultra low concentrations of primordial actinides. I investigated and developed an AMS method to detect traces of ^{238}U and ^{232}Th from electroformed ultrapure Cu samples. Starting with a molecular negative ion containing the desired species (e.g $^{238}UCu^{-}$), the injected negative ion beam is charge-exchanged to multiply-charged positive ions in the stripping gas channel of the terminal of an electrostatic tandem accelerator before the second stage of acceleration; consequently the molecule is destroyed and the actinide is further accelerated as an atomic ion in charge state +5. A time of flight system is used to identify and select the actinide atom-by-atom. While we were successful in detecting U and Th from the ultra-pure Cu matrix using AMS, further quantitative work would require the establishment of a reliable reference sample with a well defined concentration of U and Th.

It is well known that the overall detection efficiencies for actinides using AMS with a Cs-sputtering negative ion source are very low. We explore instead the possibility of obtaining higher efficiencies and equal or better sensitivity using an alternative laser-based method using positive ions. In the second part of this thesis I present my results using RIMS in actinides. I describe a procedure for the safe handling of Pu and for the preparation of

aliquots of the Pu sample to use in the resonant ionization laser ion source (RILIS) to investigate efficiency. I describe the development of new highly efficient resonance ionization schemes in Pu. With a Ti:sapphire laser system various 3-step excitation schemes were identified and compared with regard to the highest yield. Several autoionizing Rydberg series converging towards the first ionization potential (IP) were observed. Applying two methods to the spectra obtained, the series limit well as the ionization potential were precisely determined. The resulting new value of IP = 48605.748 $(95)_{\mathrm{stat}}$ $(49)_{\mathrm{sys}}$ cm^{-1} differs slightly from the NIST value of 48601(2) cm^{-1} and is significantly more accurate. High precision studies of the IP for heavy elements will serve to benchmark modern quantum and relativistic theories and provide insight into the chemical behavior of the heaviest elements (super heavy elements).

I have measured the overall efficiency of generating Th, U and Pu ion beams with the RILIS at ORNL. A high efficiency of about 32% for Th, 9% for U and 51% for Pu have been obtained using different three-step ionization schemes. I also investigated the sensitivity of RIMS at ORNL. I could observe the isotope ^{240}Pu in the ^{242}Pu sample, corresponding to a detection limit of 10^3 atoms.

To our knowledge, the detection limits obtained with RIMS for Pu are the lowest reported and the efficiency Pu, Th, and U isotopes are the highest reported for mass spectrometry analysis. This work demonstrated that RIMS fulfills the ultratrace detection demands. The studies on actinides presented here further probe and help understand capabilities of this versatile analytical technology.

The experiments described here were performed using the infrastructure and equipment of the former radioactive beam facility HRIBF at ORNL. The success of these studies could not have been done without the versatility and capabilities of the radioactive beam facility. These included the use of a hot laboratory that allowed the safe handling of Pu; the availability of the laser ion source that included the three compact tunable Ti:Sapphire lasers and the IRIS2 injector that serve as a high resolution mass spectrometer. The work done in this thesis demonstrated that the use of laser-based techniques with AMS technique constitute the most powerful techniques capable of addressing the most demanding needs of the current experiments trying to answer the big ideas in physics.

Bibliography

[1] Miroslav Iliaš, Vladimir Kelloe, and Miroslav Urban. Relativistic effects in atomic and molecular properties. *Acta Physica Slovaca. Reviews and Tutorials*, 60(3):259–391, 2010. xii, 13, 14

[2] Pavel Neogrády, Vladimir Kellö, Miroslav Urban, and Andrzej J Sadlej. Ionization potentials and electron affinities of cu, ag, and au: Electron correlation and relativistic effects. *International journal of quantum chemistry*, 63(2):557–565, 1997. xii, 14

[3] S. S. Hecker. The magic of plutonium: 5f electrons and phase instability. *Metallurgical and Materials Transactions A*, 35(8):2207–2222, Aug 2004. xii, 15

[4] Michael E Ketterer and Scott C Szechenyi. Determination of plutonium and other transuranic elements by inductively coupled plasma mass spectrometry: a historical perspective and new frontiers in the environmental sciences. *Spectrochimica Acta Part B: Atomic Spectroscopy*, 63(7):719–737, 2008. xii, 17

[5] Claudio Tuniz, Walter Kutschera, David Fink, Gregory F Herzog, and John R Bird. *Accelerator mass spectrometry: ultrasensitive analysis for global science*. CRC press, 1998. xiii, 24

[6] S Winkler. Accelerator mass spectrometry of heavy radionuclides with special focus on hf-182. *Canberra: The Australian National University*, 2007. xiii, 37

[7] Yuan Liu. Ornl developments in laser ion sources for radioactive ion beam production. *Hyperfine Interactions*, 227(1-3):85–99, 2014. xiv, 47, 49

[8] Sebastian Raeder, Amin Hakimi, Nils Stöbener, Norbert Trautmann, and Klaus Wendt. Detection of plutonium isotopes at lowest quantities using in-source resonance ionization mass spectrometry. *Analytical and bioanalytical chemistry*, 404(8):2163–2172, 2012. xvi, 61, 62, 67, 74, 75, 80

[9] K Wendt, T Gottwald, C Mattolat, and S Raeder. Ionization potentials of the lanthanides and actinides–towards atomic spectroscopy of super-heavy elements. *Hyperfine Interactions*, 227(1-3):55–67, 2014. xvii, 98

[10] A. Kramida, Yu. Ralchenko, J. Reader, and and NIST ASD Team. NIST Atomic Spectra Database (ver. 5.6.1), [Online]. Available: `https://physics.nist.gov/asd` [2019, September 15]. National Institute of Standards and Technology, Gaithersburg, MD., 2018. xviii, 103, 106

[11] N. Abgrall, A. Abramov, N. Abrosimov, et al. The large enriched germanium experiment for neutrinoless double beta decay (LEGEND). *AIP Conference Proceedings*, 1894(1):020027, 2017. 1

[12] Joachim Wolf, Katrin Collaboration, et al. The katrin neutrino mass experiment. *Nuclear Instruments and Methods in Physics Research Section A: Accelerators, Spectrometers, Detectors and Associated Equipment*, 623(1):442–444, 2010. 1, 7

[13] DN McKinsey, D Akerib, S Bedikian, A Bernstein, A Bolozdynya, A Bradley, J Chapman, K Clark, T Classen, A Curioni, et al. The lux dark matter search. *IOP Publishing*, 203(1):012026, 2010. 1

[14] Junaid Aasi, BP Abbott, Richard Abbott, Thomas Abbott, MR Abernathy, Kendall Ackley, Carl Adams, Thomas Adams, Paolo Addesso, RX Adhikari, et al. Advanced ligo. *Classical and quantum gravity*, 32(7):074001, 2015. 1

[15] N Abgrall, E Aguayo, FT Avignone, AS Barabash, FE Bertrand, M Boswell, V Brudanin, M Busch, AS Caldwell, Y-D Chan, et al. The majorana demonstrator neutrinoless double-beta decay experiment. *Advances in High Energy Physics*, 2014, 2014. 1, 2, 8, 9, 136

[16] K-H Ackermann, M Agostini, M Allardt, M Altmann, E Andreotti, AM Bakalyarov, M Balata, I Barabanov, M Barnabé Heider, N Barros, et al. The gerda experiment for the search of $0\nu\beta\beta$ decay in ^{76}Ge. *The European Physical Journal C*, 73(3):1–29, 2013. 1, 8

[17] G Alimonti, G Anghloher, C Arpesella, M Balata, G Bellini, J Benziger, S Bonetti, L Cadonati, FP Calaprice, G Cecchet, et al. Ultra-low background measurements in a large volume underground detector. *Astroparticle Physics*, 8(3):141–157, 1998. 1

[18] Rafael F Lang and Wolfgang Seidel. Search for dark matter with cresst. *New Journal of Physics*, 11(10):105017, 2009. 1

[19] M Laubenstein. Experimental techniques for low energy neutrino experiments. *Nuclear Physics B-Proceedings Supplements*, 100(1):39–41, 2001. 1

[20] K. H. Ackermann, M. Agostini, M. Allardt, et al. The GERDA experiment for the search of $0\nu\beta\beta$ decay in ^{76}Ge. *The European Physical Journal C*, 73(3):2330, Mar 2013. 2

[21] N. Abgrall, I. J. Arnquist, F. T. Avignone, III, et al. The MAJORANA DEMONSTRATOR radioassay program. *Nuclear Instruments and Methods in Physics Research Section A: Accelerators, Spectrometers, Detectors and Associated Equipment*, 828:22 – 36, 2016. 2

[22] B.D. LaFerriere, T.C. Maiti, I.J. Arnquist, and E.W. Hoppe. A novel assay method for the trace determination of th and u in copper and lead using inductively coupled plasma mass spectrometry. *Nuclear Instruments and Methods in Physics Research Section A: Accelerators, Spectrometers, Detectors and Associated Equipment*, 775:93 – 98, 2015. 2, 19

[23] L Keith Fifield. Accelerator mass spectrometry and its applications. *Reports on Progress in Physics*, 62(8):1223, 1999. 3, 18

[24] Andre De Gouvea. Neutrinos have mass—so what? *Modern Physics Letters A*, 19(38):2799–2813, 2004. 4

[25] Lester R Morss, Norman M Edelstein, Jean Fuger, and Joseph J Katz. *The chemistry of the actinide and transactinide elements*, volume 1-6. Springer, 2011. 4, 11

[26] MS Safronova, D Budker, D DeMille, Derek F Jackson Kimball, A Derevianko, and Charles W Clark. Search for new physics with atoms and molecules. *Reviews of Modern Physics*, 90(2):025008, 2018. 5

[27] Frederick Reines, CL Cowan Jr, FB Harrison, AD McGuire, and HW Kruse. Detection of the free antineutrino. *Physical Review*, 117(1):159, 1960. 6

[28] Raymond Davis Jr, Don S Harmer, and Kenneth C Hoffman. Search for neutrinos from the sun. *Physical Review Letters*, 20(21):1205, 1968. 6

[29] T Araki, K Eguchi, S Enomoto, K Furuno, K Ichimura, H Ikeda, K Inoue, K Ishihara, T Iwamoto, T Kawashima, et al. Measurement of neutrino oscillation with kamland: Evidence of spectral distortion. *Physical Review Letters*, 94(8):081801, 2005. 6

[30] MH Ahn, E Aliu, S Andringa, S Aoki, Y Aoyama, J Argyriades, K Asakura, R Ashie, F Berghaus, HG Berns, et al. Measurement of neutrino oscillation by the k2k experiment. *Physical Review D*, 74(7):072003, 2006. 6

[31] P Adamson, DJ Auty, DS Ayres, C Backhouse, G Barr, M Betancourt, M Bishai, A Blake, GJ Bock, DJ Boehnlein, et al. Improved search for muon-neutrino to electron-neutrino oscillations in minos. *Physical Review Letters*, 107(18):181802, 2011. 6

[32] D Akimov, JB Albert, P An, C Awe, PS Barbeau, B Becker, V Belov, A Brown, A Bolozdynya, B Cabrera-Palmer, et al. Observation of coherent elastic neutrino-nucleus scattering. *Science*, 357(6356):1123–1126, 2017. 6

[33] Juerg Beringer, JF Arguin, RM Barnett, K Copic, O Dahl, DE Groom, CJ Lin, J Lys, H Murayama, CG Wohl, et al. Review of particle physics. *Physical Review D-Particles, Fields, Gravitation and Cosmology*, 86(1):010001, 2012. 7

[34] Andrea Giuliani and Alfredo Poves. Neutrinoless double-beta decay. *Advances in High Energy Physics*, 2012, 2012. 7

[35] The 2015 nuclear science advisory committee. http://science.energy.gov/~/media/np/nsac/pdf/2015LRP/2015_LRPNS_091815.pdf. Accessed: 2016-11-24. 8

[36] P5 report 2014. http://science.energy.gov/~/media/hep/hepap/pdf/May-2014/FINAL_P5_Report_053014.pdf. Accessed: 2016-11-25. 8

[37] Next generation ^{76}ge meeting. https://apps.research.unc.edu/events/index.cfm?event=events.eventDetails&event_key=D14C85138B565C420C6CF290EF04B3DD3A1FA5C1. Accessed: 2016-11-25. 8

[38] J Detwiler. Demonstrator background calculations spreadsheet, 2010. 9

[39] Christoph E Düllmann. Studying chemical properties of the heaviest elements: One atom at a time. *Nuclear Physics News*, 27(2):14–20, 2017. 10

[40] J Michael Pearson. discovery of fission. *Physics Today*, 68(6):40, 2015. 10

[41] Paul J Karol, Robert C Barber, Bradley M Sherrill, Emanuele Vardaci, and Toshimitsu Yamazaki. Discovery of the elements with atomic numbers z= 113, 115 and 117 (iupac technical report). *Pure and Applied Chemistry*, 88(1-2):139–153, 2016. 10

[42] Paul J Karol, Robert C Barber, Bradley M Sherrill, Emanuele Vardaci, and Toshimitsu Yamazaki. Discovery of the element with atomic number z= 118 completing the 7th row of the periodic table (iupac technical report). *Pure and Applied Chemistry*, 88(1-2):155–160, 2016. 10

[43] D. W. Efurd, R. E. Steiner, F. R. Roensch, S. E. Glover, and J. A. Musgrave. Determination of the 240 pu/ 239 pu atom ratio in global fallout at two locations in the northern hemisphere. *Journal of Radioanalytical and Nuclear Chemistry*, 263(2):387–391, 2005. 11

[44] EP Hardy, PW Krey, and HL Volchok. Global inventory and distribution of fallout plutonium. *Nature*, 241(5390):444, 1973. 11

[45] S Bürger, SD Balsley, S Baumann, J Berger, SF Boulyga, JA Cunningham, S Kappel, A Koepf, and J Poths. Uranium and plutonium analysis of nuclear material samples by multi-collector thermal ionisation mass spectrometry: quality control, measurement uncertainty, and metrological traceability. *International Journal of Mass Spectrometry*, 311:40–50, 2012. 11

[46] Wenting Bu, Youyi Ni, Georg Steinhauser, Wang Zheng, Jian Zheng, and Naoki Furuta. The role of mass spectrometry in radioactive contamination assessment after the fukushima nuclear accident. *Journal of Analytical Atomic Spectrometry*, 33(4):519–546, 2018. 11

[47] J Chai, Y Miyamoto, Y Kokubu, M Magara, S Sakurai, S Usuda, Y Oura, and M Ebihara. An attempt for determining 235u/238u ratio for a trace amount of uranium: Search for an extinct radionuclide 247cm in the early solar system. *Journal of radioanalytical and nuclear chemistry*, 272(2):397–401, 2007. 11, 18

[48] Kenta Hotokezaka, Tsvi Piran, and Michael Paul. Short-lived 244 pu points to compact binary mergers as sites for heavy r-process nucleosynthesis. *Nature Physics*, 11(12):1042, 2015. 11, 16

[49] Anton Wallner, T Faestermann, J Feige, C Feldstein, K Knie, Gunther Korschinek, W Kutschera, A Ofan, M Paul, F Quinto, et al. Abundance of live 244 pu in deep-sea reservoirs on earth points to rarity of actinide nucleosynthesis. *Nature Communications*, 6:5956, 2015. 11, 16

[50] GR Hertel. Surface ionization. ii. the first ionization potential of uranium. *The Journal of Chemical Physics*, 47(1):335–336, 1967. 11

[51] David H Smith and GR Hertel. First ionization potentials of th, np, and pu by surface ionization. *The Journal of Chemical Physics*, 51(7):3105–3107, 1969. 11

[52] David H Smith. Mass spectrometric investigation of surface ionization. vii. the first ionization potential of curium. *The Journal of Chemical Physics*, 54(3):1424–1425, 1971. 11

[53] Earl F Worden and John G Conway. Laser spectroscopy of neptunium; first ionization potential, lifetimes and new high-lying energy levels of np i. *JOSA*, 69(5):733–738, 1979. 11

[54] Earl F Worden, Lee R Carlson, Steve A Johnson, Jeffrey A Paisner, and Richard W Solarz. Ionization potential of neutral atomic plutonium determined by laser spectroscopy. *JOSA B*, 10(11):1998–2005, 1993. 11, 104, 105

[55] N Erdmann, M Nunnemann, K Eberhardt, G Herrmann, G Huber, S Köhler, JV Kratz, G Passler, JR Peterson, N Trautmann, et al. Determination of the first ionization potential of nine actinide elements by resonance ionization mass spectroscopy (rims). *Journal of alloys and compounds*, 271:837–840, 1998. 11

[56] Glenn T Seaborg. The chemical and radioactive properties of the heavy elements. In *Modern Alchemy: Selected Papers of Glenn T Seaborg*, pages 20–23. World Scientific, 1945. 11

[57] Glenn T Seaborg. The transuranium elements. *Science*, 104(2704):379–386, 1946. 11

[58] T Vitova, I Pidchenko, D Fellhauer, PS Bagus, Y Joly, T Pruessmann, S Bahl, E Gonzalez-Robles, J Rothe, M Altmaier, et al. The role of the 5f valence orbitals of early actinides in chemical bonding. *Nature communications*, 8:16053, 2017. 11, 15

[59] JB Roberto, Charles W Alexander, Rose Ann Boll, JD Burns, JG Ezold, LK Felker, Susan L Hogle, and KP Rykaczewski. Actinide targets for the synthesis of super-heavy elements. *Nuclear Physics A*, 944:99–116, 2015. 11

[60] A Wallner, J Feige, N Kinoshita, M Paul, LK Fifield, R Golser, M Honda, U Linnemann, H Matsuzaki, S Merchel, et al. Recent near-earth supernovae probed by global deposition of interstellar radioactive 60 fe. *Nature*, 532(7597):69, 2016. 11

[61] Paul Adrien Maurice Dirac. The quantum theory of the electron. *Proceedings of the Royal Society of London. Series A, Containing Papers of a Mathematical and Physical Character*, 117(778):610–624, 1928. 12

[62] Sheldon Lee Glashow and Ben Bova. *Interactions: a journey through the mind of a particle physicist and the matter of this world*. Warner, 1988. 12

[63] Pekka Pyykko and Jean Paul Desclaux. Relativity and the periodic system of elements. *Accounts of Chemical Research*, 12(8):276–281, 1979. 12

[64] Roy Middleton. A negative ion cookbook. *University of Pennsylvania, unpublished*, 1989. 13, 26

[65] TK Sato, M Asai, A Borschevsky, T Stora, N Sato, Y Kaneya, K Tsukada, Ch E Düllmann, K Eberhardt, E Eliav, et al. Measurement of the first ionization potential of lawrencium, element 103. *Nature*, 520(7546):209, 2015. 13

[66] G. T. Seaborg, A. C. Wahl, and J. W. Kennedy. Radioactive element 94 from deuterons on uranium. *Phys. Rev.*, 69:367–367, Apr 1946. 14

[67] Glenn T Seaborg and Arthur C Wahl. The chemical properties of elements 94 and 93. *Journal of the American Chemical Society*, 70(3):1128–1134, 1948. 14

[68] Bo Bo Cunningham and Lo Bo Werner. The first isolation of plutonium. *Journal of the American Chemical Society*, 71(5):1521–1528, 1949. 14

[69] David Albright and Serena Kelleher-Vergantini. Military highly enriched uranium and plutonium stocks in acknowledged nuclear weapon states. *Institute for Science and International Security, Washington, DC*, 2015. 14

[70] Glatz Jean-Paul and Konings Rudy. Plutonium and other transuranium elements. *Ullmann's Encyclopedia of Industrial Chemistry*, 2012. 15

[71] C Grüning, G Huber, P Klopp, JV Kratz, P Kunz, G Passler, N Trautmann, A Waldek, and K Wendt. Resonance ionization mass spectrometry for ultratrace analysis of plutonium with a new solid state laser system. *International Journal of Mass Spectrometry*, 235(2):171–178, 2004. 15, 61

[72] MR Drout, AL Piro, BJ Shappee, CD Kilpatrick, JD Simon, C Contreras, DA Coulter, RJ Foley, MR Siebert, N Morrell, et al. Light curves of the neutron star merger gw170817/sss17a: Implications for r-process nucleosynthesis. *Science*, page eaaq0049, 2017. 16

[73] BJ Shappee, JD Simon, MR Drout, AL Piro, N Morrell, JL Prieto, D Kasen, TW-S Holoien, JA Kollmeier, DD Kelson, et al. Early spectra of the gravitational wave source gw170817: Evolution of a neutron star merger. *Science*, 358(6370):1574–1578, 2017. 16

[74] Stefan Bürger, Lee R Riciputi, Debra A Bostick, Steven Turgeon, Eddie H McBay, and Mark Lavelle. Isotope ratio analysis of actinides, fission products, and geolocators by high-efficiency multi-collector thermal ionization mass spectrometry. *International Journal of Mass Spectrometry*, 286(2-3):70–82, 2009. 18, 80

[75] Suresh K Aggarwal. Thermal ionisation mass spectrometry (tims) in nuclear science and technology–a review. *Analytical Methods*, 8(5):942–957, 2016. 18

[76] Liguo Cao, Wenting Bu, Jian Zheng, Shaoming Pan, Zhongtang Wang, and Shigeo Uchida. Plutonium determination in seawater by inductively coupled plasma mass spectrometry: A review. *Talanta*, 151:30–41, 2016. 18

[77] Wenting Bu, Jian Zheng, Michael E Ketterer, Sheng Hu, Shigeo Uchida, and Xiaolin Wang. Development and application of mass spectrometric techniques for ultra-trace determination of 236u in environmental samples-a review. *Analytica chimica acta*, 995:1–20, 2017. 18

[78] N Famulok, T Faestermann, L Fimiani, JM Gómez-Guzmán, K Hain, G Korschinek, P Ludwig, and S Schönert. Ultrasensitive detection method for primordial nuclides in copper with accelerator mass spectrometry. *Nuclear Instruments and Methods in Physics Research Section B: Beam Interactions with Materials and Atoms*, 2015. 18, 20, 30, 36

[79] M Laubenstein, M Hult, J Gasparro, D Arnold, S Neumaier, G Heusser, M Köhler, P Povinec, J-L Reyss, M Schwaiger, et al. Underground measurements of radioactivity. *Applied Radiation and Isotopes*, 61(2):167–172, 2004. 19

[80] S Pattberg and R Matschat. Determination of trace impurities in high purity copper using sector-field icp-ms: continuous nebulization, flow injection analysis and laser ablation. *Fresenius' journal of analytical chemistry*, 364(5):410–416, 1999. 19

[81] S Nisi, A Di Vacri, ML Di Vacri, A Stramenga, and M Laubenstein. Comparison of inductively coupled mass spectrometry and ultra low-level gamma-ray spectroscopy for ultra low background material selection. *Applied Radiation and Isotopes*, 67(5):828–832, 2009. 19

[82] Jan Verplancke. Low level gamma spectroscopy: low, lower, lowest. *Nuclear Instruments and Methods in Physics Research Section A: Accelerators, Spectrometers, Detectors and Associated Equipment*, 312(1):174 – 182, 1992. 19

[83] G. Heusser, M. Laubenstein, and H. Neder. Low-level germanium gamma-ray spectrometry at the μbq/kg level and future developments towards higher sensitivity. In P.P. Povinec and J.A. Sanchez-Cabeza, editors, *Radionuclides in the EnvironmentInt. Conf. On Isotopes in Env. Studies*, volume 8 of *Radioactivity in the Environment*, pages 495 – 510. Elsevier, 2006. 19

[84] A Marinov, I Rodushkin, D Kolb, A Pape, Y Kashiv, R Brandt, RV Gentry, and HW Miller. Evidence for the possible existence of a long-lived superheavy nucleus with atomic mass number a= 292 and atomic number z=122 in natural th. *International Journal of Modern Physics E*, 19(01):131–140, 2010. 20

[85] F. Deringer et al. Search for superheavy isotope with a=292 and neutron deficient th isotopes in natural thorianite. Poster presented at AMS 11 - Rome. 20

[86] M. Srncik, P. Steier, and G. Wallner. Depth profile of $^{236}U/^{238}U$ in soil samples in La Palma, Canary Islands. *Journal of Environmental Radioactivity*, 102(6):614–619, 2011. 20

[87] P. Steier, M. Bichler, L. K. Fifield, et al. Natural and anthropogenic ^{236}U in environmental samples. *Nuclear Instruments and Methods in Physics Research Section B: Beam Interactions with Materials and Atoms*, 266(10):2246 – 2250, 2008. 20

[88] M. A. C Hotchkis, D. Child, D. Fink, et al. Measurement of ^{236}U in environmental media. *Nuclear Instruments and Methods in Physics Research Section B: Beam Interactions with Materials and Atoms*, 172(1):659 – 665, 2000. 20

[89] X. Wang, S. Jiang, M. He, et al. ^{236}U measurement with accelerator mass spectrometry at CIAE. *Nuclear Instruments and Methods in Physics Research Section B: Beam Interactions with Materials and Atoms*, 268(13):2295 – 2299, 2010. 20

[90] A. Galindo-Uribarri, J. R. Beene, M. Danchev, et al. Pushing the limits of accelerator mass spectrometry. *Nuclear Instruments and Methods in Physics Research Section B: Beam Interactions with Materials and Atoms*, 259(1):123 – 130, 2007. 20

[91] M. S. Janzen, A. Galindo-Uribarri, Y. Liu, et al. The use of aluminum nitride to improve aluminum-26 accelerator mass spectrometry measurements and production of radioactive ion beams. *Nuclear Instruments and Methods in Physics Research Section B: Beam Interactions with Materials and Atoms*, 361:281 – 287, 2015. 20

[92] A. Galindo-Uribarri, C. C. Havener, T. L. Lewis, and Y. Liu. Selective isobar suppression for accelerator mass spectrometry and radioactive ion-beam science. *Nuclear Instruments and Methods in Physics Research Section B: Beam Interactions with Materials and Atoms*, 268(7):834 – 838, 2010. 20

[93] Y. Liu, J. C. Batchelder, A. Galindo-Uribarri, et al. Ion source development for ultratrace detection of uranium and thorium. *Nuclear Instruments and Methods in Physics Research Section B: Beam Interactions with Materials and Atoms*, 361:267 – 272, 2015. 20, 41

[94] Alfredo Galindo-Uribarri, James R Beene, M Danchev, J Doupe, B Fuentes, J Gomez Del Campo, PA Hausladen, Raymond C Juras, J Felix Liang, Albert E Litherland, et al. Pushing the limits of accelerator mass spectrometry. *Nuclear Instruments and Methods in Physics Research Section B: Beam Interactions with Materials and Atoms*, 259(1):123–130, 2007. 22

[95] Luis W Alvarez and Robert Cornog. He 3 in helium. *Physical Review*, 56(4):379, 1939. 22

[96] Luis W Alvarez. The early days of accelerator mass spectrometry. *Symposium on Accelerator Mass Spectrometry*, May 1981. 22

[97] HE Gove, KH Purser, and AE Litherland. Accelerator mass spectrometry (ams) 1977–1987. *Nuclear Instruments and Methods in Physics Research Section B: Beam Interactions with Materials and Atoms*, 268(7-8):xvii–xxii, 2010. 22

[98] AE Litherland. Ultrasensitive mass spectrometry with accelerators. *Annual Review of Nuclear and Particle Science*, 30(1):437–473, 1980. 23

[99] Walter Kutschera. Accelerator mass spectrometry: a versatile tool for research. *Nuclear Instruments and Methods in Physics Research Section B: Beam Interactions with Materials and Atoms*, 50(1-4):252–261, 1990. 23

[100] John S Vogel, Kenneth W Turteltaub, Robert Finkel, and D Erie Nelson. Accelerator mass spectrometry. *Analytical chemistry*, 67(11):353A–359A, 1995. 23

[101] L Keith Fifield. Accelerator mass spectrometry of long-lived heavy radionuclides. *Radioactivity in the Environment*, 11:263–293, 2008. 23

[102] Suresh Kumar Aggarwal. A review on the mass spectrometric studies of americium: Present status and future perspective. *Mass spectrometry reviews*, 37(1):43–56, 2018. 23

[103] R Middleton. A review of ion sources for accelerator mass spectrometry. *Nuclear Instruments and Methods in Physics Research Section B: Beam Interactions with Materials and Atoms*, 5(2):193–199, 1984. 26

[104] Meghan S Janzen, Alfredo Galindo-Uribarri, Yuan Liu, Gerald D Mills, Elisa Romero-Romero, and Daniel W Stracener. The use of aluminum nitride to improve aluminum-26 accelerator mass spectrometry measurements and production of radioactive ion

beams. *Nuclear Instruments and Methods in Physics Research Section B: Beam Interactions with Materials and Atoms*, 361:281–287, 2015. 26

[105] R Middleton and Charles T Adams. A close to universal negative ion source. *Nuclear Instruments and Methods*, 118(2):329–336, 1974. 26, 132

[106] R Middleton. A versatile high intensity negative ion source. *Nuclear Instruments and Methods in Physics Research*, 214(2-3):139–150, 1983. 26

[107] K.H Purser, A.E Litherland, and H.E Gove. Ultra-sensitive particle identification systems based upon electrostatic accelerators. *Nuclear Instruments and Methods*, 162(1):637–656, 1979. 26

[108] LK Fifield, RG Cresswell, ML Di Tada, TR Ophel, JP Day, AP Clacher, SJ King, and ND Priest. Accelerator mass spectrometry of plutonium isotopes. *Nuclear Instruments and Methods in Physics Research Section B: Beam Interactions with Materials and Atoms*, 117(3):295–303, 1996. 30

[109] LK Fifield, AP Clacher, K Morris, SJ King, RG Cresswell, JP Day, and FR Livens. Accelerator mass spectrometry of the planetary elements. *Nuclear Instruments and Methods in Physics Research Section B: Beam Interactions with Materials and Atoms*, 123(1):400–404, 1997. 30

[110] J.E McAninch, T.F Hamilton, T.A Brown, T.A Jokela, J.P Knezovich, T.J Ognibene, I.D Proctor, M.L Roberts, E Sideras-Haddad, J.R Southon, and J.S Vogel. Plutonium measurements by accelerator mass spectrometry at {LLNL}. *Nuclear Instruments and Methods in Physics Research Section B: Beam Interactions with Materials and Atoms*, 172(1–4):711 – 716, 2000. 8th International Conference on Accelerator Mass Spectrometry. 30

[111] Olivia J Marsden, Francis R Livens, J Philip Day, L Keith Fifield, and Phillip S Goodall. Determination of u-236 in sediment samples by accelerator mass spectrometry. *Analyst*, 126(5):633–636, 2001. 30

[112] Christof Vockenhuber, Irshad Ahmad, Robin Golser, Walter Kutschera, Vitaly Liechtenstein, Alfred Priller, Peter Steier, and Stephan Winkler. Accelerator mass spectrometry of heavy long-lived radionuclides. *International Journal of Mass Spectrometry*, 223–224:713 – 732, 2003. In Memoriam of Werner Lindinger. 30

[113] L.K. Fifield. Accelerator mass spectrometry of the actinides. *Quaternary Geochronology*, 3(3):276 – 290, 2008. Prospects for the New Frontiers of earth and Environmental Sciences. 30

[114] XL Zhao, MJ Nadeau, LR Kilius, and AE Litherland. The first detection of naturally-occurring 236 u with accelerator mass spectrometry. *Nuclear Instruments and Methods in Physics Research Section B: Beam Interactions with Materials and Atoms*, 92(1):249–253, 1994. 30

[115] Ran Chu. Experimental study on the production of negative ion copper clusters and applications. Master's thesis, University of Tennessee, Knoxville, 2016. 31, 132

[116] KS Grabowski, DL Knies, GK Hubler, and HA Enge. A new accelerator mass spectrometer for trace element analysis at the naval research laboratory. *Nuclear Instruments and Methods in Physics Research Section B: Beam Interactions with Materials and Atoms*, 123(1):566–570, 1997. 31

[117] PH Mao, T Kunihiro, KD McKeegan, CD Coath, G Jarzebinski, and DS Burnett. Preliminary evaluation of the secondary ion/accelerator mass spectrometer, megasims. In *36th Annual Lunar and Planetary Science Conference*, volume 36, page 2259, 2005. 31

[118] SH Sie, Th R Niklaus, and GF Suter. The australis microbeam ion source. *Nuclear Instruments and Methods in Physics Research Section B: Beam Interactions with Materials and Atoms*, 123(1):558–565, 1997. 31

[119] RM Ender, M Döbeli, M Suter, and H-A Synal. Accelerator sims at psi/eth zurich. *Nuclear Instruments and Methods in Physics Research Section B: Beam Interactions with Materials and Atoms*, 123(1):575–578, 1997. 31

[120] Graham C Wilson, Linas R Kilius, John C Rucklidge, Gang-Jian Ding, and Xiao-Lei Zhao. Trace-element analysis of mineral grains using accelerator mass spectrometry—from sampling to interpretation. *Nuclear Instruments and Methods in Physics Research Section B: Beam Interactions with Materials and Atoms*, 123(1):579–582, 1997. 31

[121] SH Sie, Th R Niklaus, and GFnbsp Suter. Microbeam ams: prospects of new geological applications. *Nuclear Instruments and Methods in Physics Research Section B: Beam Interactions with Materials and Atoms*, 123(1):112–121, 1997. 31

[122] FD McDaniel, JM Anthony, SN Renfrow, YD Kim, SA Datar, and S Matteson. Depth profiling analysis of semiconductor materials by accelerator mass spectrometry. *Nuclear Instruments and Methods in Physics Research Section B: Beam Interactions with Materials and Atoms*, 99(1):537–540, 1995. 31

[123] SPHT Freeman, C Bronk Ramsey, and REM Hedges. Imaging ams. *Nuclear Instruments and Methods in Physics Research Section B: Beam Interactions with Materials and Atoms*, 92(1-4):231–236, 1994. 31

[124] A.M. Zebelman, W.G. Meyer, K. Halbach, A.M. Poskanzer, R.G. Sextro, G. Gabor, and D.A. Landis. A time-zero detector utilizing isochronous transport of secondary electrons. *Nuclear Instruments and Methods*, 141(3):439 – 447, 1977. 35

[125] Joseph Ladislas Wiza. Microchannel plate detectors. *Nuclear Instruments and Methods*, 162(1):587–601, 1979. 35

[126] L.K. Fifield, S.G. Tims, J.O. Stone, D.C. Argento, and M. De Cesare. Ultra-sensitive measurements of 36cl and 236u at the australian national university. *Nuclear Instruments and Methods in Physics Research Section B: Beam Interactions with Materials and Atoms*, 294:126 – 131, 2013. Proceedings of the Twelfth International Conference on Accelerator Mass Spectrometry, Wellington, New Zealand, 20-25 March 2011. 35

[127] William R. Leo. *Techniques for nuclear and particle physics experiments*. Springer-Verlag Berlin Heidelberg, 1987. 35

[128] R. V. Ambartzumian and V. S. Letokhov. Selective two-step (STS) photoionization of atoms and photodissociation of molecules by laser radiation. *Appl. Opt.*, 11(2):354–358, Feb 1972. 41, 43

[129] H. J. Kluge, B. A. Bushaw, G. Passler, et al. Resonance ionization spectroscopy for trace analysis and fundamental research. *Fresenius' journal of analytical chemistry*, 350(4):323–329, 1994. 41

[130] David M Lubman. *Lasers and mass spectrometry*, volume 1. Oxford University Press, 1990. 41

[131] Vladilen Letokhov. *Laser photoionization spectroscopy*. Elsevier, 2012. 41, 43

[132] JP Young, RW Shaw, and DH Smith. Resonance ionization mass spectrometry. *Analytical Chemistry*, 61(22):1271A–1279A, 1989. 41

[133] MG Payne, Lu Deng, and N Thonnard. Applications of resonance ionization mass spectrometry. *Review of scientific instruments*, 65(8):2433–2459, 1994. 41, 42

[134] J.D. Fassett, L.J. Moore, J.C. Travis, and J.R. DeVoe. Laser resonance ionization mass spectrometry. *Science*, 230:262, 1985. 42

[135] Yuki Higuchi, Kenichi Watanabe, Takuya Hasegawa, Hideki Tomita, Jun Kawarabayashi, and Tetsuo Iguchi. Resonance ionization mass spectrometry using inductively coupled plasma as an atom source. *Journal of Nuclear Science and Technology*, 45(sup6):93–96, 2008. 42

[136] Valentin Fedosseev, Katerina Chrysalidis, Thomas Day Goodacre, Bruce Marsh, Sebastian Rothe, Christoph Seiffert, and Klaus Wendt. Ion beam production and study of radioactive isotopes with the laser ion source at isolde. *Journal of Physics G: Nuclear and Particle Physics*, 44(8):084006, 2017. 42, 46

[137] Y. Liu, T. Gottwald, C. C. Havener, J. Y. Howe, J. Kiggans, C. Mattolat, C. R. Vane, K. Wendt, and J. R. Beene. Laser ion source development at holifield radioactive ion beam facility. *Review of Scientific Instruments*, 83(2), 2012. 43

[138] James R Beene, Darryl T Dowling, Carl J Gross, Raymond C Juras, Yuan Liu, Martha J Meigs, Anthony J Mendez, Witold Nazarewicz, John William Sinclair, Daniel W Stracener, et al. Radioactive ion beam production capabilities at the holifield radioactive ion beam facility. *AIP Conference Proceedings*, 1336(1):576–580, 2011. 43

[139] James R Beene, Daniel W Bardayan, A Galindo Uribarri, Carl J Gross, KL Jones, J Felix Liang, Witold Nazarewicz, Daniel W Stracener, B Alan Tatum, and RL Varner. Isol science at the holifield radioactive ion beam facility. *Journal of Physics G: Nuclear and Particle Physics*, 38(2):024002, 2011. 43

[140] Marc Huyse. Ionization in a hot cavity. *Nuclear Instruments and Methods in Physics Research*, 215(1-2):1–5, 1983. 46

[141] F Schwellnus, R Catherall, B Crepieux, VN Fedosseev, BA Marsh, Ch Mattolat, M Menna, FK Österdahl, S Raeder, T Stora, et al. Study of low work function materials for hot cavity resonance ionization laser ion sources. *Nuclear Instruments and Methods in Physics Research Section B: Beam Interactions with Materials and Atoms*, 267(10):1856–1861, 2009. 46

[142] Yuan Liu and Daniel W Stracener. A resonant ionization laser ion source at ornl. *Nuclear Instruments and Methods in Physics Research Section B: Beam Interactions with Materials and Atoms*, 376:68–72, 2016. 47

[143] Y. Liu, C. U. Jost, A. J. Mendez, II, et al. On-line commissioning of the HRIBF resonant ionization laser ion source. *Nuclear Instruments and Methods in Physics Research Section B: Beam Interactions with Materials and Atoms*, 298:5 – 12, 2013. 48

[144] W Demtröder. Laser spectroscopy : basic concepts and instrumentation, 1996. 69

[145] ML Citron, HR Gray, CW Gabel, and CR Stroud Jr. Experimental study of power broadening in a two-level atom. *Physical Review A*, 16(4):1507, 1977. 69

[146] NV Vitanov, BW Shore, L Yatsenko, K Böhmer, T Halfmann, T Rickes, and K Bergmann. Power broadening revisited: theory and experiment. *Optics communications*, 199(1-4):117–126, 2001. 69

[147] Ruben de Groote. *Modeling and simulation of two-step resonance ionization processes using CW and pulsed lasers*. PhD thesis, Leuven U. 69

[148] R Kirchner. Progress in ion source development for on-line separators. *Nuclear Instruments and Methods in Physics Research*, 186(1-2):275–293, 1981. 74

[149] HL Ravn. Status and future development of ion sources for on-line mass separators. *Nuclear Instruments and Methods in Physics Research Section B: Beam Interactions with Materials and Atoms*, 70(1):107–117, 1992. 74

[150] R Kirchner. Ion sources for radioactive beams and related problems (review). *Review of scientific instruments*, 67(3):928–933, 1996. 74

[151] R Kirchner. Review of isol target–ion-source systems. *Nuclear Instruments and Methods in Physics Research Section B: Beam Interactions with Materials and Atoms*, 204:179–190, 2003. 74

[152] Yixiang Duan, Edwin P Chamberlin, and JoséA Olivares. Development of a new high-efficiency thermal ionization source for mass spectrometry. *International journal of mass spectrometry and ion processes*, 161(1-3):27–39, 1997. 74

[153] Yixiang Duan, Ray E Danen, Xiaomei Yan, Robert Steiner, Juan Cuadrado, David Wayne, Vahid Majidi, and José A Olivares. Characterization of an improved thermal ionization cavity source for mass spectrometry. *Journal of the American Society for Mass Spectrometry*, 10(10):1008–1015, 1999. 74

[154] David M Wayne, Wei Hang, Diane K McDaniel, Robert E Fields, Eddie Rios, and Vahid Majidi. The thermal ionization cavity (tic) source: elucidation of possible mechanisms for enhanced ionization efficiency. *International Journal of Mass Spectrometry*, 216(1):41–57, 2002. 74

[155] S Bürger, LR Riciputi, S Turgeon, D Bostick, E McBay, and M Lavelle. A high efficiency cavity ion source using tims for nuclear forensic analysis. *Journal of Alloys and Compounds*, 444:660–662, 2007. 74

[156] Zhai Li-hua, Deng Hu, Wei Guan-yi, Li Zhi-ming, Wang Chang-hai, Li Xue-song, Zhou Guo-qing, Su Yong-yang, and Zhang Zi-bin. A new, ohmic-heating based thermal ionization cavity source for mass spectrometry. *International Journal of Mass Spectrometry*, 305(1):45–49, 2011. 74

[157] S. Raeder, S. Fies, T. Gottwald, C. Mattolat, S. Rothe, and K. Wendt. In-source resonance ionization spectroscopy of high lying energy levels in atomic uranium. *Hyperfine Interactions*, 196(1):71–79, Feb 2010. 74, 77

[158] S. Raeder. Spurenanalyse von aktiniden in der umwelt mittels resonanzionisations-massenspektrometrie. *Doktorarbeit, Institut für Physik, Johannes Gutenberg Universität Mainz*, 2010. 74

[159] S. Raeder, V. Sonnenschein, T. Gottwald, et al. Resonance ionization spectroscopy of thorium isotopes–towards a laser spectroscopic identification of the low-lying 7.6 ev isomer of ^{229}Th. *Journal of Physics B: Atomic, Molecular and Optical Physics*, 44(16):165005, 2011. 74, 77

[160] Amin Hakimi, Thomas Fischbach, Sebastian Raeder, Norbert Trautmann, and Klaus Wendt. High resolution-resonance ionization spectroscopy on uranium. *Hyperfine Interactions*, 216(1-3):59–64, 2013. 74, 77

[161] GS Hurst, Munir H Nayfeh, and JP Young. A demonstration of one-atom detection. *Applied Physics Letters*, 30(5):229–231, 1977. 80

[162] N Trautmann, G Passler, and KDA Wendt. Ultratrace analysis and isotope ratio measurements of long-lived radioisotopes by resonance ionization mass spectrometry (rims). *Analytical and bioanalytical chemistry*, 378(2):348–355, 2004. 80

[163] Pascal Schönberg, Christoph Mokry, Jörg Runke, Daniela Schönenbach, Nils Stöbener, Petra Thörle-Pospiech, Norbert Trautmann, and Tobias Reich. Application

of resonance ionization mass spectrometry for ultratrace analysis of technetium. *Analytical chemistry*, 89(17):9077–9082, 2017. 80

[164] George Downing Liveing and James Dewar. On the spectra of sodium and potassium. *Proceedings of the Royal Society of London*, 29:398–402, 1879. 90, 91

[165] Walter Noël Hartley. Lvi.—on homologous spectra. *Journal of the Chemical Society, Transactions*, 43:390–400, 1883. 90

[166] ARP Rau and Mitio Inokuti. The quantum defect: Early history and recent developments. *American Journal of Physics*, 65(3):221–225, 1997. 93

[167] Gordon WF Drake and RA Swainson. Quantum defects and the 1/n dependence of rydberg energies: Second-order polarization effects. *Physical Review A*, 44(9):5448, 1991. 93

[168] Thomas F Gallagher. *Rydberg atoms*, volume 3. Cambridge University Press, 2005. 93

[169] Anthony F Starace. The quantum defect theory approach. In *Photoionization and other probes of many-electron interactions*, pages 395–406. Springer, 1976. 93

[170] Pekka Pyykko. Relativistic effects in structural chemistry. *Chemical Reviews*, 88(3):563–594, 1988. 94

[171] Sebastian Rothe. *An all-solid state laser system for the laser ion source RILIS and in-source laser spectroscopy of astatine at ISOLDE, CERN*. PhD thesis, Mainz U., Inst. Kernphys., 2012. 96

[172] S Köhler, R Deiβenberger, K Eberhardt, N Erdmann, G Herrmann, G Huber, JV Kratz, M Nunnemann, G Passler, PM Rao, et al. Determination of the first ionization potential of actinide elements by resonance ionization mass spectroscopy. *Spectrochimica Acta Part B: Atomic Spectroscopy*, 52(6):717–726, 1997. 103, 105

[173] Wayne K Stuckey and Robert W Kiser. Doubly charged negative ions of oxygen, fluorine, chlorine and bromine. *Nature Publishing Group*, 1966. 136

[174] Robert W. Kiser. *Instrumental Inorganic Chemistry*, chapter Doubly-charged negative ions in the gas phase, pages 89–158. Springer Berlin Heidelberg, Berlin, Heidelberg, 1979. 136

[175] H. Baumann, E. Heinicke, H.J. Kaiser, and K. Bethge. On the existence of doubly negative charged heavy ions. *Nuclear Instruments and Methods*, 95(2):389 – 391, 1971. 136

[176] David Spence, W. A. Chupka, and C. M. Stevens. Search for long-lived doubly charged atomic negative ions. *Phys. Rev. A*, 26:654–657, Jul 1982. 136

[177] K. H. Chang, R. D. McKeown, R. G. Milner, and J. Labrenz. Search for long-lived doubly charged negative atomic ions. *Phys. Rev. A*, 35:3949–3951, May 1987. 136

[178] L. Frees, E. Heinicke, and W.S. Koski. Concerning doubly charged negative ions of iodine in the gas phase. *Nuclear Instruments and Methods*, 159(1):105 – 107, 1979. 136

[179] J Ashenfelter, B Balantekin, HR Band, G Barclay, CD Bass, D Berish, NS Bowden, A Bowes, CD Bryan, JP Brodsky, et al. The prospect physics program. *arXiv preprint arXiv:1512.02202*, 2015. 140

Appendices

Appendix A

Cluster Formations

During the characterization of the ultrapure Cu we studied the production and formation of Cu clusters in the Cs-sputtering source. In 1973 Middleton and Adams [105] developed a universal Cs sputtering ion source that is nowadays the workhorse of most of the AMS laboratories. However there are still aspects of the sputtering process and the formation of negative ions (atoms, molecules and clusters) that are not fully understood. In this work we present experimental observation of the cluster formations and it relation with the sputtering process .

This test was performed at Oak Ridge National Laboratory (ORNL) using the low energy section of the 25 MV tandem AMS setup (Figure A.1) and in the Center for Isotopic Research on Cultural and Environmental Heritage (CIRCE) in Italy using the 3 MV tandem accelerator Figure A.2. The detailed results and analysis of production and formation of Cu clusters are reported in [115], they can be summarized as follows:

- Even-odd alternation in the cluster intensities, where the intensity of odd-n cluster was greater than that of even-n
- Magic numbers, manifest as discontinuities on the intensity pattern
- Binomial distribution based on the natural isotopic abundance
- Sputtering yield power law
- Cluster yield dependence with the Cs-sputtering energy

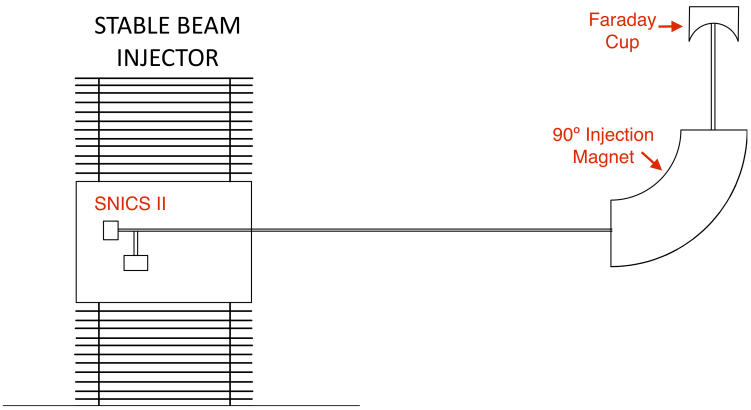


Figure A.1: Low energy setup from the 25 MV Tandem accelerator at ORNL. Consists of the Cs-sputter ion source SNICS II located in the stable injector, a high resolution magnet and a faraday cup.

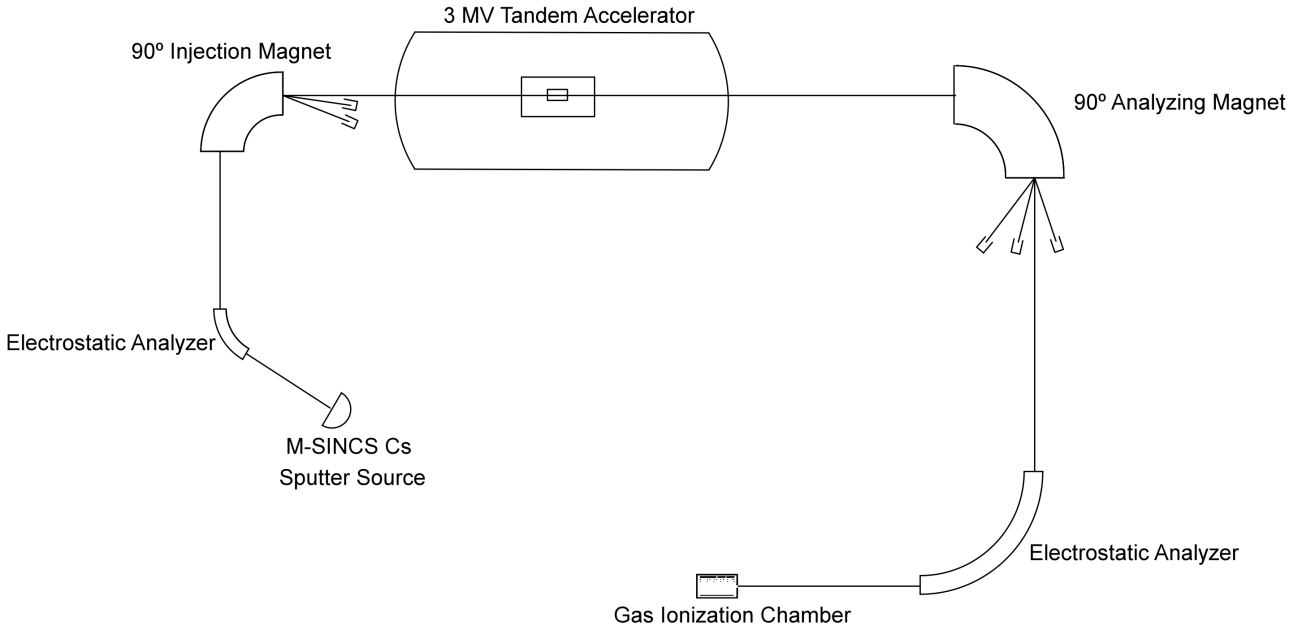
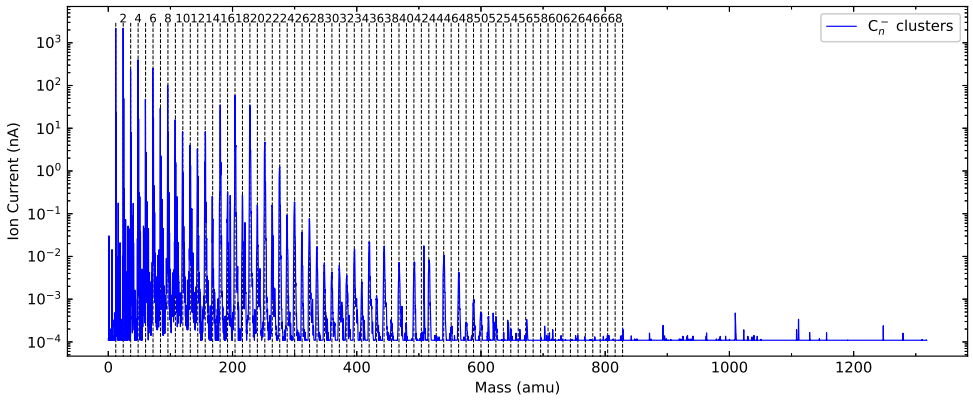


Figure A.2: Schematic diagram showing the main components of the AMS setup at CIRCE.

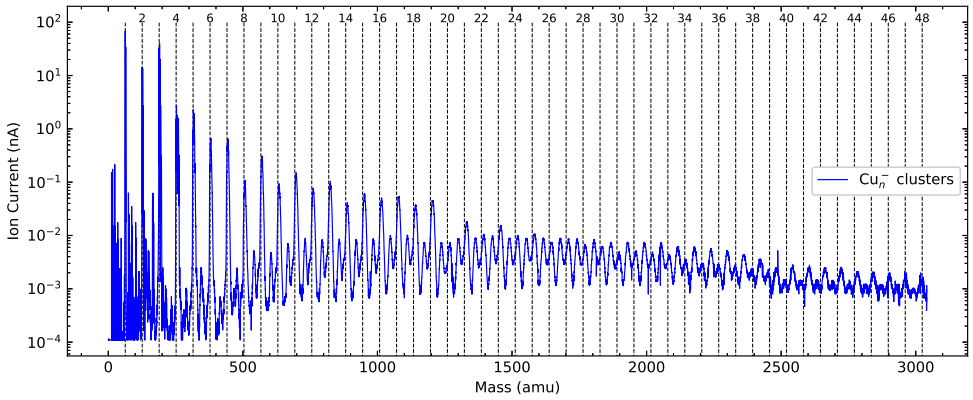
The study of the Cu clusters motivated to study clusters behavior for a lighter and heavier atomic number, we analyzed C and Au. We performed mass scans up to mass 3000 amu for Cu, 3500 amu for Au and 1300 amu for C showed in Figure A.3. In the case of C we stopped seeing clusters formation around mass 800 amu. We observed that C and Au present even-odd intensity effects like previously observed in Cu clusters, odd numbers presenting higher yield that the even numbers. In the three cases there were formation of other series of clusters with other elements. The C spectra shows a series of either ^{12}C + H or the series of the isotope ^{13}C, while the Cu spectra shows the series $^{63}Cu_n$ + O_2. The intensity of the $^{63}Cu_nO^2$ peaks varied strongly from sample to sample and also depended on the source operation parameters. The Au spectra showed the series $^{197}Au_n$+^{63}Cu. There was an odd -even effect in the series $^{197}Au_n{}^{63}$, the odd clusters being much less intense than the even clusters, from cluster n=5 there were no peaks visible for this series.

A Discussion

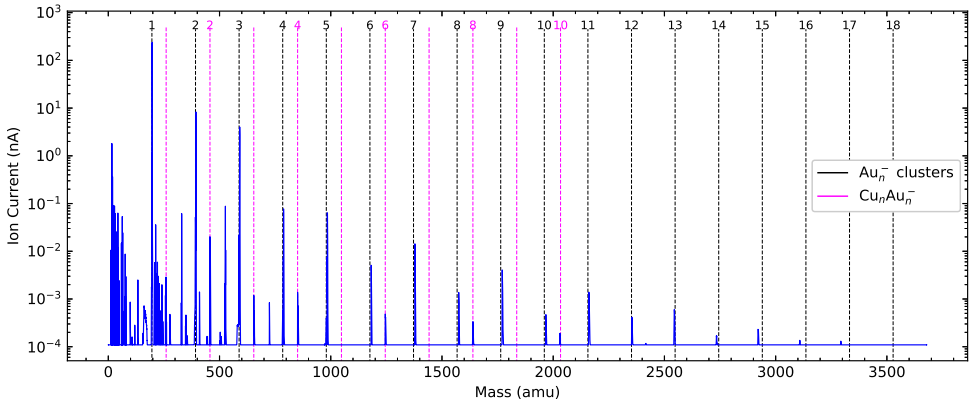
The measurements is this work gave us an insight of the type of contamination that can be produced in the low energy part of the AMS system. As explained in Chapter 5, Th and U are often extracted as negatively charged oxide from the Cs-sputtering ion source, however these studies demonstrated that the $^{63}Cu_nO^2$ cluster formation were not stable and depended on the sample and conditions of the ion source. Furthermore, we observed that the Cu cathode wheel can create contamination as well since for Au we observed $^{197}Au^{63}_nCu$ cluster formations. Therefore using a Cu wheel for U and Th in ultrapure Cu ultratrace detection is not recommended.



(a)



(b)



(c)

Figure A.3: Spectra of C, Cu and Au using a Cs-sputtering ion at 8 kV pre-acceleration voltage and accelerated at an energy of 100, 40 and 35 keV respectively. In all three spectra is observed cluster formations. Carbon and gold show the same odd-even pattern found for Cu clusters. The spectra of Au presents another series belonging to $^{197}Au_n$+^{63}Cu, however the peaks are only observed in even numbers of n.

Appendix B

Search for Doubly Charged Negative Atomic Ions

For many decades there has been controversial claims of the observation of doubly charged negative atomic ions mostly in light mass elements [173, 174, 175]. There have been attempts to reproduce those results without success [176, 177, 178].

The lifetimes of gaseous doubly-charged negative ions in their ground state are expected to be short and have been predicted to be of the order of 0.1 ns or less, however in excited states they can have long lifetimes of approximately 0.1 ms [174]. It was suggested that the probability of production of the doubly-charged species increases with the mass of the element [175].

In this study, we explored the feasibility of forming doubly-charged negative atomic ions with Cu because:

- Cu has relatively large electron affinity E.A. = 1.228 eV. It can form negative ions easily.
- Cu has an intermediate atomic number of Z=29, A=63. Increase the probability of observation.
- Cu samples can be produced extremely pure [15].
- Cu has an odd mass number. The signature of a possible doubly charged would be a non integer half mass.

We performed an experiment with the low energy setup of the 25 MV Tandem at the ORNL. Measuring the mass spectra of various Cu samples, we obtained suggestive evidence of doubly charged negative atomic Cu ions, Figure B.1. In order to verify that these peaks correspond to Cu we used a sample material isotopically enriched ^{63}Cu and ^{65}Cu. In the mass spectrum of ^{65}Cu sample, the ion peak at 31.5 amu, the exact half mass of ^{63}Cu, disappeared. Similar results have been observed with the ^{63}Cu sample. This result could mean that the mid-mass peaks are :

1. Doubly charged negative atomic ions
2. The break up of the singly charged negative Cu dimers before the injection magnet.

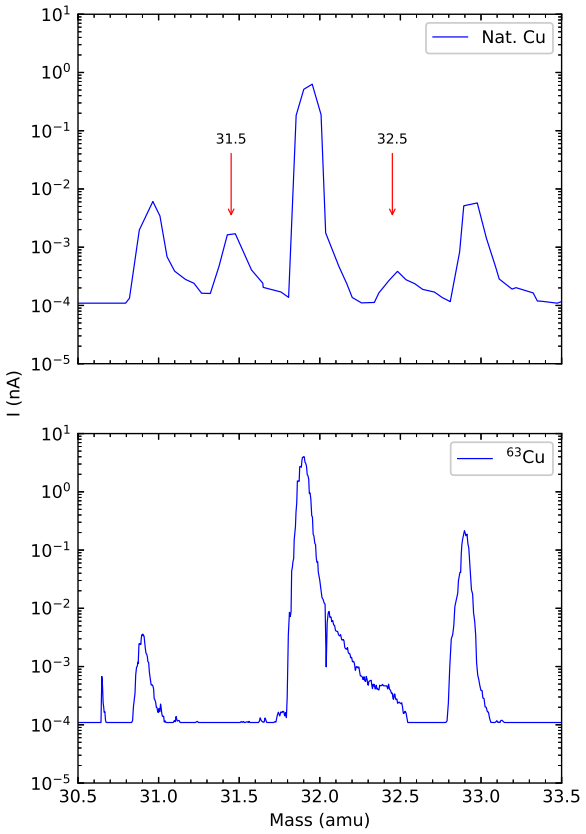


Figure B.1: Comparison between the spectra of the natural Cu (above) and the spectra of enriched ^{65}Cu (below). The peak at 31.5 mass disappears in the spectra of enriched ^{65}Cu.

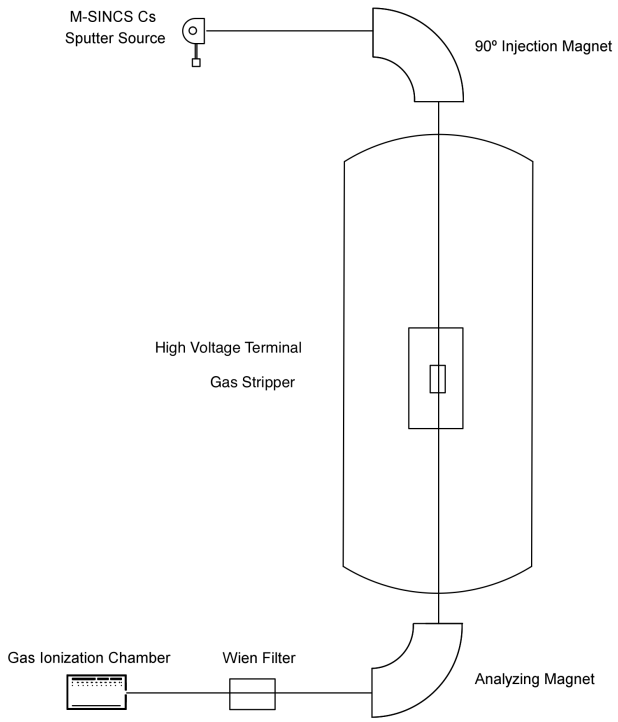


Figure B.2: Schematic diagram of the experimental setup for AMS at the ANU.

For a conclusive test we used AMS. The experiment was held at the Australian National University (ANU). We used the 14 UD pelletron Figure B.2. We assumed that the doubly charged negative atomic ions exist and we tuned the machine to inject them. We did not observed evidence of doubly charged Cu atomic negative ions. We observed the second possibility of the origin of these peaks, that they come from the breakup of the Cu dimers $^{63}Cu_2$,$^{65}Cu_2$ and $^{63}Cu^{65}Cu$.

From this experiment we can conclude:

- AMS technique enabled us to determine the identity of the Cu ion peaks at half masses of 31.5 amu and 32.5 amu.
- They do not correspond to the doubly charged negative Cu atomic ions but to the breakup products of singly charged negative Cu dimers before the injection magnet.
- We will continue the search for doubly charged negative ions. We propose the elements of the Figure B.3.

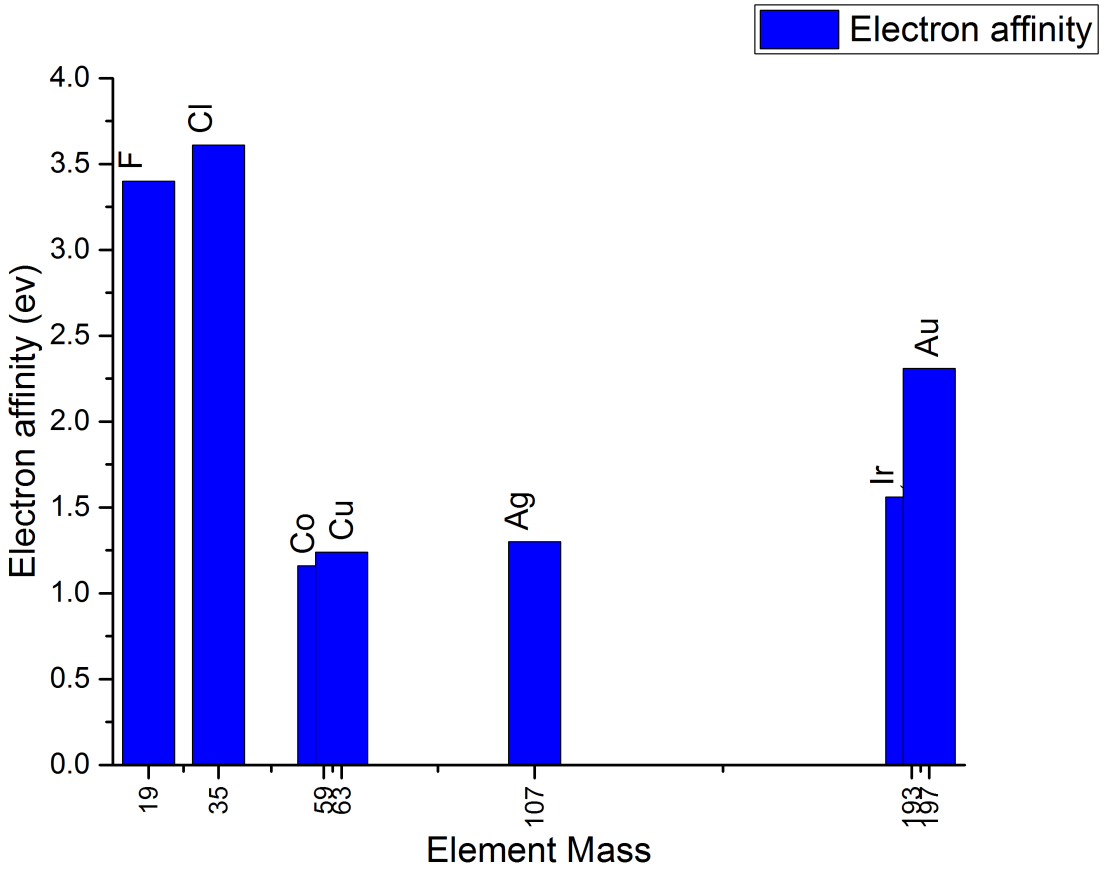


Figure B.3: Candidate elements for the search of doubly charged negative ions.

Appendix C

PROSPECT

The PROSPECT (Precision Reactor Oscillation and Spectrum) experiment utilizes the Inverse Beta Decay (IBD) reaction $\overline{\nu}_e + p \longrightarrow e^+ + n$ to make a precise measurement of the antineutrino spectrum from the highly-enriched uranium High Flux Isotope Reactor (HFIR) located at ORNL and to probe eV-scale sterile neutrinos by searching for neutrino oscillations over meter-long distances [179]. Interactions will take place in and around the experiment's segmented ^{6}Li-doped liquid scintillator detectors, producing a pair of triggers correlated in space and time. The proposed layout of the two-phase experiment is shown in Figure C.1.

Over the past few years several neutrino experiments at nuclear reactors have detected fewer antineutrinos than scientists had predicted, and the energy of the neutrinos did not match expectations. This, in combination with earlier anomalous results, led to the hypothesis that a fraction of electron antineutrinos may transform into sterile neutrinos that would have remained undetected in previous experiments. This hypothesized transformation would take place through a quantum mechanical process called neutrino oscillation. The first observation of neutrino oscillation amongst known types of neutrinos from the sun and the atmosphere led to the 2015 Nobel Prize in physics.

The development and construction of PROSPECT has been a significant team effort, the installation of PROSPECT followed four years of intensive research and development. PROSPECT was built in 16 months by the PROSPECT collaboration of more than 65 participants from 10 universities and 4 national laboratories, including 17 participants

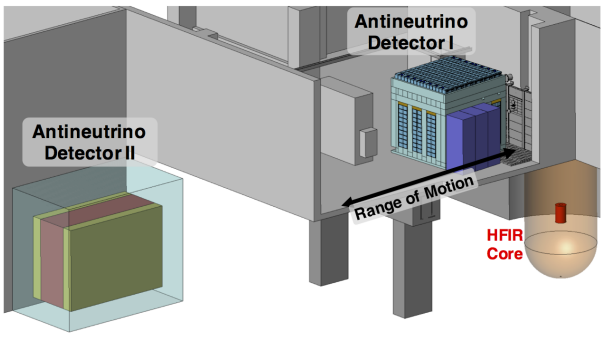


Figure C.1: Layout of the PROSPECT experiment. Shown are the HFIR reactor core and the two antineutrino detectors, AD-I and AD-II.

representing ORNL. I was involved in detector characterization, detector assembly and testing, radiation background studies, liquid scintillator optical characterization. Since March 2018 PROSPECT started data taking. With a surface-based, segmented detector, PROSPECT has produced the highest statistics measurement of ^{235}U $\bar{\nu}_e^-$ spectrum to date and with 33 days of data has disfavored sterile neutrino hypothesis in reactor sector at 2.2σ. PROSPECT has paved the way for surface-based neutrino detection capabilities. Initial results from PROSPECT have demonstrated the ability to detect 100s of antineutrino events per day with good signal-to-background in this above ground location and perform precise measurements of the HFIR antineutrino energy spectrum. Other similar research efforts are taking place worldwide with PROSPECT considered as the leading experiment.

Appendix D

Level Schemes

Table D.1: $E_2 = 35568.888\ cm^{-1}$

Peak #	λ_3	σ (λ_3)	FWHM (λ_3)	Avg I (nA)	E_{tot}	σ (E_{tot})
1	13028.9	0.006	0.987	0.038	48597.738	0.008
2	13035.3	0.038	0.916	0.016	48604.188	0.060
3	13042.6	0.013	0.405	0.018	48611.488	0.049
4	13050.8	0.015	0.213	0.017	48619.688	0.049
5	13058.3	0.456	3.523	0.020	48627.138	0.458
6	13064.4	0.010	0.458	0.023	48633.238	0.048
7	13068.9	0.024	3.122	0.026	48637.788	0.053
8	13097.0	0.003	0.355	0.036	48665.838	0.047
10	13122.7	0.116	4.416	0.026	48691.588	0.125
11	13135.5	0.037	0.891	0.018	48704.338	0.060
12	13142.3	0.078	2.615	0.071	48711.188	0.091
13	13165.6	0.009	0.489	0.055	48734.438	0.048
14	13171.4	0.016	0.519	0.041	48740.288	0.050
15	13176.6	0.014	2.296	0.076	48745.438	0.049
16	13183.5	0.028	1.338	0.057	48752.388	0.054
17	13196.7	0.011	0.349	0.044	48765.588	0.048
18	13222.7	0.002	0.340	0.113	48791.538	0.047

Table D.1. Continued

Peak #	λ_3	σ (λ_3)	FWHM (λ_3)	Avg I (nA)	E_{tot}	σ (E_{tot})
19	13232.2	0.015	0.951	0.038	48801.038	0.049
20	13236.7	0.022	0.665	0.029	48805.538	0.052
21	13248.1	0.025	4.098	0.052	48816.955	0.053
22	13260.4	0.013	1.064	0.044	48829.288	0.049
23	13283.8	0.026	3.769	0.056	48852.721	0.054
24	13293.3	0.013	0.806	0.053	48862.188	0.049
25	13302.6	0.003	0.286	0.092	48871.521	0.047
26	13305.4	0.015	1.734	0.060	48874.288	0.049
27	13310.6	0.030	1.732	0.034	48879.455	0.056
28	13329.1	0.003	0.337	0.100	48897.988	0.047
29	13337.0	0.007	1.148	0.085	48905.921	0.047
30	13339.4	0.009	0.342	0.054	48908.238	0.048
31	13354.7	0.007	0.449	0.091	48923.588	0.047
32	13370.9	0.008	0.673	0.059	48939.788	0.048

Table D.2: $E_2 = 35790.806\ cm^{-1}$

Peak #	λ_3	σ (λ_3)	FWHM (λ_3)	Avg I (nA)	E_{tot}	σ (E_{tot})
1	12448.3	0.002	0.325	0.253	48239.106	0.005
2	12455.6	0.003	0.267	0.170	48246.406	0.006
3	12457.5	0.005	0.254	0.141	48248.306	0.007
4	12463.6	0.009	0.182	0.105	48254.406	0.010
5	12470.6	0.007	0.212	0.123	48261.356	0.008
6	12471.7	0.004	0.232	0.140	48262.506	0.007
7	12472.7	0.013	0.243	0.142	48263.506	0.014
8	12477.6	0.007	0.185	0.114	48268.406	0.009
9	12486.6	0.008	0.205	0.111	48277.406	0.010
10	12507.7	0.021	0.275	0.101	48298.506	0.021
11	12513.0	0.008	0.208	0.111	48303.806	0.009
12	12515.4	0.014	0.141	0.133	48306.206	0.014
13	12518.1	0.014	0.197	0.135	48308.906	0.015
14	12522.7	0.007	0.193	0.116	48313.456	0.009
15	12525.3	0.009	0.199	0.111	48316.106	0.010
16	12531.1	0.005	0.244	0.139	48321.906	0.007
17	12532.3	0.005	0.243	0.142	48323.056	0.007
18	12543.4	0.005	0.225	0.139	48334.206	0.007
19	12547.6	0.023	0.395	0.098	48338.406	0.023
20	12555.2	0.009	0.304	0.119	48345.956	0.010
21	12566.3	0.008	0.178	0.110	48357.056	0.010
22	12570.1	0.027	0.223	0.058	48360.906	0.027
23	12570.9	0.019	0.215	0.099	48361.706	0.019
24	12572.0	0.010	0.163	0.144	48362.806	0.011
25	12573.3	0.013	0.173	0.097	48364.106	0.014
26	12577.2	0.018	0.217	0.097	48368.006	0.019
27	12579.5	0.004	0.203	0.142	48370.306	0.006

Table D.2. Continued

Peak #	λ_3	σ (λ_3)	FWHM (λ_3)	Avg I (nA)	E_{tot}	σ (E_{tot})
28	12585.1	0.015	0.165	0.097	48375.906	0.016
29	12587.3	0.017	0.224	0.098	48378.056	0.017
30	12589.7	0.032	0.265	0.058	48380.506	0.032
31	12590.5	0.024	0.267	0.097	48381.306	0.024
32	12592.9	0.007	0.181	0.110	48383.706	0.009
33	12594.2	0.005	0.232	0.132	48385.006	0.007
34	12602.2	0.003	0.243	0.172	48393.006	0.006
35	12604.6	0.012	0.199	0.104	48395.356	0.013
36	12606.1	0.004	0.201	0.138	48396.906	0.007
37	12611.8	0.011	0.180	0.111	48402.556	0.012
38	12616.5	0.003	0.204	0.149	48407.306	0.006
39	12622.4	0.004	0.201	0.146	48413.156	0.006
40	12623.4	0.002	0.206	0.186	48414.206	0.005
41	12624.4	0.006	0.183	0.119	48415.206	0.008
42	12637.2	0.005	0.170	0.125	48428.006	0.007
43	12637.9	0.008	0.158	0.110	48428.706	0.009
44	12638.4	0.019	0.164	0.095	48429.206	0.019
45	12649.7	0.004	0.198	0.146	48440.506	0.006
46	12652.0	0.001	0.210	0.277	48442.806	0.005
47	12655.4	0.015	0.181	0.120	48446.206	0.015
48	12659.5	0.006	0.497	0.256	48450.256	0.008
49	12663.7	0.018	0.182	0.110	48454.506	0.018
50	12664.2	0.003	0.207	0.241	48455.006	0.006
51	12666.9	0.009	0.168	0.124	48457.656	0.010
52	12671.2	0.007	0.250	0.152	48462.006	0.008
53	12673.7	0.015	0.168	0.108	48464.506	0.016
54	12674.4	0.024	0.150	0.098	48465.206	0.025

Table D.2. Continued

Peak #	λ_3	σ (λ_3)	FWHM (λ_3)	Avg I (nA)	E_{tot}	σ (E_{tot})
55	12676.5	0.003	0.199	0.218	48467.306	0.006
56	12677.9	0.005	0.194	0.165	48468.706	0.007
57	12680.1	0.003	0.232	0.259	48470.906	0.006
58	12683.8	0.013	0.168	0.105	48474.606	0.014
59	12684.7	0.005	0.178	0.139	48475.506	0.007
60	12686.4	0.024	0.350	0.098	48477.206	0.024
61	12686.8	0.004	0.201	0.165	48477.606	0.006
62	12691.6	0.012	0.196	0.106	48482.356	0.013
63	12693.0	0.008	0.165	0.114	48483.806	0.009
64	12695.2	0.014	0.158	0.098	48485.956	0.015
65	12700.2	0.011	0.134	0.098	48490.956	0.012
66	12700.7	0.006	0.161	0.108	48491.506	0.008
67	12702.6	0.009	0.155	0.099	48493.406	0.010
68	12705.8	0.002	0.188	0.162	48496.606	0.006
69	12707.4	0.014	0.251	0.096	48498.206	0.015
70	12708.0	0.008	0.135	0.122	48498.806	0.010
71	12709.4	0.008	0.212	0.108	48500.206	0.009
72	12713.4	0.001	0.214	0.285	48504.206	0.005
73	12714.4	0.001	0.224	0.360	48505.206	0.005
74	12715.8	0.005	0.202	0.143	48506.606	0.007
75	12716.3	0.014	0.141	0.127	48507.106	0.015
76	12719.4	0.007	0.182	0.072	48510.206	0.008
77	12719.7	0.014	-0.142	0.114	48510.456	0.015
78	12720.9	0.014	0.183	0.134	48511.706	0.015
79	12722.6	0.011	0.254	0.122	48513.406	0.012
80	12725.0	0.004	0.198	0.159	48515.806	0.006
81	12727.2	0.001	0.241	0.293	48518.006	0.005

Table D.2. Continued

Peak #	λ_3	σ (λ_3)	FWHM (λ_3)	Avg I (nA)	E_{tot}	σ (E_{tot})
82	12730.1	0.007	0.184	0.124	48520.906	0.009
83	12731.8	0.009	0.179	0.110	48522.606	0.010
84	12734.6	0.028	0.430	0.130	48525.406	0.028
85	12735.0	0.006	0.159	0.119	48525.806	0.008
86	12737.0	0.010	0.197	0.109	48527.806	0.011
87	12763.9	0.033	0.168	0.129	48554.706	0.033
88	12765.5	0.138	0.178	0.096	48556.306	0.138
89	12771.5	0.012	0.167	0.128	48562.306	0.013
90	12772.5	0.065	0.126	0.102	48563.306	0.065
91	12772.9	0.054	0.157	0.100	48563.706	0.054
92	12773.6	0.066	0.163	0.102	48564.406	0.066
93	12781.4	0.190	-0.189	0.061	48572.206	0.190
94	12786.7	0.108	0.191	0.093	48577.506	0.108
95	12787.6	0.071	0.172	0.100	48578.406	0.072
96	12788.4	0.051	0.226	0.113	48579.206	0.051
97	12789.3	0.022	0.236	0.146	48580.056	0.022
98	12790.0	0.017	0.206	0.297	48580.806	0.018
99	12790.6	0.009	0.258	0.649	48581.406	0.011
100	12790.9	0.011	0.256	0.555	48581.706	0.012
101	12791.6	0.019	0.217	0.286	48582.406	0.020
102	12792.2	0.018	0.198	0.168	48583.006	0.019
103	12792.9	0.034	0.188	0.127	48583.656	0.035
104	12793.5	0.047	0.195	0.114	48584.306	0.047
105	12794.1	0.080	0.230	0.108	48584.856	0.081
106	12794.6	0.084	0.204	0.105	48585.406	0.084
107	12795.2	0.014	0.191	0.103	48585.956	0.015
108	12795.7	0.023	0.197	0.101	48586.506	0.023

Table D.2. Continued

Peak #	λ_3	σ (λ_3)	FWHM (λ_3)	Avg I (nA)	E_{tot}	σ (E_{tot})
109	12796.2	0.026	0.220	0.100	48587.006	0.027
110	12796.6	0.019	0.218	0.102	48587.406	0.020
111	12797.1	0.042	0.307	0.107	48587.856	0.043
112	12797.5	0.020	0.344	0.115	48588.306	0.020
113	12797.9	0.012	0.241	0.131	48588.656	0.013
114	12798.2	0.011	0.260	0.131	48589.006	0.012
115	12798.6	0.010	0.260	0.135	48589.406	0.011
116	12799.0	0.011	0.215	0.131	48589.806	0.012
117	12799.3	0.025	0.261	0.123	48590.106	0.025
118	12799.7	0.043	0.350	0.121	48590.506	0.044
119	12800.3	0.017	0.332	0.199	48591.106	0.018
120	12803.7	0.010	1.049	0.373	48594.506	0.012
121	12806.9	0.004	0.680	0.714	48597.706	0.006
122	12828.9	0.002	0.269	0.517	48619.706	0.005
123	12836.9	0.068	2.750	0.122	48627.656	0.068
124	12842.4	0.002	0.533	0.521	48633.206	0.005
125	12875.0	0.001	0.330	0.625	48665.806	0.005
126	12885.6	0.113	4.328	0.122	48676.406	0.113
127	12901.1	0.090	3.687	0.206	48691.856	0.090
128	12903.2	0.122	3.019	0.153	48694.006	0.122
129	12905.2	0.249	6.499	0.153	48695.956	0.249
130	12911.9	0.101	4.694	0.189	48702.706	0.101
131	12920.7	0.066	1.560	0.093	48711.456	0.066
132	12923.5	0.011	0.430	0.140	48714.306	0.012
133	12934.5	0.003	0.276	0.269	48725.306	0.006
134	12943.7	0.003	0.489	0.521	48734.506	0.006
135	12949.5	0.002	0.525	0.705	48740.306	0.006

Table D.2. Continued

Peak #	λ_3	σ (λ_3)	FWHM (λ_3)	Avg I (nA)	E_{tot}	σ (E_{tot})
136	12955.0	0.024	1.572	0.190	48745.806	0.024
137	12961.3	0.002	0.255	0.462	48752.106	0.005
138	12974.8	0.009	0.427	0.216	48765.606	0.010
139	13000.8	0.004	0.276	0.450	48791.606	0.006
140	13010.3	0.007	1.199	0.528	48801.056	0.009
141	13025.9	0.039	2.685	0.164	48816.706	0.039
142	13038.4	0.006	1.229	0.634	48829.206	0.008
143	13042.6	0.009	0.348	0.269	48833.406	0.010
144	13062.2	0.060	2.231	0.133	48853.006	0.061
145	13071.5	0.011	0.633	0.203	48862.256	0.012
146	13076.0	0.020	1.129	0.189	48866.806	0.020
147	13080.7	0.003	0.228	0.399	48871.506	0.006
148	13083.5	0.011	1.511	0.340	48874.306	0.012
149	13088.7	0.028	1.730	0.212	48879.506	0.029
150	13098.3	0.097	2.639	0.168	48889.056	0.097
151	13100.9	0.009	0.046	0.434	48891.656	0.010
152	13115.1	0.021	0.997	0.226	48905.906	0.021
153	13117.4	0.002	0.406	0.768	48908.206	0.005
154	13132.8	0.040	0.456	0.144	48923.606	0.040
155	13142.0	0.013	0.357	0.175	48932.806	0.014
156	13148.9	0.013	1.050	0.254	48939.706	0.014

Table D.3: $E_2 = 35977.442\ cm^{-1}$

Peak #	λ_3	σ (λ_3)	FWHM (λ_3)	Avg I (nA)	E_{tot}	σ (E_{tot})
1	12299.560	0.005	0.192	0.193	48277.002	0.007
2	12299.998	0.010	0.176	0.145	48277.440	0.011
3	12312.394	0.130	14.113	0.143	48289.836	0.131
4	12321.050	0.001	0.218	1.114	48298.492	0.005
5	12321.650	0.006	0.158	0.355	48299.092	0.008
6	12325.178	0.004	0.184	0.444	48302.620	0.006
7	12326.351	0.002	0.233	0.732	48303.793	0.005
8	12328.785	0.002	0.208	0.879	48306.227	0.005
9	12336.005	0.005	0.209	0.595	48313.447	0.007
10	12338.682	0.020	0.018	0.337	48316.124	0.021
11	12344.495	0.011	0.215	0.410	48321.937	0.012
12	12345.524	0.015	0.246	0.393	48322.966	0.016
13	12347.998	0.004	0.207	0.661	48325.440	0.006
14	12350.807	0.005	0.193	0.564	48328.249	0.007
15	12351.697	0.007	0.127	0.144	48329.139	0.008
16	12356.792	0.005	0.202	0.628	48334.234	0.007
17	12366.289	0.004	0.212	0.533	48343.731	0.006
18	12368.347	0.024	0.436	0.353	48345.789	0.025
19	12368.585	0.010	0.152	0.409	48346.027	0.011
20	12371.636	0.023	0.390	0.316	48349.078	0.024
21	12381.282	0.017	0.142	0.318	48358.724	0.017
22	12383.059	0.004	0.181	0.460	48360.501	0.007
23	12384.286	0.003	0.188	0.570	48361.728	0.006
24	12385.311	0.003	0.177	0.558	48362.753	0.006
25	12386.697	0.007	0.194	0.396	48364.139	0.008
26	12393.554	0.011	0.184	0.390	48370.996	0.012
27	12398.486	0.001	0.193	1.002	48375.928	0.005

Table D.3. Continued

Peak #	λ_3	σ (λ_3)	FWHM (λ_3)	Avg I (nA)	E_{tot}	σ (E_{tot})
28	12400.577	0.014	0.271	0.355	48378.019	0.015
29	12403.834	0.004	0.186	0.535	48381.276	0.006
30	12407.509	0.001	0.219	1.621	48384.951	0.005
31	12415.578	0.011	0.182	0.377	48393.020	0.012
32	12417.909	0.002	0.187	0.805	48395.351	0.005
33	12419.493	0.093	2.488	0.319	48396.935	0.093
34	12420.691	0.009	0.177	0.414	48398.133	0.010
35	12429.851	0.001	0.198	1.380	48407.293	0.005
36	12433.214	0.017	0.246	0.438	48410.656	0.018
37	12435.717	0.004	0.190	0.761	48413.159	0.007
38	12436.727	0.003	0.220	1.121	48414.169	0.006
39	12437.757	0.008	0.181	0.464	48415.199	0.010
40	12441.620	0.336	8.198	0.313	48419.062	0.336
41	12450.595	0.002	0.162	0.669	48428.037	0.005
42	12451.269	0.005	0.193	0.471	48428.711	0.007
43	12453.697	0.005	0.194	0.451	48431.139	0.007
44	12455.637	0.001	0.273	1.122	48433.079	0.005
45	12457.935	0.002	0.186	0.675	48435.377	0.006
46	12463.101	0.001	0.192	1.282	48440.543	0.005
47	12464.258	0.008	0.195	0.384	48441.700	0.009
48	12464.816	0.004	0.193	0.515	48442.258	0.006
49	12465.371	0.006	0.205	0.432	48442.813	0.008
50	12465.824	0.020	-0.030	0.306	48443.266	0.021
51	12467.587	0.010	0.145	0.303	48445.029	0.011
52	12468.745	0.005	0.187	0.350	48446.187	0.007
53	12469.621	0.001	0.186	2.094	48447.063	0.005
54	12472.729	0.002	0.218	2.350	48450.171	0.005

Table D.3. Continued

Peak #	λ_3	σ (λ_3)	FWHM (λ_3)	Avg I (nA)	E_{tot}	σ (E_{tot})
55	12473.068	0.001	0.209	3.253	48450.510	0.005
56	12475.317	0.001	0.198	2.334	48452.759	0.005
57	12477.040	0.002	0.192	1.262	48454.482	0.005
58	12477.545	0.001	0.210	2.616	48454.987	0.005
59	12484.274	0.002	0.193	1.063	48461.716	0.006
60	12484.549	0.003	0.201	0.911	48461.991	0.006
61	12487.052	0.001	0.183	1.904	48464.494	0.005
62	12487.727	0.003	0.197	0.865	48465.169	0.006
63	12489.831	0.009	0.187	0.390	48467.273	0.011
64	12491.238	0.001	0.188	2.110	48468.680	0.005
65	12493.450	0.003	0.174	0.733	48470.892	0.006
66	12497.173	0.009	0.187	0.393	48474.615	0.010
67	12498.096	0.004	0.188	0.540	48475.538	0.007
68	12502.045	0.010	0.192	0.382	48479.487	0.012
69	12504.913	0.001	0.194	1.793	48482.355	0.005
70	12506.034	0.002	0.186	0.907	48483.476	0.006
71	12506.394	0.018	0.163	0.315	48483.836	0.018
72	12508.510	0.007	0.006	0.446	48485.952	0.009
73	12509.916	0.011	0.172	0.306	48487.358	0.012
74	12513.501	0.003	0.175	0.487	48490.943	0.006
75	12514.023	0.006	0.167	0.361	48491.465	0.008
76	12515.028	0.007	0.161	0.185	48492.470	0.009
77	12515.953	0.015	0.218	0.310	48493.395	0.016
78	12519.112	0.001	0.195	2.625	48496.554	0.005
79	12520.816	0.011	0.212	0.480	48498.258	0.012
80	12521.320	0.002	0.182	1.081	48498.762	0.006
81	12521.970	0.007	0.154	0.334	48499.412	0.009

Table D.3. Continued

Peak #	λ_3	σ (λ_3)	FWHM (λ_3)	Avg I (nA)	E_{tot}	σ (E_{tot})
82	12522.775	0.013	0.177	0.310	48500.217	0.014
83	12523.627	0.006	0.195	0.375	48501.069	0.008
84	12526.785	0.003	0.181	0.780	48504.227	0.006
85	12527.071	0.013	0.140	0.211	48504.513	0.014
86	12527.435	0.029	0.364	0.227	48504.877	0.030
87	12527.792	0.002	0.181	1.163	48505.234	0.005
88	12528.235	0.012	0.173	0.600	48505.677	0.013
89	12529.413	0.006	0.190	1.106	48506.855	0.008
90	12529.710	0.004	0.180	1.431	48507.152	0.006
91	12532.775	0.001	0.202	3.330	48510.217	0.005
92	12534.250	0.007	0.183	0.911	48511.692	0.009
93	12535.983	0.003	0.226	1.878	48513.425	0.006
94	12538.383	0.020	0.233	0.307	48515.825	0.021
95	12539.444	0.012	0.196	0.317	48516.886	0.013
96	12540.510	0.001	0.197	1.925	48517.952	0.005
97	12543.463	0.007	0.209	0.398	48520.905	0.009
98	12545.170	0.003	0.189	0.545	48522.612	0.006
99	12547.620	0.006	0.289	1.015	48525.062	0.008
100	12548.359	0.001	0.220	4.217	48525.801	0.005
101	12549.593	0.009	0.249	0.206	48527.035	0.010
102	12549.591	0.044	0.292	0.326	48527.033	0.044
103	12550.385	0.001	0.211	3.728	48527.827	0.005
104	12551.558	0.006	0.224	0.202	48529.000	0.008
105	12553.971	0.002	0.193	1.369	48531.413	0.005
106	12554.741	0.023	0.144	0.327	48532.183	0.024
107	12555.874	0.019	0.191	0.370	48533.316	0.020
108	12557.062	0.081	0.378	0.360	48534.504	0.081

Table D.3. Continued

Peak #	λ_3	σ (λ_3)	FWHM (λ_3)	Avg I (nA)	E_{tot}	σ (E_{tot})
109	12557.639	0.002	0.225	1.966	48535.081	0.005
110	12559.615	0.021	0.151	0.364	48537.057	0.022
111	12560.388	0.016	0.135	0.339	48537.830	0.017
112	12561.004	0.004	0.201	0.755	48538.446	0.006
113	12563.481	0.019	0.174	0.354	48540.923	0.019
114	12564.185	0.004	0.203	0.663	48541.627	0.006
115	12566.439	0.015	0.152	0.354	48543.881	0.016
116	12567.167	0.005	0.202	0.581	48544.609	0.007
117	12569.237	0.014	0.192	0.376	48546.679	0.015
118	12569.954	0.007	0.269	0.528	48547.396	0.009
119	12571.533	0.026	0.197	0.346	48548.975	0.026
120	12571.854	0.010	0.182	0.423	48549.296	0.011
121	12572.520	0.007	0.208	0.510	48549.962	0.008
122	12574.138	0.006	0.310	0.565	48551.580	0.008
123	12574.298	0.002	0.178	0.420	48551.740	0.005
124	12574.950	0.006	0.225	0.459	48552.392	0.008
125	12576.349	0.011	0.299	2.436	48553.791	0.012
126	12576.523	0.011	0.218	1.406	48553.965	0.012
127	12577.296	0.002	0.235	6.123	48554.738	0.006
128	12578.895	0.004	0.199	1.044	48556.337	0.007
129	12579.354	0.024	0.158	0.412	48556.796	0.024
130	12580.645	0.065	0.254	0.351	48558.087	0.065
131	12580.897	0.015	0.179	0.524	48558.339	0.016
132	12581.378	0.062	0.476	0.406	48558.820	0.062
133	12581.813	0.001	0.187	2.932	48559.255	0.005
134	12582.676	0.003	0.202	1.050	48560.118	0.006
135	12583.245	0.023	0.195	0.365	48560.687	0.024

Table D.3. Continued

Peak #	λ_3	σ (λ_3)	FWHM (λ_3)	Avg I (nA)	E_{tot}	σ (E_{tot})
136	12584.448	0.004	0.203	0.406	48561.890	0.007
137	12585.015	0.008	0.230	0.345	48562.457	0.009
138	12586.171	0.010	0.262	0.331	48563.613	0.011
139	12586.694	0.008	0.186	0.342	48564.136	0.009
140	12587.774	0.012	0.216	0.309	48565.216	0.013
141	12588.265	0.007	0.165	0.335	48565.707	0.009
142	12589.294	0.022	0.197	0.268	48566.736	0.023
143	12589.754	0.009	0.192	0.300	48567.196	0.010
144	12590.720	0.028	0.244	0.269	48568.162	0.028
145	12591.162	0.008	0.021	0.325	48568.604	0.010
146	12591.800	0.090	0.983	0.336	48569.242	0.090
147	12592.498	0.010	0.199	0.304	48569.940	0.012
148	12593.336	0.027	0.379	0.209	48570.778	0.028
149	12593.754	0.010	0.215	0.310	48571.196	0.011
150	12594.616	0.031	0.281	0.258	48572.058	0.031
151	12594.954	0.009	0.195	0.298	48572.396	0.010
152	12596.082	0.016	0.288	0.302	48573.524	0.016
153	12596.862	0.026	0.263	0.337	48574.304	0.026
154	12597.171	0.010	0.209	0.319	48574.613	0.011
155	12598.211	0.011	0.159	0.306	48575.653	0.012
156	12598.863	0.029	0.284	0.363	48576.305	0.030
157	12599.170	0.012	0.220	0.332	48576.612	0.013
158	12599.712	0.011	0.167	0.212	48577.154	0.012
159	12600.106	0.009	0.253	0.329	48577.548	0.010
160	12600.986	0.009	0.222	0.366	48578.428	0.010
161	12601.825	0.008	0.188	0.401	48579.267	0.010
162	12602.626	0.005	0.247	0.497	48580.068	0.007

Table D.3. Continued

Peak #	λ_3	σ (λ_3)	FWHM (λ_3)	Avg I (nA)	E_{tot}	σ (E_{tot})
163	12603.383	0.007	0.296	0.794	48580.825	0.009
164	12603.934	0.004	0.243	2.601	48581.376	0.006
165	12604.266	0.008	0.263	1.643	48581.708	0.009
166	12604.874	0.008	0.279	0.522	48582.316	0.009
167	12605.508	0.010	0.346	0.340	48582.950	0.011
168	12606.131	0.028	0.321	0.302	48583.573	0.028
169	12606.782	0.030	0.288	0.304	48584.224	0.030
170	12607.304	0.039	0.340	0.288	48584.746	0.039
171	12607.834	0.029	0.421	0.291	48585.276	0.029
172	12608.458	0.025	0.245	0.302	48585.900	0.026
173	12608.945	0.022	0.250	0.300	48586.387	0.023
174	12609.113	0.063	17.782	0.290	48586.555	0.063
175	12609.482	0.030	0.320	0.302	48586.924	0.031
176	12609.934	0.027	0.303	0.312	48587.376	0.028
177	12610.441	0.025	11.886	0.322	48587.883	0.026
178	12610.844	0.014	0.191	0.359	48588.286	0.014
179	12611.244	0.014	0.233	0.389	48588.686	0.015
180	12611.978	0.013	0.180	0.443	48589.420	0.014
181	12612.284	0.016	-0.100	0.338	48589.726	0.017
182	12612.713	0.002	0.234	0.643	48590.155	0.005
183	12613.623	0.002	0.373	10.770	48591.065	0.005
184	12614.642	0.010	0.211	0.817	48592.084	0.012
185	12617.051	0.057	0.857	0.968	48594.493	0.057
186	12620.293	0.008	0.703	4.902	48597.735	0.010
187	12626.751	0.015	1.154	3.489	48604.193	0.016
188	12642.234	0.011	0.201	1.951	48619.676	0.012
189	12655.769	0.005	0.586	6.475	48633.211	0.007

Table D.3. Continued

Peak #	λ_3	σ (λ_3)	FWHM (λ_3)	Avg I (nA)	E_{tot}	σ (E_{tot})
190	12659.643	0.004	0.627	8.613	48637.085	0.007
191	12677.561	0.021	4.784	1.860	48655.003	0.022
192	12686.350	0.023	0.029	0.877	48663.792	0.024
193	12688.392	0.001	0.328	7.686	48665.834	0.005
194	12698.272	0.051	3.206	0.820	48675.714	0.052
195	12707.993	0.010	1.245	1.830	48685.435	0.011
196	12719.142	0.024	1.821	2.510	48696.584	0.025
197	12726.409	0.011	2.159	4.988	48703.851	0.012
198	12733.959	0.045	2.282	0.450	48711.401	0.045
199	12737.214	0.022	1.340	0.625	48714.656	0.023
200	12757.066	0.003	0.445	1.504	48734.508	0.006
201	12762.836	0.004	0.414	1.389	48740.278	0.006
202	12768.568	0.055	1.992	0.453	48746.010	0.055
203	12774.625	0.001	0.278	6.318	48752.067	0.005
204	12775.386	0.040	1.136	1.050	48752.828	0.040
205	12786.757	0.074	2.390	0.866	48764.199	0.074
206	12788.123	0.003	0.408	4.782	48765.565	0.006
207	12814.124	0.010	0.259	2.577	48791.566	0.011
208	12821.083	0.164	7.849	1.789	48798.525	0.164
209	12839.339	0.050	3.036	2.051	48816.781	0.050
210	12851.891	0.010	1.879	6.893	48829.333	0.011
211	12875.037	0.060	3.172	1.609	48852.479	0.060
212	12884.918	0.018	0.765	1.029	48862.360	0.019
213	12889.053	0.047	1.091	0.722	48866.495	0.047
214	12894.014	0.009	0.258	0.596	48871.456	0.011
215	12896.889	0.018	1.459	1.703	48874.331	0.019
216	12901.977	0.015	1.764	1.983	48879.419	0.015

Table D.3. Continued

Peak #	λ_3	σ (λ_3)	FWHM (λ_3)	Avg I (nA)	E_{tot}	σ (E_{tot})
217	12911.058	0.037	1.593	1.103	48888.500	0.037
218	12914.000	0.026	1.246	0.554	48891.442	0.026
219	12920.538	0.002	0.391	10.008	48897.980	0.005
220	12923.497	0.014	0.327	0.560	48900.939	0.015
221	12925.091	0.019	0.568	0.606	48902.533	0.020
222	12928.471	0.007	1.171	6.892	48905.913	0.008
223	12930.802	0.003	0.438	8.533	48908.244	0.006
224	12934.519	0.007	0.243	2.901	48911.961	0.009
225	12946.172	0.006	0.631	5.556	48923.614	0.008
226	12947.136	0.015	0.422	2.608	48924.578	0.015
227	12955.363	0.004	0.381	6.216	48932.805	0.006

Table D.4: $E_2 = 36313.781\ cm^{-1}$

Peak #	λ_3	σ (λ_3)	FWHM (λ_3)	Avg I (nA)	E_{tot}	σ (E_{tot})
1	12093.5	0.006	0.209	1.955	48407.281	0.007
2	12099.4	0.004	0.183	1.997	48413.181	0.006
3	12100.4	0.014	0.192	1.506	48414.181	0.014
4	12114.3	0.007	0.141	1.711	48428.081	0.008
5	12117.4	0.005	0.174	1.954	48431.181	0.007
6	12121.6	0.003	0.194	2.675	48435.381	0.005
7	12126.8	0.003	0.179	3.190	48440.581	0.005
8	12127.9	0.002	0.161	3.184	48441.681	0.005
9	12129.0	0.001	0.191	6.646	48442.781	0.004
10	12131.3	0.018	0.213	1.372	48445.031	0.019
11	12132.4	0.007	0.153	1.804	48446.181	0.008
12	12133.3	0.095	0.855	1.469	48447.081	0.096
13	12136.4	0.001	0.202	6.947	48450.181	0.004
14	12136.7	0.005	0.161	2.098	48450.481	0.006
15	12139.0	0.002	0.198	3.757	48452.781	0.005
16	12140.9	0.009	0.104	1.544	48454.631	0.010
17	12141.2	0.002	0.198	4.588	48454.981	0.005
18	12143.9	0.017	0.212	1.574	48457.681	0.018
19	12148.2	0.003	0.365	5.182	48461.981	0.005
20	12150.7	0.015	0.182	1.802	48464.481	0.016
21	12151.3	0.060	0.205	1.449	48465.081	0.060
22	12153.5	0.024	0.203	1.697	48467.281	0.025
23	12154.9	0.006	0.160	2.704	48468.681	0.007
24	12157.1	0.004	0.185	3.188	48470.881	0.006
25	12160.8	0.046	0.232	1.474	48474.531	0.046
26	12161.8	0.020	0.153	1.628	48475.581	0.021
27	12165.7	0.005	0.208	2.111	48479.481	0.006

Table D.4. Continued

Peak #	λ_3	σ (λ_3)	FWHM (λ_3)	Avg I (nA)	E_{tot}	σ (E_{tot})
28	12168.6	0.009	0.205	2.006	48482.381	0.010
29	12169.7	0.007	0.224	1.871	48483.481	0.008
30	12172.2	0.013	0.279	1.428	48485.981	0.014
31	12173.6	0.005	0.166	1.977	48487.381	0.007
32	12177.2	0.013	0.171	1.375	48490.981	0.014
33	12180.8	0.011	0.169	1.682	48494.531	0.012
34	12182.8	0.006	0.171	2.377	48496.581	0.008
35	12185.0	0.008	0.193	2.168	48498.781	0.009
36	12187.3	0.011	0.193	1.885	48501.081	0.012
37	12190.5	0.002	0.200	4.428	48504.231	0.005
38	12191.5	0.001	0.198	7.504	48505.231	0.004
39	12192.9	0.020	0.530	2.001	48506.681	0.021
40	12193.4	0.002	0.186	5.163	48507.181	0.005
41	12196.7	0.025	0.327	1.635	48510.481	0.025
42	12199.5	0.005	0.197	2.642	48513.281	0.006
43	12202.2	0.010	0.264	1.997	48515.981	0.011
44	12204.2	0.001	0.219	9.049	48517.981	0.004
45	12207.0	0.005	0.225	2.703	48520.781	0.006
46	12208.8	1.090	534.652	1.523	48522.581	1.090
47	12211.4	0.010	0.270	2.928	48525.181	0.011
48	12214.1	0.024	0.160	1.775	48527.881	0.024
49	12215.2	0.004	0.193	4.480	48528.981	0.006
50	12215.7	0.044	0.224	1.687	48529.481	0.044
51	12217.7	0.022	0.142	1.769	48531.431	0.023
52	12218.4	0.002	0.186	7.455	48532.181	0.005
53	12219.5	0.008	0.195	2.885	48533.281	0.009
54	12220.7	0.022	0.193	2.397	48534.481	0.023

Table D.4. Continued

Peak #	λ_3	σ (λ_3)	FWHM (λ_3)	Avg I (nA)	E_{tot}	σ (E_{tot})
55	12221.3	0.004	0.358	11.992	48535.031	0.006
56	12223.3	0.006	0.221	1.956	48537.081	0.007
57	12224.1	0.001	0.194	4.941	48537.881	0.004
58	12224.6	0.015	0.302	1.622	48538.381	0.016
59	12227.2	0.002	0.180	3.437	48540.931	0.005
60	12227.9	0.010	0.193	1.599	48541.631	0.011
61	12230.1	0.003	0.184	2.528	48543.881	0.005
62	12230.8	0.015	0.187	1.513	48544.581	0.015
63	12232.9	0.003	0.211	2.219	48546.681	0.005
64	12233.6	0.020	0.337	1.492	48547.381	0.021
65	12235.5	0.008	0.208	1.698	48549.281	0.009
66	12236.2	0.017	0.166	1.393	48549.981	0.017
67	12238.0	0.010	0.196	1.483	48551.731	0.011
68	12238.6	0.054	0.967	1.382	48552.381	0.054
69	12240.0	0.019	0.239	1.336	48553.781	0.019
70	12241.0	0.005	0.210	2.446	48554.731	0.006
71	12242.6	0.007	0.198	1.973	48556.381	0.008
72	12243.0	0.013	0.243	1.400	48556.781	0.014
73	12244.3	0.009	0.007	1.785	48558.081	0.010
74	12244.6	0.008	0.156	1.742	48558.331	0.009
75	12245.5	0.001	0.209	8.873	48559.281	0.004
76	12246.3	0.004	0.208	3.029	48560.081	0.006
77	12248.2	0.017	0.346	1.644	48561.981	0.018
78	12250.0	0.029	0.337	1.533	48563.731	0.030
79	12251.6	0.048	0.475	1.442	48565.331	0.048
80	12253.1	0.037	0.476	1.505	48566.881	0.037
81	12254.6	0.020	0.490	1.488	48568.331	0.021

Table D.4. Continued

Peak #	λ_3	σ (λ_3)	FWHM (λ_3)	Avg I (nA)	E_{tot}	σ (E_{tot})
82	12256.0	0.029	0.618	1.464	48569.731	0.030
83	12257.2	0.017	0.363	1.489	48570.981	0.018
84	12258.4	0.015	0.298	1.465	48572.181	0.016
85	12259.6	0.017	0.347	1.413	48573.381	0.018
86	12260.6	0.014	0.206	1.370	48574.381	0.014
87	12261.7	0.013	0.218	1.376	48575.481	0.014
88	12262.7	0.009	0.206	1.453	48576.481	0.010
89	12263.7	0.010	0.255	1.477	48577.431	0.011
90	12264.6	0.008	0.227	1.604	48578.331	0.009
91	12265.4	0.013	0.203	2.083	48579.181	0.014
92	12266.3	0.006	0.291	3.177	48580.081	0.008
93	12267.0	0.028	0.204	7.794	48580.781	0.028
94	12267.6	0.011	0.284	23.754	48581.381	0.012
95	12268.0	0.014	0.273	18.998	48581.781	0.014
96	12268.6	0.029	0.253	7.306	48582.381	0.029
97	12269.2	0.004	0.259	4.158	48582.981	0.006
98	12269.9	0.007	0.201	2.867	48583.681	0.008
99	12270.5	0.009	0.169	2.521	48584.281	0.010
100	12271.1	0.005	0.198	2.177	48584.881	0.007
101	12271.7	0.008	0.187	2.026	48585.431	0.009
102	12272.2	0.007	0.197	2.048	48585.981	0.009
103	12272.7	0.012	0.264	1.935	48586.481	0.013
104	12273.2	0.008	0.219	2.070	48586.981	0.009
105	12273.7	0.012	0.341	2.082	48587.481	0.013
106	12277.3	0.003	0.277	14.346	48591.081	0.005
107	12280.7	0.025	0.906	5.029	48594.481	0.025
108	12284.0	0.006	0.629	12.540	48597.731	0.007

Table D.4. Continued

Peak #	λ_3	σ (λ_3)	FWHM (λ_3)	Avg I (nA)	E_{tot}	σ (E_{tot})
109	12290.4	0.007	1.083	13.903	48604.181	0.008
110	12313.3	0.029	2.898	2.525	48627.081	0.030
111	12319.5	0.008	0.399	2.937	48633.231	0.009
112	12323.9	0.013	2.559	4.304	48637.681	0.013
113	12341.2	0.205	-3.869	1.967	48654.981	0.205
114	12352.1	0.004	0.238	3.487	48665.831	0.006
115	12362.1	0.045	2.936	2.714	48675.881	0.046
116	12371.9	0.033	1.778	3.537	48685.681	0.034
117	12377.4	0.036	4.807	4.264	48691.181	0.036
118	12382.5	0.027	1.788	3.579	48696.281	0.027
119	12390.8	0.066	1.511	2.260	48704.581	0.066
120	12397.3	0.013	-0.112	4.987	48711.081	0.013
121	12400.7	0.061	2.276	2.171	48714.431	0.062
122	12420.7	0.004	0.390	4.212	48734.481	0.006
123	12426.5	0.005	0.447	4.413	48740.281	0.006
124	12438.3	0.001	0.255	12.238	48752.081	0.004
125	12450.3	0.021	2.170	3.051	48764.081	0.021
126	12451.8	0.013	0.523	2.169	48765.581	0.014
127	12455.6	0.004	0.255	4.026	48769.381	0.006
128	12477.8	0.011	0.309	4.072	48791.581	0.012
129	12487.1	0.025	1.170	5.474	48800.831	0.025
130	12491.6	0.004	0.887	20.125	48805.381	0.006
131	12516.3	0.097	2.334	3.041	48830.081	0.097
132	12536.9	0.050	2.780	4.382	48850.681	0.050
133	12560.5	0.014	1.469	8.288	48874.281	0.015
134	12577.9	0.009	1.565	12.615	48891.681	0.010
135	12592.2	0.030	1.166	3.166	48905.981	0.030

Table D.4. Continued

Peak #	λ_3	σ (λ_3)	FWHM (λ_3)	Avg I (nA)	E_{tot}	σ (E_{tot})
136	12594.5	0.001	0.456	34.202	48908.281	0.004
137	12609.9	0.003	0.555	9.969	48923.648	0.005
138	12626.1	0.003	0.728	9.002	48939.881	0.005
139	12660.8	0.003	0.260	6.880	48974.581	0.005
140	12667.0	0.004	0.238	5.304	48980.781	0.006
141	12676.3	0.015	0.883	6.937	48990.081	0.015
142	12682.9	0.128	3.571	3.983	48996.681	0.128
143	12697.5	0.004	0.348	16.906	49011.281	0.006
144	12699.1	0.037	1.665	5.743	49012.831	0.037
145	12707.1	0.005	0.939	27.181	49020.881	0.007
146	12714.4	0.160	2.037	2.500	49028.181	0.160
147	12725.6	0.042	3.080	8.276	49039.381	0.042
148	12743.6	0.033	0.778	4.824	49057.381	0.033
149	12768.8	0.004	0.618	14.791	49082.581	0.006
150	12775.3	0.014	1.149	6.210	49089.031	0.015

Table D.5: $E_2 = 36452.504\ cm^{-1}$

Peak #	λ_3	σ (λ_3)	FWHM (λ_3)	Avg I (nA)	E_{tot}	σ (E_{tot})
1	12052.5	0.013	0.161	2.239	48505.004	0.015
2	12053.5	0.012	0.219	2.375	48506.004	0.014
3	12058.5	0.013	0.193	2.315	48511.004	0.015
4	12064.1	0.024	0.250	1.998	48516.604	0.025
5	12067.2	0.022	0.193	1.974	48519.704	0.023
6	12070.7	0.027	0.182	1.830	48523.204	0.028
7	12074.0	0.009	0.186	1.509	48526.504	0.012
8	12076.1	0.012	0.178	1.296	48528.604	0.015
9	12081.6	0.013	0.158	1.760	48534.104	0.015
10	12082.7	0.017	0.230	2.174	48535.204	0.018
11	12083.4	0.002	0.225	4.698	48535.854	0.008
12	12085.3	0.017	0.177	1.683	48537.804	0.018
13	12129.8	0.014	0.681	2.432	48582.304	0.016
14	12142.8	0.011	1.054	2.961	48595.304	0.013
15	12185.3	0.005	0.314	5.250	48637.804	0.009
16	12224.2	0.079	2.628	2.441	48676.654	0.079
17	12238.3	0.011	2.307	8.194	48690.804	0.014
18	12252.1	0.071	1.229	1.938	48704.554	0.072
19	12263.1	0.167	1.553	2.245	48715.604	0.167
20	12288.6	0.004	0.423	5.911	48741.054	0.009
21	12300.3	0.016	0.316	2.102	48752.804	0.018
22	12306.0	0.002	0.063	11.849	48758.504	0.008
23	12339.8	0.002	0.291	6.391	48792.304	0.008
24	12365.6	0.367	4.268	1.752	48818.104	0.367
25	12394.7	0.016	1.779	4.777	48847.204	0.018
26	12399.1	0.890	0.448	1.983	48851.604	0.890
27	12409.7	0.108	3.722	1.964	48862.154	0.108

Table D.5. Continued

Peak #	λ_3	σ (λ_3)	FWHM (λ_3)	Avg I (nA)	E_{tot}	σ (E_{tot})
28	12422.2	0.554	3.106	1.899	48874.704	0.554
29	12436.5	0.046	2.539	3.562	48889.004	0.047
30	12455.6	0.009	0.253	2.565	48908.104	0.012
31	12456.5	0.005	0.328	4.094	48909.004	0.009
32	12461.9	0.001	0.301	10.499	48914.404	0.008
33	12473.3	1.153	1.413	2.488	48925.771	1.153
34	12481.0	0.004	0.372	5.513	48933.504	0.009
35	12523.2	2.302	1.433	2.432	48975.654	2.302
36	12529.0	0.004	0.288	4.764	48981.504	0.008
37	12538.5	0.033	1.251	2.193	48990.954	0.034
38	12544.5	0.036	0.981	2.253	48997.004	0.037
39	12547.7	0.024	0.320	1.941	49000.154	0.025
40	12556.3	0.056	1.760	1.881	49008.754	0.056
41	12566.5	0.498	26.071	2.399	49019.004	0.498

Table D.6: $E_2 = 36689.646\ cm^{-1}$

Peak #	λ_3	σ (λ_3)	FWHM (λ_3)	Avg I (nA)	E_{tot}	σ (E_{tot})
1	11802.756	0.024	0.303	0.192	48492.402	0.025
2	11804.898	0.007	0.192	0.231	48494.544	0.011
3	11811.434	0.010	0.165	0.391	48501.080	0.013
4	11814.586	0.005	0.191	0.533	48504.232	0.010
5	11815.585	0.002	0.155	0.673	48505.231	0.009
6	11817.518	0.007	0.158	0.496	48507.164	0.011
7	11820.595	0.005	0.192	0.796	48510.241	0.010
8	11822.036	0.016	0.138	0.655	48511.682	0.018
9	11823.781	0.005	0.243	0.642	48513.427	0.010
10	11828.493	0.014	0.320	0.479	48518.139	0.016
11	11836.163	0.004	0.189	0.662	48525.809	0.009
12	11838.196	0.002	0.183	0.894	48527.842	0.009
13	11840.636	0.025	18.586	0.630	48530.282	0.027
14	11841.773	0.004	0.196	0.631	48531.419	0.009
15	11842.577	0.011	0.091	0.633	48532.223	0.014
16	11845.413	0.004	0.206	0.638	48535.059	0.010
17	11848.815	0.006	0.183	0.547	48538.461	0.010
19	11851.233	0.014	0.132	0.603	48540.879	0.017
22	11851.977	0.010	0.205	0.482	48541.623	0.013
24	11853.862	0.040	0.255	0.578	48543.508	0.041
25	11854.244	0.020	0.221	0.603	48543.890	0.021
26	11854.972	0.015	0.255	0.449	48544.618	0.017
27	11857.227	0.040	0.437	0.606	48546.873	0.041
28	11857.741	0.012	0.244	0.441	48547.387	0.015
29	11860.352	0.012	0.162	0.409	48549.998	0.015
30	11862.094	0.018	0.180	0.389	48551.740	0.020
31	11862.759	0.022	0.174	0.394	48552.405	0.024

Table D.6. Continued

Peak #	λ_3	σ (λ_3)	FWHM (λ_3)	Avg I (nA)	E_{tot}	σ (E_{tot})
32	11864.274	0.013	0.405	0.541	48553.920	0.016
33	11865.099	0.002	0.203	1.132	48554.745	0.009
34	11866.398	0.009	0.187	0.450	48556.044	0.012
35	11866.726	0.015	0.234	0.418	48556.372	0.017
36	11867.145	0.013	0.193	0.418	48556.791	0.016
37	11868.410	0.007	-0.005	0.489	48558.056	0.011
38	11869.610	0.002	0.201	1.195	48559.256	0.009
39	11870.488	0.014	0.255	0.492	48560.134	0.016
40	11872.818	0.009	0.182	0.531	48562.464	0.013
41	11873.694	0.007	0.159	0.521	48563.340	0.011
42	11874.088	0.016	0.274	0.478	48563.734	0.018
43	11874.698	0.009	0.237	0.508	48564.344	0.013
44	11875.677	0.021	0.117	0.386	48565.323	0.023
45	11876.054	0.021	0.313	0.423	48565.700	0.023
46	11877.471	0.030	-0.023	0.412	48567.117	0.031
47	11878.810	0.043	0.653	0.399	48568.456	0.044
48	11880.194	0.032	0.090	0.408	48569.840	0.033
49	11880.919	0.010	0.213	0.456	48570.565	0.013
50	11881.373	0.023	0.141	0.394	48571.019	0.025
51	11882.601	0.017	0.201	0.408	48572.247	0.019
52	11883.793	0.018	0.146	0.407	48573.439	0.020
53	11884.864	0.012	0.154	0.413	48574.510	0.015
54	11885.895	0.016	0.197	0.416	48575.541	0.019
55	11886.852	0.013	0.256	0.433	48576.498	0.016
56	11887.823	0.009	0.174	0.445	48577.469	0.013
57	11888.724	0.007	0.193	0.472	48578.370	0.011
58	11889.587	0.006	0.234	0.569	48579.233	0.011

Table D.6. Continued

Peak #	λ_3	σ (λ_3)	FWHM (λ_3)	Avg I (nA)	E_{tot}	σ (E_{tot})
59	11890.396	0.007	0.236	0.834	48580.042	0.011
60	11891.178	0.010	0.337	1.888	48580.824	0.013
61	11891.734	0.007	0.274	5.655	48581.380	0.011
62	11892.091	0.008	0.288	4.635	48581.737	0.012
63	11892.697	0.006	0.282	1.540	48582.343	0.010
64	11893.362	0.004	0.236	0.947	48583.008	0.009
65	11894.011	0.008	0.186	0.648	48583.657	0.011
66	11894.630	0.013	0.178	0.568	48584.276	0.015
67	11895.225	0.007	0.257	0.536	48584.871	0.011
68	11895.777	0.011	0.200	0.462	48585.423	0.014
69	11896.332	0.010	0.248	0.469	48585.978	0.013
70	11896.814	0.051	0.396	0.455	48586.460	0.052
71	11897.353	0.015	0.310	0.467	48586.999	0.018
72	11897.806	0.017	0.301	0.457	48587.452	0.019
73	11898.280	0.014	0.189	0.220	48587.926	0.016
74	11898.617	0.027	0.319	0.218	48588.263	0.029
75	11901.467	0.005	0.239	0.851	48591.113	0.010
76	11904.978	0.010	0.930	0.876	48594.624	0.013
77	11908.095	0.009	0.609	0.829	48597.741	0.012
78	11914.561	0.006	1.196	4.662	48604.207	0.011
79	11930.034	0.006	0.236	1.339	48619.680	0.011
80	11937.910	0.073	3.049	0.765	48627.556	0.073
81	11943.628	0.020	0.460	0.470	48633.274	0.022
82	11947.465	0.014	0.284	0.730	48637.111	0.016
83	11965.204	0.021	5.247	2.269	48654.850	0.022
84	11986.099	0.076	1.932	0.781	48675.745	0.076
85	12007.243	0.062	1.342	1.448	48696.889	0.063

Table D.6. Continued

Peak #	λ_3	σ (λ_3)	FWHM (λ_3)	Avg I (nA)	E_{tot}	σ (E_{tot})
86	12014.166	0.013	2.119	5.175	48703.812	0.016
87	12024.720	0.009	0.564	0.951	48714.366	0.012
88	12050.659	0.002	0.428	1.827	48740.305	0.009
89	12074.408	0.026	2.441	0.905	48764.054	0.027
90	12111.308	0.086	-0.367	1.682	48800.954	0.086
91	12127.296	0.223	3.143	0.637	48816.942	0.223
92	12139.580	0.004	1.071	2.871	48829.226	0.010
93	12160.967	0.028	2.247	1.373	48850.613	0.029
94	12181.902	0.009	0.219	1.059	48871.548	0.013
95	12184.640	0.011	1.306	2.791	48874.286	0.014
96	12189.657	0.026	2.058	1.506	48879.303	0.027
97	12198.506	0.017	1.937	0.921	48888.152	0.019
98	12208.353	0.005	0.252	1.172	48897.999	0.010
99	12211.286	0.018	0.286	0.571	48900.932	0.020
100	12218.598	0.002	0.328	4.614	48908.244	0.009
101	12238.526	0.051	3.252	0.747	48928.172	0.051
102	12243.147	0.002	0.410	6.379	48932.793	0.009
103	12249.927	0.022	0.006	1.843	48939.573	0.023
104	12264.966	0.078	4.868	0.861	48954.612	0.079
105	12291.108	0.003	0.288	3.682	48980.754	0.009
106	12301.253	0.038	1.963	1.237	48990.899	0.039
107	12305.908	0.028	0.389	1.373	48995.554	0.029
108	12319.015	0.030	3.125	1.329	49008.661	0.031
109	12321.585	0.001	0.347	6.074	49011.231	0.009
110	12338.404	0.033	2.897	1.158	49028.050	0.034
111	12349.877	0.021	1.932	2.395	49039.523	0.022
112	12363.787	0.022	0.616	1.242	49053.433	0.024

Table D.6. Continued

Peak #	λ_3	σ (λ_3)	FWHM (λ_3)	Avg I (nA)	E_{tot}	σ (E_{tot})
113	12367.717	0.008	1.061	3.423	49057.363	0.011
114	12392.983	0.019	0.533	0.506	49082.629	0.021
115	12399.485	0.039	0.957	0.479	49089.131	0.040
116	12411.794	0.004	0.204	0.952	49101.440	0.009
117	12415.099	0.011	0.208	0.567	49104.745	0.014
118	12432.211	0.048	2.107	0.659	49121.857	0.048
119	12438.785	0.002	0.403	2.353	49128.431	0.009
120	12455.641	0.005	0.272	1.153	49145.287	0.010
121	12467.233	0.172	-0.311	1.520	49156.879	0.173
122	12480.511	0.053	4.423	2.439	49170.157	0.054
123	12508.671	0.029	4.060	4.289	49198.317	0.030
124	12515.307	0.012	0.336	0.816	49204.953	0.015
125	12520.339	0.003	0.884	9.450	49209.985	0.009
126	12538.346	0.009	0.925	4.057	49227.992	0.012
127	12545.748	0.004	0.778	7.420	49235.394	0.009
128	12548.869	0.012	0.541	1.089	49238.515	0.015
129	12550.344	0.011	0.388	0.808	49239.990	0.014
130	12550.980	0.015	0.593	0.738	49240.626	0.017
131	12558.567	0.096	1.037	0.662	49248.213	0.097
132	12570.150	0.009	0.265	1.155	49259.796	0.012
133	12574.019	0.003	0.460	2.286	49263.665	0.009
134	12577.201	0.004	0.195	1.129	49266.847	0.010
135	12586.394	0.020	0.496	0.772	49276.040	0.022
136	12596.200	0.171	-3.571	0.414	49285.846	0.171
137	12597.778	0.049	2.280	1.486	49287.424	0.049
138	12609.028	0.016	2.971	3.308	49298.674	0.019
139	12620.913	0.014	1.295	2.637	49310.559	0.016

Table D.6. Continued

Peak #	λ_3	σ (λ_3)	FWHM (λ_3)	Avg I (nA)	E_{tot}	σ (E_{tot})
140	12640.749	0.101	1.946	1.189	49330.395	0.101
141	12643.367	0.003	0.509	6.226	49333.013	0.009
142	12646.481	0.049	1.036	1.189	49336.127	0.050
143	12650.526	0.015	1.590	2.854	49340.172	0.017
144	12661.299	0.009	1.275	6.206	49350.945	0.013
145	12666.742	0.019	1.326	2.886	49356.388	0.021
146	12674.573	0.029	2.473	0.939	49364.219	0.030
147	12686.468	0.044	1.967	0.807	49376.114	0.045
148	12692.196	0.022	0.636	0.680	49381.842	0.024
149	12694.894	0.002	0.305	2.399	49384.540	0.009
150	12706.281	0.011	0.736	1.692	49395.927	0.014
151	12734.982	0.007	0.463	2.701	49424.628	0.011
152	12736.985	0.040	0.160	0.669	49426.631	0.041
153	12740.177	0.038	1.369	1.174	49429.823	0.039
154	12744.193	0.004	0.208	2.615	49433.839	0.009
155	12751.891	0.002	0.480	10.453	49441.537	0.009
156	12755.428	0.003	0.235	5.722	49445.074	0.009
157	12756.100	0.022	0.794	0.417	49445.746	0.023
158	12758.800	0.008	0.586	1.029	49448.446	0.012
159	12764.603	0.014	0.921	3.312	49454.249	0.016
160	12776.720	0.005	0.454	6.159	49466.366	0.010
161	12791.374	0.059	-0.106	2.346	49481.020	0.060
162	12809.715	0.065	0.185	0.680	49499.361	0.066
163	12812.306	0.006	0.743	3.810	49501.952	0.010
164	12815.313	0.020	0.383	0.846	49504.959	0.022
165	12817.900	0.018	0.914	1.290	49507.546	0.020
166	12820.815	0.003	0.426	3.957	49510.461	0.009

Table D.6. Continued

Peak #	λ_3	σ (λ_3)	FWHM (λ_3)	Avg I (nA)	E_{tot}	σ (E_{tot})
167	12824.813	0.008	0.188	0.554	49514.459	0.012
168	12831.878	0.017	0.834	0.861	49521.524	0.019
169	12833.108	0.048	0.797	0.517	49522.754	0.049
170	12844.904	0.005	1.192	2.483	49534.550	0.010
171	12857.117	0.009	0.548	1.149	49546.763	0.013
172	12863.800	0.130	2.869	0.461	49553.446	0.130
173	12873.211	0.007	0.646	1.954	49562.857	0.011
174	12877.524	0.001	0.229	4.226	49567.170	0.009
175	12882.292	0.017	1.242	1.221	49571.938	0.019
176	12892.289	0.002	0.344	4.615	49581.935	0.009
177	12894.928	0.011	0.550	1.270	49584.574	0.014
178	12899.003	0.002	0.230	3.884	49588.649	0.009
179	12906.779	0.005	0.239	1.659	49596.425	0.010
180	12912.300	0.027	0.218	0.451	49601.946	0.028
181	12914.817	0.007	0.624	1.821	49604.463	0.011
182	12923.500	0.012	-0.038	0.299	49613.146	0.015
183	12929.405	0.005	0.637	1.466	49619.051	0.010
184	12934.511	0.004	0.265	1.157	49624.157	0.009
185	12938.700	0.139	1.976	0.304	49628.346	0.139
186	12945.513	0.003	0.539	2.128	49635.159	0.009
187	12952.192	0.025	0.340	0.426	49641.838	0.026
188	12956.412	0.001	0.280	4.828	49646.058	0.009
189	12961.782	0.011	0.992	0.934	49651.428	0.014
190	12972.639	0.013	2.385	1.336	49662.285	0.015
191	12989.400	0.014	1.436	1.151	49679.046	0.016
192	12994.375	0.010	1.185	1.299	49684.021	0.013
193	13006.111	0.003	0.269	1.578	49695.757	0.009

Table D.6. Continued

Peak #	λ_3	σ (λ_3)	FWHM (λ_3)	Avg I (nA)	E_{tot}	σ (E_{tot})
194	13008.578	0.020	0.309	0.562	49698.224	0.021
195	13010.821	8.543	-7.503	0.406	49700.467	8.543
196	13018.337	0.053	0.965	0.456	49707.983	0.054
197	13025.206	0.009	1.415	2.468	49714.852	0.012
198	13031.023	0.008	1.071	2.354	49720.669	0.012
199	13042.615	0.011	0.339	1.166	49732.261	0.014
200	13045.210	0.028	2.772	1.377	49734.856	0.030
201	13051.526	0.023	2.644	1.495	49741.172	0.025
202	13062.260	0.013	1.561	2.196	49751.906	0.015
203	13071.900	0.005	0.528	2.486	49761.546	0.010
204	13073.350	0.002	0.254	3.631	49762.996	0.009
205	13077.700	0.066	0.683	0.636	49767.346	0.066
206	13083.600	0.003	0.371	2.889	49773.246	0.009
207	13089.400	0.048	0.827	0.611	49779.046	0.049
208	13096.300	0.022	0.896	0.966	49785.946	0.024
209	13101.625	0.087	2.035	0.404	49791.271	0.087
210	13110.406	0.010	0.359	0.542	49800.052	0.013
211	13112.611	0.031	1.626	0.412	49802.257	0.032
212	13121.604	0.002	0.346	2.714	49811.250	0.009
213	13132.890	0.038	2.424	0.805	49822.536	0.039
214	13139.092	0.029	0.852	0.523	49828.738	0.030
215	13152.095	0.004	0.344	2.704	49841.741	0.009
216	13154.297	0.033	1.911	1.109	49843.943	0.034
217	13156.504	0.017	1.246	1.577	49846.150	0.019
218	13162.200	0.041	2.929	0.789	49851.846	0.042
219	13166.000	0.003	0.504	3.433	49855.646	0.009
220	13173.806	0.003	0.240	1.987	49863.452	0.009

Table D.6. Continued

Peak #	λ_3	σ (λ_3)	FWHM (λ_3)	Avg I (nA)	E_{tot}	σ (E_{tot})
221	13176.067	0.004	0.253	0.344	49865.713	0.010
222	13185.639	0.009	0.861	0.358	49875.285	0.012
223	13190.515	0.002	0.287	3.826	49880.161	0.009
224	13194.329	0.033	2.330	0.997	49883.975	0.034
225	13196.507	0.003	0.363	2.935	49886.153	0.009
226	13207.820	0.006	0.225	0.992	49897.466	0.011
227	13215.007	0.007	1.369	2.239	49904.653	0.011
228	13217.916	0.020	2.423	1.188	49907.562	0.022
229	13224.199	0.003	0.440	2.407	49913.845	0.009
230	13227.477	0.014	0.675	0.956	49917.123	0.016
231	13233.086	0.015	1.820	1.207	49922.732	0.017
232	13255.420	0.005	0.989	1.604	49945.066	0.010
233	13258.206	0.030	0.258	0.351	49947.852	0.032
234	13260.679	0.009	0.352	0.673	49950.325	0.013
235	13262.188	0.010	0.298	0.615	49951.834	0.013
236	13270.087	0.011	0.778	0.826	49959.733	0.014
237	13278.827	0.003	0.345	1.862	49968.473	0.009
238	13280.129	0.004	0.232	0.805	49969.775	0.010
239	13281.709	0.018	0.259	0.308	49971.355	0.020
240	13290.578	0.008	0.493	0.741	49980.224	0.012
241	13295.407	0.015	0.404	0.496	49985.053	0.017
242	13299.352	0.072	1.912	0.408	49988.998	0.073
243	13301.308	0.008	0.251	0.662	49990.954	0.012
244	13302.900	0.037	0.993	0.443	49992.546	0.038
245	13307.227	0.149	3.477	0.392	49996.873	0.149
246	13314.444	0.896	-17.439	0.463	50004.090	0.896
247	13335.745	0.005	0.967	2.643	50025.391	0.010

Table D.6. Continued

Peak #	λ_3	σ (λ_3)	FWHM (λ_3)	Avg I (nA)	E_{tot}	σ (E_{tot})
248	13342.569	0.079	3.119	0.628	50032.215	0.079
249	13350.018	0.004	0.360	1.877	50039.664	0.010

Vita

Elisa Romero Romero was born and raised in Mexico City. Before attending the University of Tennessee Knoxville, she attended the Universidad Nacional Autónoma de México where she earned a Bachelor of Arts in Physics in 2012. In the same year Elisa earned a scholarship from the Consejo Nacional de Ciencia y Tecnología and a graduate research scholarship to perform PhD studies at the University of Tennessee Knoxville and began working under the tutelage of Dr. Galindo-Uribarri in the development of ultrasensitive analytical techniques for applications in ultra-trace detection.